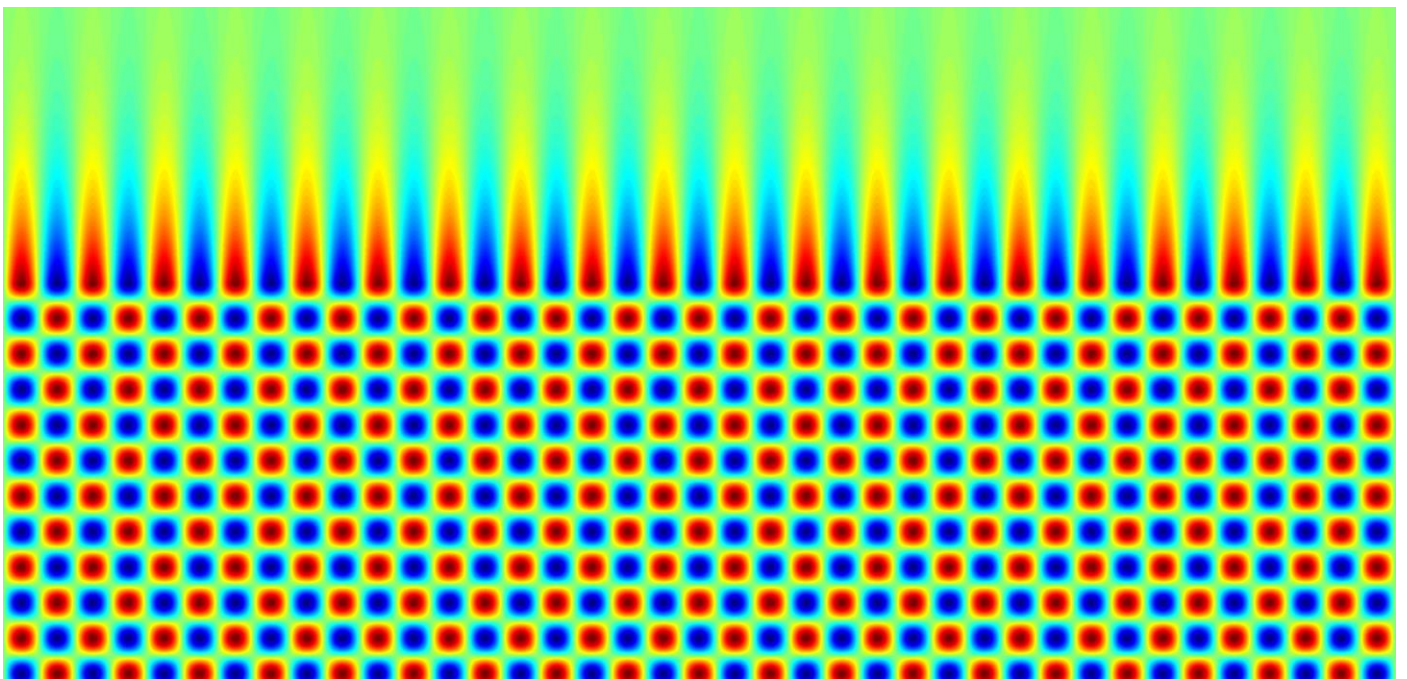


Fluorescence Detection Based Point-Of-Care Diagnostics Platforms

Bridging the gap between laboratory and market

Neeraj Adsul



∴ csem



Fluorescence Detection Based
Point-of-Care Diagnostics Platforms
Bridging the Gap between Laboratory and Market

Inauguraldissertation

zur

Erlangung der Würde eines Doktors der Philosophie
vorgelegt der
Philosophisch-Naturwissenschaftlichen Fakultät
der Universität Basel

von

Neeraj Adsul

aus Indien

Basel, 2014

Genehmigt von der Philosophisch-Naturwissenschaftlichen Fakultät
auf Antrag von

Prof. Dr. Christian Schönenberger

Dr. Alexander Stuck

Dr. Giovanni Nisato

Basel, den 10 Dez 2013

Prof. Dr. Jörg Schibler
Dekan

- To
- ▶ My Extraordinary and Loving Wife
 - ▶ My Parents
 - ▶ My Awesome Brother
 - ▶ My Grandparents

"There is Plenty of Room at the Bottom" - Richard P Feynman.

Contents

1	Introduction	1
1.1	Point of Care (PoC) Sensors	3
1.1.1	Magnetic beads assay	3
1.1.2	Supercritical Angle Fluorescence platform	4
1.1.3	TIR Guided Fluorescence Out-coupling	4
1.1.4	Fluorescence Polarization Anisotropy	5
1.1.5	Sensing with Consumer Technology	5
1.2	Commercial Point of Care platforms	5
1.2.1	TRIAGE®System	6
1.3	Motivation for Thesis Work	8
1.3.1	Opportunities and Problems Found	8
1.3.2	Proposed solutions and demonstration	8
2	BioPLC Platform	11
2.1	Introduction	11
2.2	Motivation and goal	12
2.3	Sensing Platform	12
2.4	Sensing Experiments	14
2.4.1	Fluorescent magnetic microbeads	14
2.4.2	MEH-PPV as PL layer	15
2.4.3	ADS055RE as PL layer	16
2.4.4	F8BT as PL layer with Surelight P1	17
2.5	Discussion	20
2.5.1	Comparison with theoretical model	20
2.6	Conclusions	22
3	BioCOP	23
3.1	Introduction	23
3.2	Overview of Idea	24
3.3	Chip Design	25
3.3.1	Substrate Material	25
3.3.2	Fluorescence immunoassay	26
3.3.3	Two sided embossing	27
3.3.4	Total internal reflection (TIR) angle	27
3.3.5	Evanescent Field	28
3.3.6	Placement of gratings and fluidics	30
3.3.7	Excitation beam width	31

3.3.8	Mask Design	33
3.4	Electrical Design	35
3.5	Grating Design	37
3.5.1	Grating Performance Parameters	37
3.5.2	Zinc Sulphide (ZnS) High Index Coating	39
3.5.3	Grating Simulations	40
3.5.4	Simulation results	40
3.5.5	Grating filter	43
3.6	Fabrication of Chip	44
3.7	Characterization	47
3.7.1	Selection of filters	49
3.8	Biosensing Experiments	51
3.8.1	Experiment-01 Dose-response	51
3.8.2	Experiment-02 Fluorescence Microscopy	52
3.8.3	Experiment-03 Dose Response	53
3.8.4	Experiment-04 Dose-response	54
3.9	Final Updated Design	55
3.10	Conclusions	56
4	Photo-FET	59
4.1	Introduction	60
4.2	Device physics	61
4.2.1	LE-FET	61
4.2.2	LS-FET	62
4.3	Design	63
4.3.1	Mask Layouts	63
4.4	Problem of contacting ITO Pads	64
4.5	Spectral characteristics of integrated system	67
4.6	Testing FET devices	67
4.6.1	LE-FET - LS-FET face-to-face	67
4.6.2	LE-FET - Fluidic Chip - LS-FET	69
4.6.3	Fluorescence measurements	69
4.7	Blue OLED and OPD	69
4.8	Photo-FET Reader	71
4.8.1	Mechanical Design	71
4.8.2	Electrical design	74
4.9	Benchmarking of Photo-FET Reader	76
4.9.1	OLED - Si Photodiode Test	78
4.10	Conclusions	78
5	Conclusions and Outlook	81
	Bibliography	83
A	Appendix	87

1

Introduction

We can agree that *Prevention is better than cure*, whether it is matter of health, security or any other aspect of life. As an example, at an accident spot; before administrating any emergency medication it might be suitable to quickly check for victims allergic response to it. Airport security often needs to test for explosives or narcotics. People with diabetes regularly monitor blood glucose as control measure in order not to escalate the disorder.

In recent decades humanity has achieved great success over communicable diseases which were historically massive epidemics. Few of such diseases under fair control are polio, tuberculosis, HIV/AIDS etc. However our lifestyle has given us chronic illnesses or also known as non-communicable diseases (NCD). These disorders include cancer, diabetes, heart disease and mental illnesses. Although such disorders used to occur at old age, now-a-days onset age these have drastically come down. This makes society unhealthy, less productive and unhappy. Such a population adds huge overhead or economic burden on the economy of the country. Therefore strategic actions to emphasize preventive medicine and early disease diagnostics must be deployed.

Point-of-Care(PoC) sensors are compact, low-cost and provide rapid analysis (typically within 30 minutes). The term PoC sensors really means that the sensor could be used wherever required, not limited to dedicated analysis laboratories. Such sensors could be of tremendous help for the preventive strategy.

A critical review published by Chin et al. [1] gives an excellent list of companies working towards developing PoC devices, out of which many are based on fluorescence detection. In the table1.1 some of the examples of fluorescence based sensors are summarized.

(Some of the acronyms from table- f-TIR: frustrated total internal reflection; SAF: supercritical angle fluorescence, TIR: total internal reflection, LOD: limit of detection)

Immunoassay technique is extremely sensitive and highly specific. Sensitive means that it can detect extremely low concentrations of the analyte. Specific means that the assays themselves are less susceptible to non-specific bindings. Though environmental changes such as temperature or the medium in which assay is carried out may affect the specificity. Immunoassay technique combined with fluorescent labeling is very flexible mainly due to availability of wide range of fluorescent labels to choose from. It also benefits from progress in image sensors and photo detector technology.

Despite these inherent advantages, it is only in the last decade commercial PoC devices are being developed based on fluorescence detection. Many sensor platforms

Table 1.1: Examples of fluorescence based PoC Sensors

Detection method	Analyte/Assay	Novelty	Performance
Fluorescence microscope [2]	c-reactive protein	capillary driven fluidic chip	1ng/mL, 5 minutes, 5 μ L of serum
CCD imaging device measuring change in f-TIR [3]	Troponin-I, morphine	magnetic nanobeads assay, no fluidics is required	3pM for cTnI, 30ng/ml for morphine
Microfluorimeter with photodiode and LED [4]	Gliadin protein for celiac disease	reflector or metalized surfaces inside the fluidic chip	4.1 ng/mL
In-situ fluorimetry photodiode and LED [5]	phytoplankton fluorescence	Application and ultra low cost	4% error compared to commercial, good enough
CCD based detection of evanescently excited fluorescence [6]	general purpose, high throughput	single mode waveguide, gratings to in-couple laser in	1 pg/mL
Spectrofluorometer [7]	pH sensitive dye inside solgel-based matrix to measure dissolved CO ₂	ratiometric measurement using dual LED excitation	35 ppb LOD
SAF detection using photomultiplier [8]	Streptavidin - IL2	Paraboloid element for focus SAF only	subpicomolar
Lateral flow assay [9]	Mycotoxin - fumonisin	Assay itself	<5ug/L
Fiber collection into spectrometer [10]	antibody antigen (CRP)	TIR guided fluorescence out-coupling by cutting chip at 60°	0.1mg/L
Fluorimeter [11]	nanoparticle antibodies for cardiac cTnT and cTnI	Fluorescence polarization anisotropy measurement	cTnT, cTnI 15 pM for both

are demonstrated in the academic and patent literature. Only few of these have been actually been successfully transferred from lab to at least a start-up and very few make it to commercial markets.

Instead of fixating on summarizing only the performance parameters such as sensitivity, detection limit and estimated cost, I have followed a different approach. Six relevant published examples (5 academic + 1 commercial) are concisely explained and illustrated. This provides an insight into what kind of innovation or "thinking different" is necessary.

1.1 Point of Care (PoC) Sensors

1.1.1 Magnetic beads assay

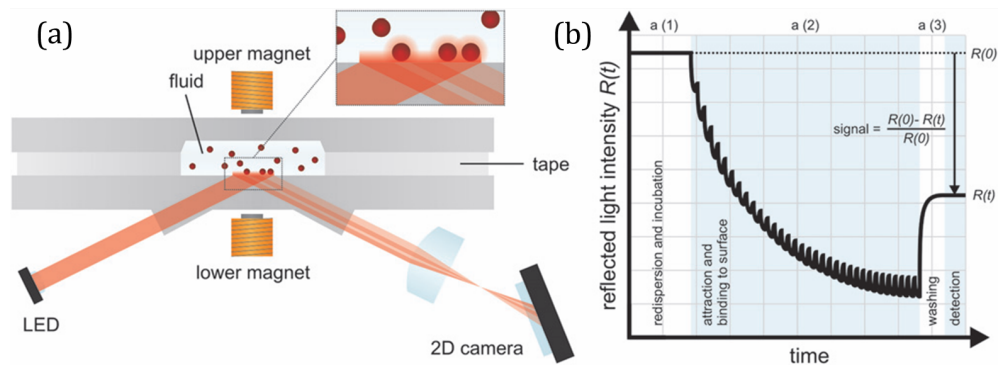


Figure 1.1: Schematic and single measurement adopted from [3] - (b)Magnetic beads assay controlled by two electromagnets (e) Signal drops as more and more beads are collected at the interface

Working principle: When light incident upon a substrate is reflected back in air such that it undergoes total internal reflection (TIR) inside the substrate, result is called frustrated-TIR or f-TIR. The arrangement of the sensor is shown in figure 1.1(a). Magnetic nanoparticles gets attached on the surface from where the beam is reflected. This causes drop in beam intensity as a function of concentration of particles then monitored by a camera. Examples of such intensity changes monitored by camera are shown in figure 1.1(b).

Morphine Assay: Anti-morphine antibodies are attached to magnetic nanoparticles. Surface is provided with morphine conjugated to BSA. Sample containing morphine is mixed with nanoparticles. As a first step electromagnets bring all nanoparticles close to bottom surface. Particles bound to morphine do not bind to surface while others free of morphine do. Then electromagnets move away the particles which are unbound and weakly bound. At this point signal increases to maximum.

Paper also demonstrates other assays including Cardiac Troponin-I and substance of drug abuse.

Claimed advantages are: Microfluidics is not required since there is no need to flow solutions, low cost cartridge, multiplexed assays possible.

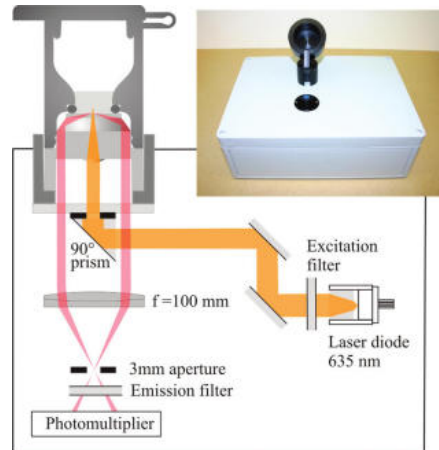


Figure 1.2: Schematic and photograph of SAF platform adopted from [8] - Shows arrangement with disposable cartridge and optical paths of excitation and emission

1.1.2 Supercritical Angle Fluorescence platform

It consists of a tube with specially designed paraboloid optical lens at the bottom. Top surface of this lens forms the sensing area. Fluorescent analyte is excited using laser, dichroic mirror and a 90° prism as shown in 1.2. Due to paraboloid lens only supercritical angle fluorescence is focused back into a photomultiplier tube.

Their work demonstrated an assay based upon functionalized Zeonex plastic using silanes + Dextran hydro-gel. Dose-response was measured using Streptavidin and biotinylated IL-2 capture antibodies. The platform detects only evanescently out-coupled fluorescence, specifically coupled into forbidden zone. A small disposable cartridge has also been developed. Novelty lies in design of paraboloid element.

1.1.3 TIR Guided Fluorescence Out-coupling

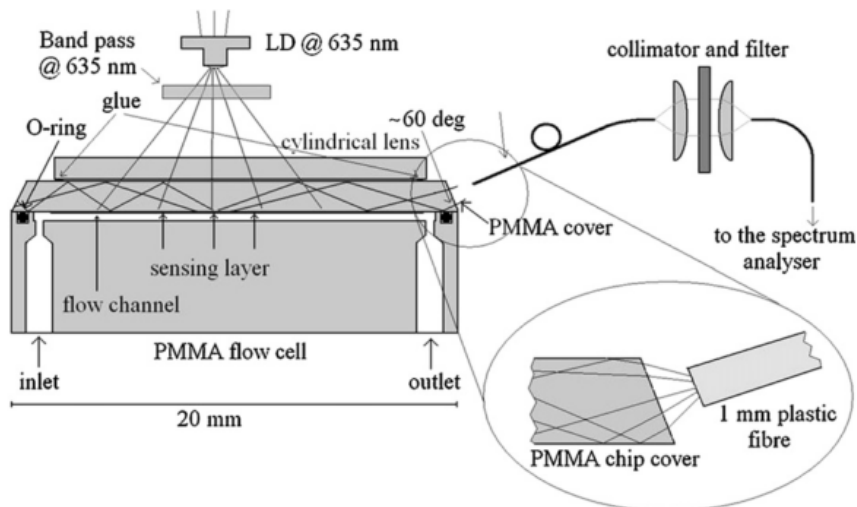


Figure 1.3: Schematic adopted from [10] - Show the fluid flow and optical paths of excitation, out-coupling and detection

Fluorescence emitted close to a thick PMMA substrate is guided by total internal reflection (TIR). Out-coupling is achieved by precisely cutting the edge at 60° , shown in 1.3. Assay involves PMMA coated with EUDRAGIT L100 anionic copolymers then activated and attached with C5 capture antibodies (A or B or C types), Sandwich assay contains C5 antibodies CRP antigen target antibody C7 clone with DY-647 fluorophores. Fluorescence emitted is Laser Induced Fluorescence (LIF). Proposed solution reduces background signal by detecting only the evanescently coupled fluorescence.

1.1.4 Fluorescence Polarization Anisotropy

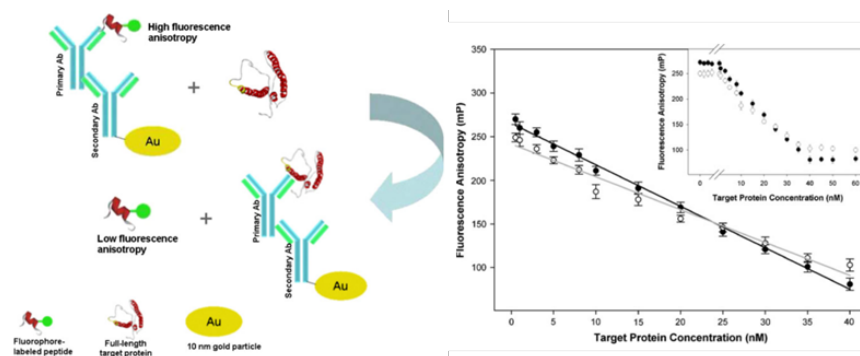


Figure 1.4: Assay and Dose Response adopted from [11] - (left) Au NPs are attached to Secondary Ab and Primary Ab are labeled with fluorophores. (right) Shows dose response obtained from fluorescence polarization anisotropy assay

Detection of : Fluorescence polarization anisotropy using equation

$$r = \frac{I_{\parallel} - I_{\perp}}{I_{\parallel} + 2I_{\perp}}$$

Fluorescence intensities of vertically (I_{\parallel}) and horizontally polarized emission (I_{\perp}) are measured by alternatively orienting the polarizer parallel and perpendicular.

Antibodies are attached with metallic nanoparticles. After binding, fluorescence emission is influenced by close proximity of nanoparticles resulting in polarization anisotropy.

1.1.5 Sensing with Consumer Technology

Smartphones have become ubiquitous in our lives. Their performances, varieties of embedded sensors, quality front/back camera, computing power and sophisticated programming options are breaking new grounds every year. It is totally possible to take advantage of their hardware capability combined with intelligent algorithms to make sensor platforms. Especially their imaging capabilities are demonstrated in articles summarized in table 1.2

1.2 Commercial Point of Care platforms

Commercial interest for developing PoC devices is well justified. Figure 1.5 shows global market overview. IVD market in 2012 was 72 billion USD of which PoC part was 21.5 billion USD (30%)[20].

Table 1.2: Colorimetric or fluorescence detection based on Smartphones or Mobile Phones

Reference	Principle, Comments
Tseng2010[12]	Incoherent in-line holography. Image and hologram reconstruction as output, data processing on computer
Mudanyali2012[13]	Image capture and processing. Automated reader for lateral flow immunoassay strip
Shen2012[14]	Image capture and processing. Automatic reading of colorimetric urine strips
Navruz2013[15]	Fiber optic tapering imager to focus image, capture and processing. Image quality captured on phone comparable to microscope
Wei2013[16]	Fluorescent imaging of single nanoparticle and viruses. Compact but high performance optical system as attachment to phone
Zhu2013[17]	Image capture and processing. Simple optical attachment, whole blood cell counter on phone. Results comparable to automated cell counters.
Coskun2013[18], Coskun2013a[19]	Laser or LED excited fluorescence in cuvettes, emission captured and processed by camera. Urine Albumin measurement, Peanuts detection for peanut allergy. Design of a simple attachment to phone containing optics and holders

Next section describes commercially successful PoC platform TRIAGE® for detection of cardiac markers. The system is widely used at hospitals in USA. It was developed by company BIOSITE Inc., recently acquired by Alere group of companies.

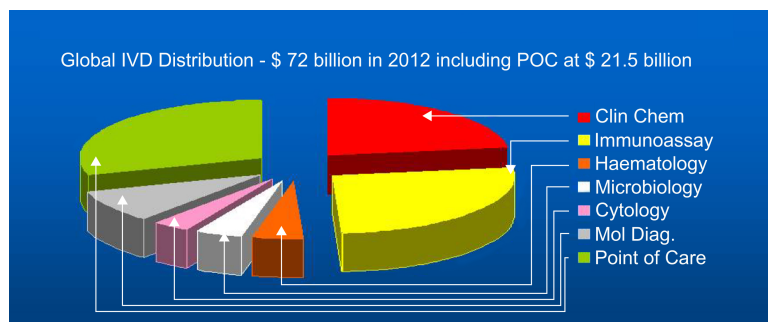


Figure 1.5: Global IVD Market Distribution in 2012 - Point-of-Care IVD comprises of more than 72 billion USD, PoC Share 30%.

1.2.1 TRIAGE® System

Sample: Whole blood or plasma in anti-coagulating tube

Assay Principle: A fluorescence resonance energy transfer (FRET) dye is excited at $\lambda = 670nm$ by a laser diode which fluoresces at $\lambda = 760nm$. The dye is incorporated into latex particles to make fluoresce based on principle of fluorescence energy transfer latex (FETL). Emission is detected by array of silicon photodiodes.

Assay device: Contains a base, a blood filter, a lid and a label as shown in Figure 1.6.

Assay process: Blood sample added in the sample zone enters the filter where RBCs

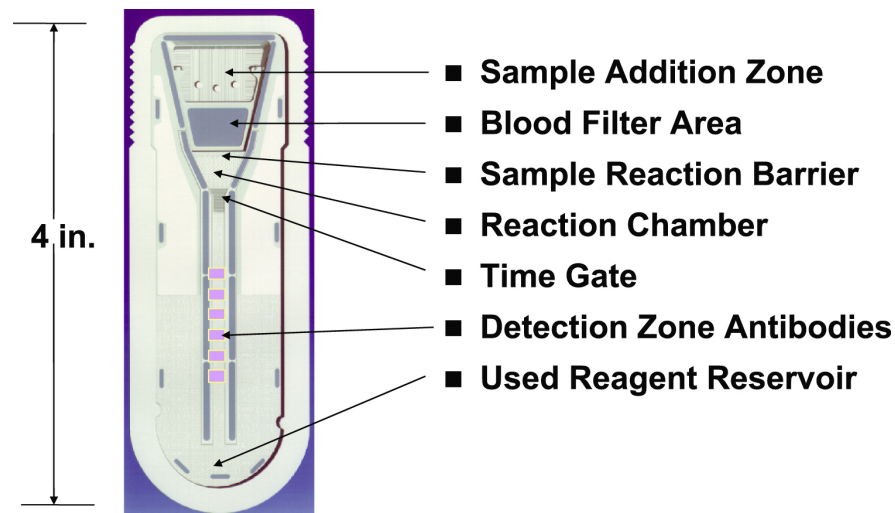


Figure 1.6: TRIAGE®meter disposable cartridge - Shows components on the chip.

are separated from plasma due to lateral flow. Plasma enters high capillarity zone called Sample Reaction Barrier (SRB). Fluid goes from SRB to low capillarity zone Reaction Chamber (RC) and delayed at the time gate (TG). This gives time for analyte to conjugate with fluorescent antibodies in RC. TG is hydrophobic which becomes hydrophilic because proteins from sample bind to TG surface. This process provides the incubation time for assay which is typically 2 minutes. The detection zone is hydrophilic channel which allows smooth flow to the end reservoir. The detection zone has high and low positive controls, a negative control, and antibodies for the analyte to be measured. The excess plasma washes the channel removing unbound analyte.



Figure 1.7: TRIAGE®reader - Form factor is desktop reader and designed for laboratory use with little training.

Analytes Measured: This system measures many of the cardiac markers CK-MB, Troponin-I, Myoglobin, B-type Natriuretic Peptide (BNP), NT-proBNP using different cartridges. A single cartridge can perform maximum of 3 tests simultaneously.

1.3 Motivation for Thesis Work

1.3.1 Opportunities and Problems Found

From all the platforms reviewed in previous sections, I see following opportunities to improve upon:

1. Microfluidics substrate, mechanical support structures are separately fabricated and then assembled with rest of the device. Assembling many things together in a disposable cartridge increases cost of the consumable. Complete integration would further reduce the cost of the cartridge.
2. Many devices use direct face-to-face excitation or fluorescence microscope like excitation. Therefore exciter-detector optical path requires precisely aligned cross polarizers and stack of filters in the reader. To reduce background signal in such a configuration, optical elements needs to high performance and their cost goes up. If we use off-normal illumination or use evanescent field excitation the background will be minimal.
3. Many demonstrated platforms use photo multipliers or ultra low noise cooled CCD or CMOS sensors. They are not portable at all. Use of off the shelf silicon photodiodes or even better Organic Photodiodes (OPDs) will further reduce the cost of reader as well.

1.3.2 Proposed solutions and demonstration

To improve upon all above points has motivated me to design, fabricate and evaluate multiple biosensor platforms. Each one applies different approaches to solve these problems. This has allowed me to clearly identify the challenges of total integration without loss of performance. I have demonstrated solutions to number of these challenges in following three sensor platforms which together form my thesis work.

1. **BioPLC**

BioPLC stands for **Bio** Photoluminescent **Coupling**) This platform is based upon evanescent field excitation of the analyte attached with fluorescence labeled antibodies captured near a waveguide surface on a glass chip. This platform *demonstrates how to in-couple the excitation light from a photoluminescent polymer into a low mode waveguide without use of exotic coupling techniques* such as gratings, prism, end face or butt coupling. It uses off the shelf low cost LEDs, silicon photodiodes and longpass filters for detecting fluorescence from analyte.

2. **BioCOP** This platform demonstrates *integration of mechanical support, microfluidics and optical in-coupling structures into a single plastic substrate*. Gratings are designed and optimized for in-coupling of excitation light into substrate. They can be photo-excited with two possible approaches. For surface sensitive detection and live measurements evanescent field excitation can be used. If measurement during the assay is not required then after final washing step through excitation with off-normal illumination can be chosen. A laser diode, silicon photodiode and a very low-cost longpass foil filter are the optical elements used as reader.

3. **PHOTO-FET** This was an EU funded project PHOTO-FET(FP7-ICT-248052). We developed fully disposable platform for simultaneous detection of three cardiac markers - CK-MB, Troponin-I and Myoglobin. *Microfluidics and all optical components such as polarizers, filters etc. are integrated on the disposable chip by lamination.* Trans-illumination excitation is used and light sources are low cost inorganic green LEDs or organic light emitters such as OLEDs or Organic Light Emitting-FETs(LE-FET). Detectors used are silicon photodiodes or organic light sensitive devices such as OPDs or Organic Light Sensing FETs (LS-FET). This is a commercially developed system for company Molecular Vision Ltd.

2

BioPLC Platform

2.1 Introduction

Optical waveguides for fluorescence excitation and collection for in-field sensors began with the use of optical fiber[21]. Optical fiber has distinct advantage of carrying the signals to very long distances without much losses. But their properties can not be changed with ease and their systems are cumbersome to handle. In contrast, planar optical waveguides are easy to design and fabricate for given requirements, also very efficient in exciting and collecting fluorescence. Zeptosense AG's(acquired by Bayer) bio-sensing platform has demonstrated and commercially deployed an optical waveguide based fluorescence detection[6]. Planar waveguides have also been utilized for improving the contrast in fluorescence microscopy [22].

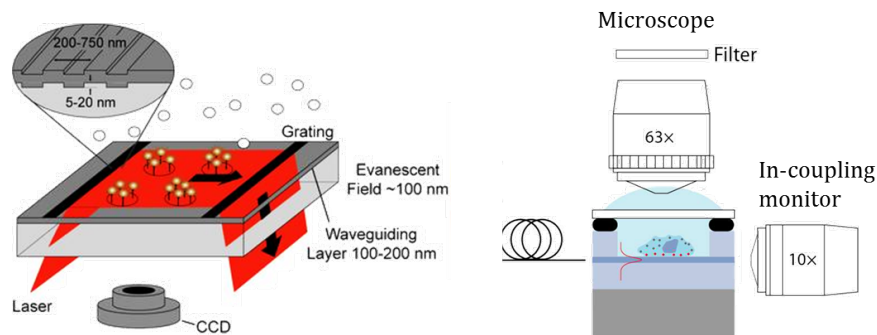


Figure 2.1: Schematics of Single Mode Optical Waveguide platforms - Light is coupled into a single mode waveguide by using gratings [6](left) and end face coupling [22](right). Fluorescence is excited by evanescent field of the guided light.

Figure 2.1 shows schematics of both the mentioned examples. Zeptosense platform consists of two parallel pads of gratings fabricated into glass close to longer sides of the chip. A single mode tantalum pentoxide (Ta_2O_5) waveguide is deposited on the glass substrate also coating the gratings. Fluorescent analyte is immobilized in the region between two grating pads. A laser coupled into the waveguide excites fluorescence by its evanescent field. The emission from analyte can be detected by a CCD imager underneath. The second grating can out-couple the laser and used for referencing. The gratings are fabricated into glass. The detection limits obtained are in range 1-15 pg/mL . Since very high precision of fabrication of grating is a necessity, the cost of such a chip is close to 100 EUR.

The microscopy platform consists of a polymer (PMMA $n \approx 1.49$) based low mode waveguide fabricated on a glass substrate using a low index polymer layer (Cytop polymer $n \approx 1.34$) acting as cladding. The thickness of PMMA layer is designed to support only single mode. Cells labeled with fluorescent dye are fixed on the waveguide. Light coupled into waveguide with edge coupling interacts with cell via evanescent field only creating a better contrast image as compared by the paper. In such type of sensors, coupling of light into a single mode waveguide with high efficiency still remains a challenge.

Previous work at CSEM SA by Ramuz et. al [23, 24] demonstrated coupling of Organic LED emission into a Ta_2O_5 based single mode waveguide. It has been used with an Organic Photodiode (OPD) based spectrometer under EU project SEMOFOS (Project Nr. IST-FP6-016768). Later on, efficient coupling of light from a photoluminescent polymer layer (PL layer), deposited on the similar waveguide was also shown [25]. This work measured changes in spectrum of guided light corresponding to analyte concentration. Complete dose-response test was not performed.

2.2 Motivation and goal

As already mentioned, cost of Ta_2O_5 single mode waveguide fabricated with in-coupling and out-coupling gratings is very high. Interestingly more than 95% of the cost is for making the gratings on a glass substrate. Similar coupling efficiency can be obtained without use of grating and therefore it was intriguing to benchmark the performance of a platform consisting of:

- ▶ PL layer based coupling of light into a single mode, Ta_2O_5 waveguide
- ▶ Evanescent excitation of analyte captured on the waveguide surface by guided light
- ▶ Off the shelf silicon photodiodes to measure intensity of emitted fluorescence.

In this chapter we benchmark such system. Development of one-step surface chemistry for such optical waveguides with better coverage and fluorescence intensity was also performed. This was done in collaboration with Landquart center of CSEM SA.

2.3 Sensing Platform

The schematic of the complete sensing platform is shown in the Figure 2.2. It consists of a glass substrate (0.7mm thick) deposited with 150 nm Ta_2O_5 . In the center of the waveguide, a photoluminescent polymer (PL layer) (ADS055RE or F8BT or MEH-PPV) of thickness $\approx 100 - 200nm$ is deposited in an inert atmosphere of a glove-box. It was annealed to remove any excess solvent. Finally encapsulated with $\approx 300 - 500\mu m$ thick UV epoxy and 0.3mm square glass piece to protect from degradation [26]. Two custom designed and micro-machined microfluidics pieces were placed symmetrically on two sides of PL layer spot. One of the advantages of the proposed configuration was that due to symmetry considerations equal amount of PL light propagates in each direction and thus allows for a stable reference. A chip prepared with above process is shown in figure 2.2, bottom. The chip is placed in a specially designed and micro-machined holder made in black ABS plastic. A blue LED is fixed just under PL layer which has emission angle of 15° so as to illuminate only PL spot. Two Si photodiodes (Hamamatsu S2387, $5.6 \times 5.6mm^2$) were placed exactly under the fluidic areas. Two

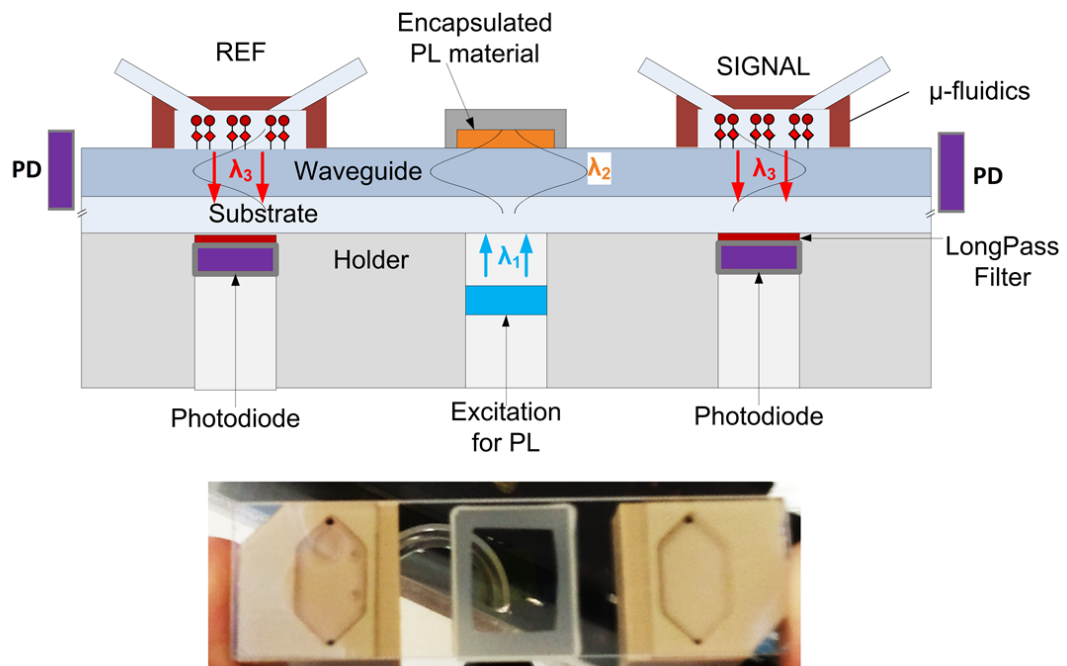


Figure 2.2: Schematic of BioPLC principle - The device consists of a central excitation channel and two detection channels for signal and reference, respectively.

optional photodiodes can also be used at the edge of the chip to monitor in-coupled light or fluorescence emission from analyte.

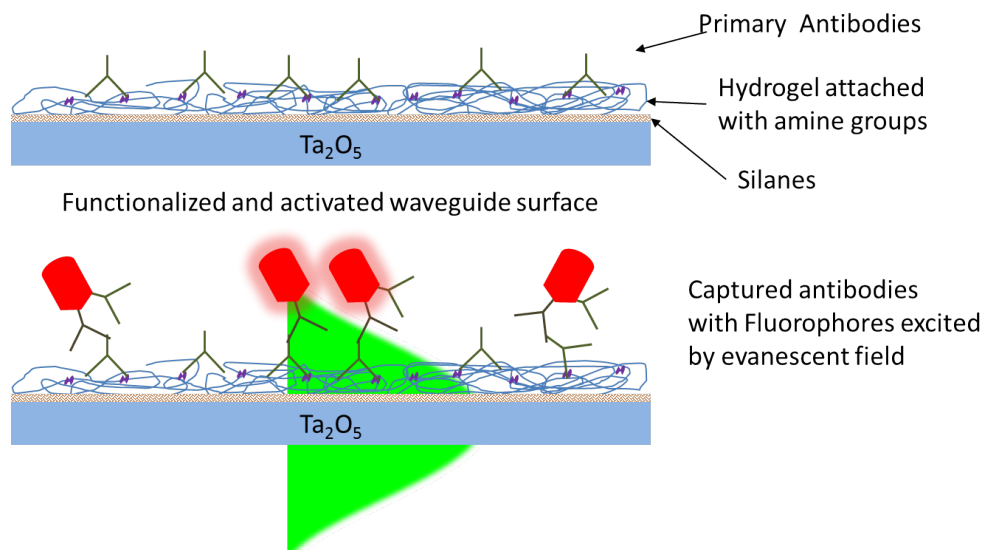


Figure 2.3: Immunoassay reaction schematic - Waveguide surface functionalized with hydrogel which is attached with primary antibodies. Labeled secondary antibodies are flown through the channel which are captured on surface by primary antibodies. Evanescent field of guided light excites the fluorophores.

The platform was tested with a fluorescence immunoassay based on IgG. The principle of immunoassay is shown in Figure 2.3 After cleaning, chip surface was functionalized with silanes + dextran based hydrogel using in-house developed process (CSEM at Landquart). Just before the experiment hydrogel was activated by first

washing with sodium maleate buffer, then using N-hydroxysuccinimide(NHS) + N-(3-dimethylaminopropyl)-N'-ethylcarbo-di-imide hydrochloride(EDC) in 2-(N-morpholino) ethanesulfonic (MES) buffer to attach amine groups to the hydrogel. Finally primary antibodies (Rabbit IgG in PBS) were attached to the surface to act as capture element for labeled secondary antibodies.

2.4 Sensing Experiments

2.4.1 Fluorescent magnetic microbeads

While the surface chemistry for functionalization was being developed, we tested the platform with polymer magnetic fluorescent microparticles(from Microparticles GmbH www.microparticles.de). These particles have peak absorption/emission at 633/672nm, are opaque and have nominal diameter of $\approx 10\mu m$. Due to opaque nature fluorescence emission is detectable only in the direction same as excitation. In our platform the photodiode is on the same side as excitation. A long pass color filter was used to filter out the any scattered background excitation. Photodiode currents were amplified by an transimpedance amplifier with gain 10^6 . The original stock solution of microparticles

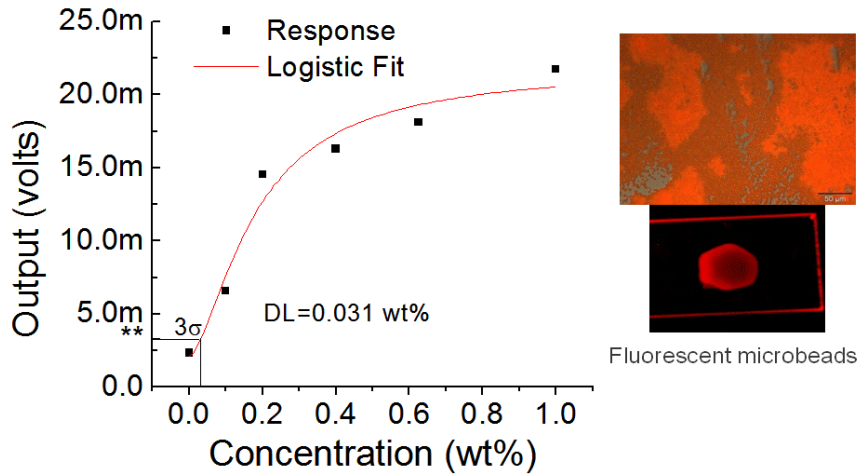


Figure 2.4: Dose-response with fluorescent microparticles. - Concentrations of 0.1, 0.2, 0.4 and 0.625 and 1 wt%. Photos on right shows microscope image of one such layer (top) and on chip excited by evanescent field (bottom)

was 1wt% (10mg/ml). It was diluted in series 0.1, 0.2, 0.4 and 0.625 wt%. Before making each dilution, stock solution was lightly ultra-sonicated to separate the microparticles. For each measurement $2\mu L$ solution was drop casted in the sensing region and was allowed to dry. The measurement was carried out by turning on the blue LED to excite PL layer. The emission from PL layer was guided into the waveguide and the dried fluorescent particles layer was illuminated. Before applying next dose microparticles were wiped off with first with DI H_2O and then with ethanol using a clean-room grade low particle tissue. Complete dose response curve and illuminated microbeads for highest concentration layer is shown in figure 2.4. Bright red light on the edges of the chip is guided light scattered by microbead layer. Dark spot in the center of particle layer is due to one sided emission from microparticles.

The detection limit (LOD or DL) calculated from 3σ ($3 \times$ standard deviation) and is estimated to be 0.031 wt% (0.31 mg/ml). This test validated the basic functioning of

the setup. Actual bio-tests were carried out with different combinations of fluorophores and PL layer materials which are explained in following sections.

2.4.2 MEH-PPV as PL layer

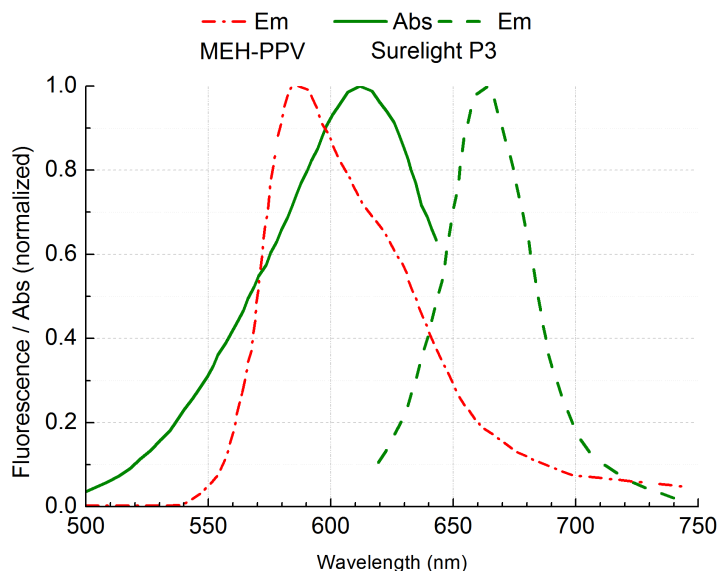


Figure 2.5: Absorption/emission spectra of used materials. - (continuous/dashes) absorption/emission of Surelight P3 (dash-dot) MEH-PPV emission

MEH-PPV (Poly[2-methoxy-5-(2-ethylhexyloxy)-1,4-phenylenevinylene]) is high brightness photoluminescent polymer ($M_W > 100k$) which is used in Organic LEDs as electroluminescent material. It is regularly used in our lab and was readily available. MEH-PPV has absorption/emission maxima at 550/587nm. Figure 2.5 shows related spectra including compatible fluorophore Surelight P3.

Chip is functionalized as explained in Section 2.3.

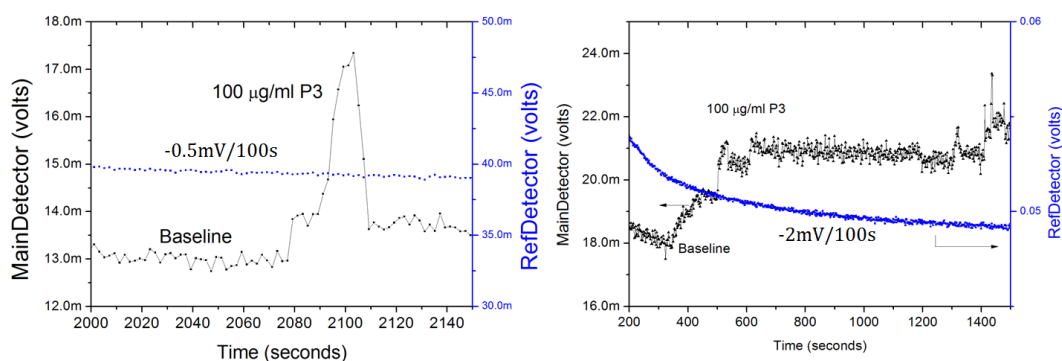


Figure 2.6: Single dose experiment, - MEH-PPV as PL layer and secondary antibodies + Surelight P3 as analyte.(left) Response on used chip rise and fall due to inefficient binding(right) Response on fresh chip rises by 3mV(without correcting for decay) and stays.

As a starting point, an old chip (used 5 weeks before for testing and stored inside the glove-box after use) was dosed with 400 μ L of 100 μ g/ml analyte. The response recorded

is shown in 2.6 (left). Reference detector (blue dotted curve) monitors intensity of in-coupled light on the edge of the chip. Since encapsulated PL layer was already burned-in, intensity remained fairly stable (decay rate $-0.5\text{mV}/100\text{s}$). PL layer decays faster at first until all air inside the encapsulation is used up during photo-oxidation, which is called burned-in effect[27]. Main detector showed 5mV increase at first but then dropped to 1mV above the baseline during washing step. This was due to degraded or already used-up functionalization on the chip.

Then same test was repeated on freshly prepared chip. As expected PL intensity decayed faster (decay rate $-2\text{mV}/100\text{s}$) By injection of $100\mu\text{g}/\text{ml}$, the signal increased by about 6mV (after correcting for decay). It stayed at the same level even while washing with PBS as shown in figure 2.6 (right).

From these experiments we concluded that the signal gain was not adequate (only $6\text{mV}/$ per $100\mu\text{g}/\text{ml}$). It can be explained from spectral matching in figure 2.5. The overlapping of MEH-PPV and Surelight P3 emission spectra is very large. Due to extended overlap guided light which is scattered by the fluidics and sensing area contributes much of the baseline signal and makes spatial filtering ineffective. Hence we replaced MEH-PPV by a narrow emission spectrum dye ADS055RE (American Dye Source). Its emission matches with the fluorophore absorption as seen in figure 2.7.

2.4.3 ADS055RE as PL layer

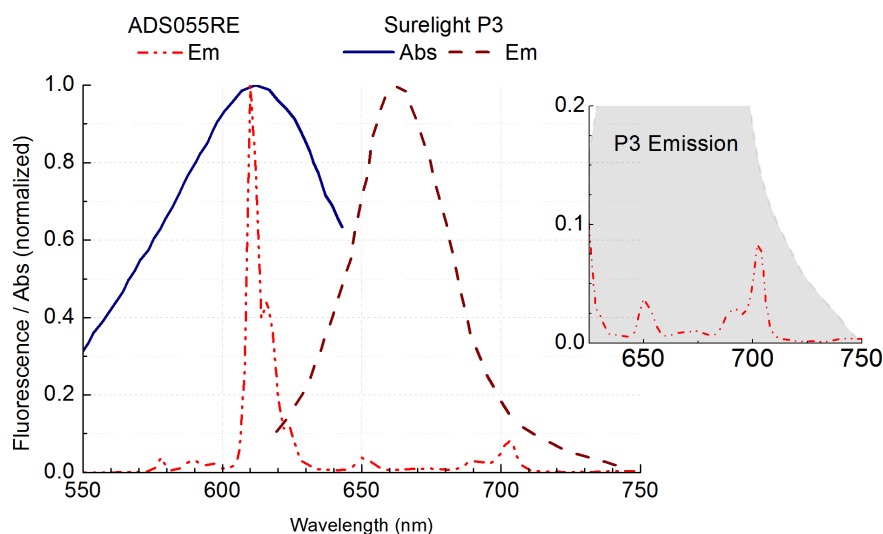


Figure 2.7: Spectra of ADS055RE and Surelight P3. - ADS055RE emission perfectly matches with the absorption of Surelight P3. (b) highlights additional peaks at 650 and 702 nm inside emission tail of PL

ADS055RE is phosphorescent metal complex used for making organic light emitting devices (source American Dye Source www.adsdyes.com). It's a small molecule ($M_w = 1458.51$ g/mol) with absorption/emission maxima at $371/613\text{nm}$. For testing this combination of PL layer + fluorophore, we started with dose of $10\mu\text{g}/\text{mL}$. The recorded signal is shown in figure 2.8(left). The response was 0.4mV increase over the baseline. Fluctuations at the beginning are due to air-bubbles. Response to $100\mu\text{g}/\text{mL}$ is shown in 2.8(right). It was 4.5mV above the base line. When flow-rate was doubled to $40\mu\text{L}/\text{min}$ for second dose of $100\mu\text{g}/\text{mL}$. As it's clearly seen that the signal rose faster

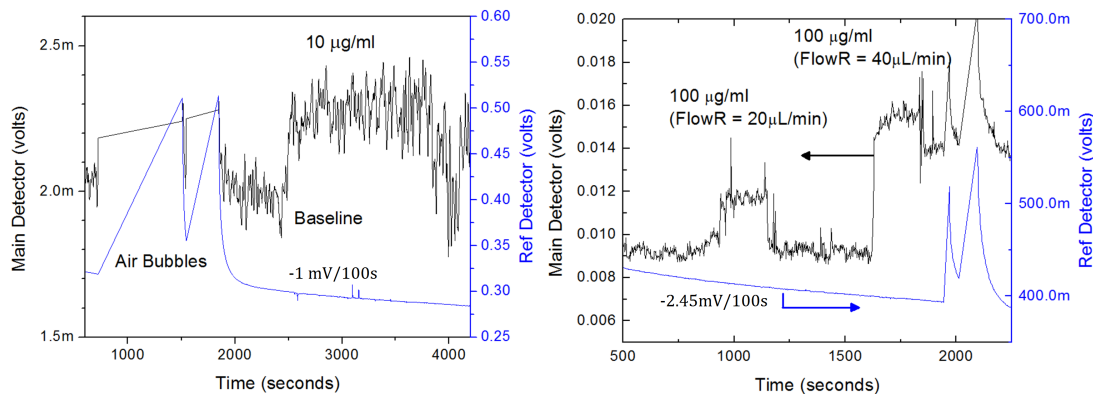


Figure 2.8: Single Dose Experiment - ADS055RE as PL layer + secondary antibodies + P3 as analyte. (left) $10\mu\text{g/mL}$ dose (right) $100\mu\text{g/ml}$ First peak flow-rate of $20\mu\text{L/min}$ and second time with $40\mu\text{L/min}$ was used.

than before along with higher fluorescence signal. This is due to increased concentration of secondary antibodies on surface. Additionally as seen from graphs, binding is not permanent. This chip could have problem with the surface quality as we had seen white clouds formations after deposition of PL layer.

Lowest concentration detected ($10\mu\text{g/mL}$) with ADS055RE-P3 combination is ten times better than MEH-PPV ($100\mu\text{g/ml}$). We discovered problem with decay of encapsulated ADS055RE (decay rate $-2.45\text{mV}/100\text{s}$). Also at first use it decayed $-1\text{mV}/100\text{s}$ but as exposure continued it was faster. ADS055RE was excited by 365nm UV LED since it absorbs only in UV. Organic materials degrade under UV exposure and this forced us to search for alternative.

To overcome the limitation, F8BT (Poly[(9,9-di-n-octylfluorenyl-2,7-diyl)-alt-(benzo[2,1,3]thiadiazol-4,8-diyl)]) was tried as PL layer. Experiments with F8BT are discussed in the next section.

2.4.4 F8BT as PL layer with Surelight P1

F8BT is a polymer ($M_W > 100\text{k}$) used as organic semiconductor in organic transistors (OFET)[28], light emitting transistors (LE-OFET)[29], as well as solid state DFB laser[30]. It has absorption/emission maxima at $430/540\text{nm}$. A compatible fluorophore surelight P1 was chosen which absorbs/emits at $540/666\text{nm}$. All related spectra are shown in figure 2.9.

For the tests, first the hydrogel was activated and primary capture antibodies were immobilized on the waveguide surface, as already explained in 2.3. Dose-response test was performed with $400\mu\text{L}$ of concentrations $5, 10, 50, 250\mu\text{g/ml}$, with flow rate of $20\mu\text{L/min}$. The response recorded is shown in figure 2.10. Left axis (brown) is for main detector and right (blue) is for reference detector. Between each dose, channel was washed with PBS buffer at higher flow-rate of $80\text{-}100\mu\text{L/min}$. Higher flow-rate wash step is seen as small symmetric bumps in the graph. Unfortunately after first dose of 5 , an air-bubble entered into main channel. We reversed the flow and then used maximum flow-rate(1 ml/min) to remove it (tiny sharp downward spike at about 50min). The signal for lowest concentration of $5\mu\text{g/ml}$ was lost. At the end of highest concentration ($250\mu\text{g/ml}$) lower doses were re-tested. Chip was regenerated removing bound secondary antibodies by flowing glycine/HCl $\text{pH}=2.4$ through the channel. This

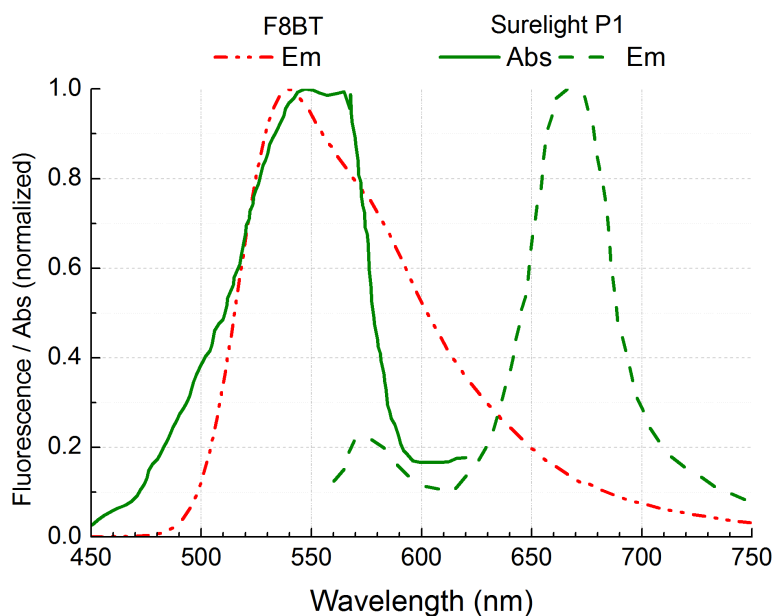


Figure 2.9: Spectra of Surelight P1 fluorophore, F8BT as PL layer - inset shows optically pumped organic laser made with F8BT from [30].

resulted in sharp dips seen in the graph marked as regeneration. A $50\mu\text{g/ml}$ dose applied after regeneration produced higher signal than before, for the same dose. We attribute this to greater availability of free capture antibodies on the surface. Chip was regenerated once more and dosed with even lower concentration ($25\mu\text{g/ml}$). A sharp fluctuation in the reference signal at 286 min corresponds to a large air bubble in the reference channel.

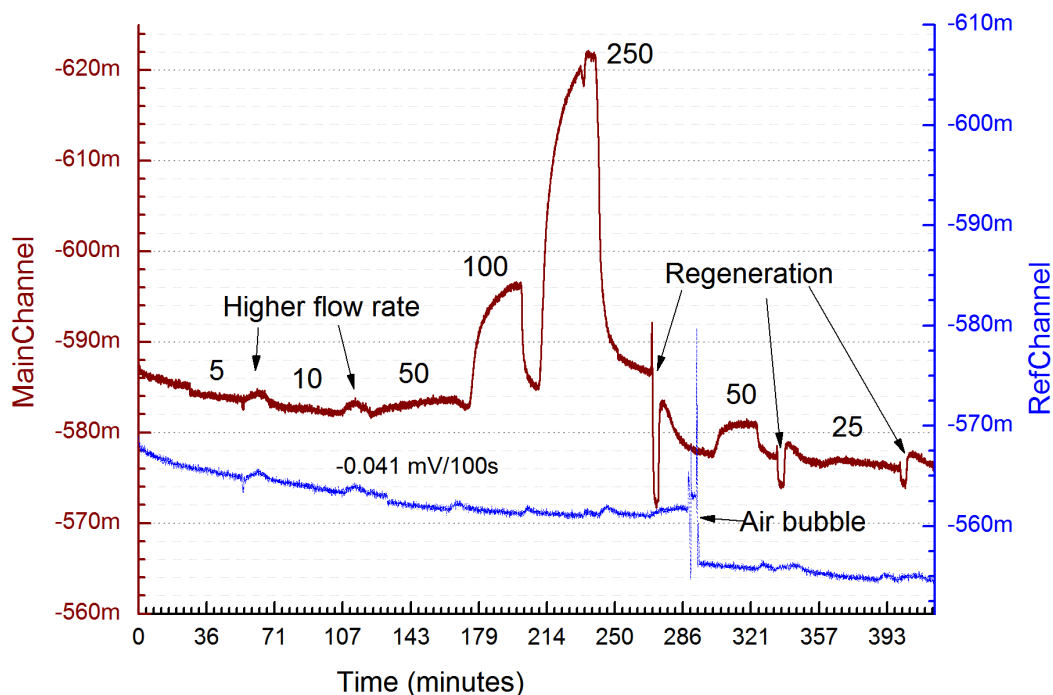


Figure 2.10: Dose-response in real time for F8BT - P1 combination. - Shows response to dose of $400\mu\text{L}$ with concentrations 5, 10, 25, 50, $250\mu\text{g/ml}$

The dose-response curve obtained by processing the data is shown in figure 2.11. Response is normalized for signal gain respect to baseline for each dose. After regeneration of the chip, a new baseline is used for calculation. Correction for PL intensity decay was applied by measuring drop on reference channel for the duration of the dose.

The limit of detection (LOD) calculated by using $3 \times \sigma$ of the baseline signal is $7 \mu\text{g}/\text{ml}$ of concentration. Taking into account total molecular weight of analyte molecule (15 MDa for P1 + 150 kDa for IgG = 15.15 MDa) it will translate to LOD = 462 pM concentration.

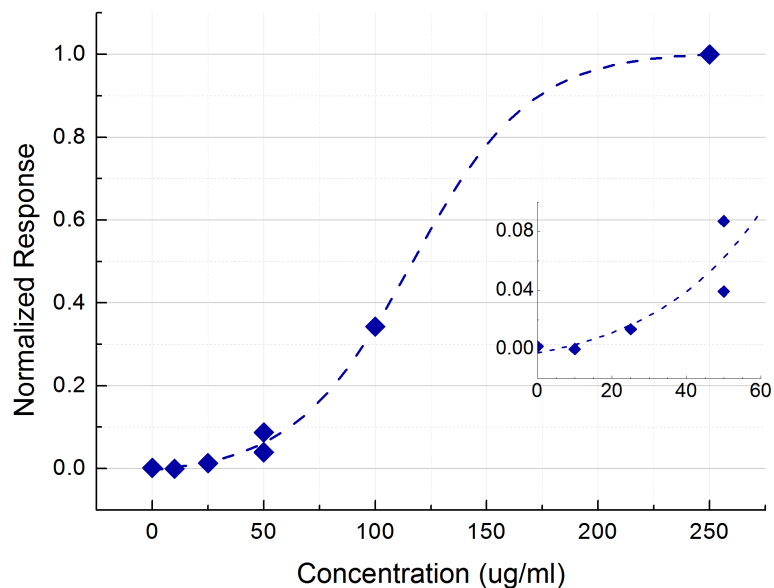


Figure 2.11: Dose Response Curve - IgG/ anti-IgG Surelight P1. The inset shows close up for low concentrations.

Photo of the complete test platform is shown in figure 2.12.

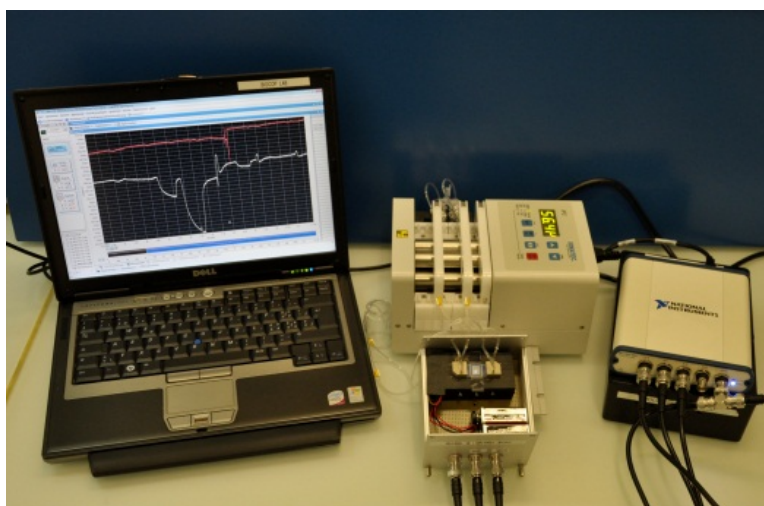


Figure 2.12: Platform test setup - Compact platform including optical chip, microfluidics and detection electronics.

2.5 Discussion

This platform has major advantage that no mechanical alignment schemes are required to in-couple light into a single mode waveguide. As measured in previous work [25] coupling efficiency of $> 30\%$ is achievable. Availability of wide range of fluorescent dyes allow matching with absorption spectrum of the analyte. Evanescent field excitation makes it highly surface sensitive detection technique. MEH-PPV as PL material has very long emission tail extending beyond 700nm. Doping and oxidation increase these low energy transitions and further broadens the tail. ADS055RE is a very promising candidate and it could still be used with by blending it with an inorganic matrix to cut down the NIR tail. Organic matrix won't be helpful because of auto-fluorescence in UV.

The dye P3 had very small Stoke Shift which was making filtering even more difficult. There switching to P1 with Stoke shift of $> 100nm$ proved very important.

Stability and lifetime issues of the PL layer have been minimized by use of F8BT. The decay of order of only a few tens of $\mu V/100s$ is achieved over entire 7 hours experiment. Major challenge to overcome is still the spectral overlap in emission regions of PL layer and the analyte. This overlap becomes dominant cause of background signal at lower concentrations.

In the next part I have compared a theoretical model in relation to BioPLC platform.

2.5.1 Comparison with theoretical model

It known that presence of a dipole close to an interface modifies the emission pattern and extensive theory has been developed by Ref. [31, 32, 33]. When the dipole is near a combination of interfaces with refractive indices n_1, n_2, n_3 such that $n_3 > n_2 > n_1$, then the dipole emissions are further modified. A model was developed and is given in the book by Novotny & Hecht, Nano-Optics [34]. They have developed analytical formulations which permit calculation of far field radiation pattern under such conditions.

Baumner et. al [35] had studied and modeled a similar system. They have used drop casted film of Rhodamine B as fluorescent dipole layer on single mode Ta_2O_5 waveguide deposited on glass (160nm thick). Figure 2.13(left) shows the definitions of various powers used in the model in the form of cross-section of waveguide (blue thin layer). Center of circle is the layer of dipoles situated on top of the waveguide ($n=2.1$). Power radiated into upper hemisphere (air) is P_{up} . Power coupled into waveguide is P_{wg} . Power in the lower hemisphere is emitted an-isotropically into two zones but symmetric around central axis. Power emitted into so called "forbidden zone" P_{fo} at angles greater than critical angle between air and glass ($\alpha_c = 43.6^\circ$). And power emitted at angles less than α_c is allowed power P_{al} . The simulation model assumes dipole at the interface, i.e. distance from dipole to interface is 0nm.

Figure on right shows calculated distribution of defined powers as a function of waveguide thickness. Since our waveguide is 150nm thick it is marked in the graph with a red vertical line. Extracted values from graph for our waveguide are summarized in table 2.1.

The power coupling efficiency from PL layer to waveguide is $\approx 40\%$. The same estimation was made by [27] was found to be 35% using model from [36]. The difference

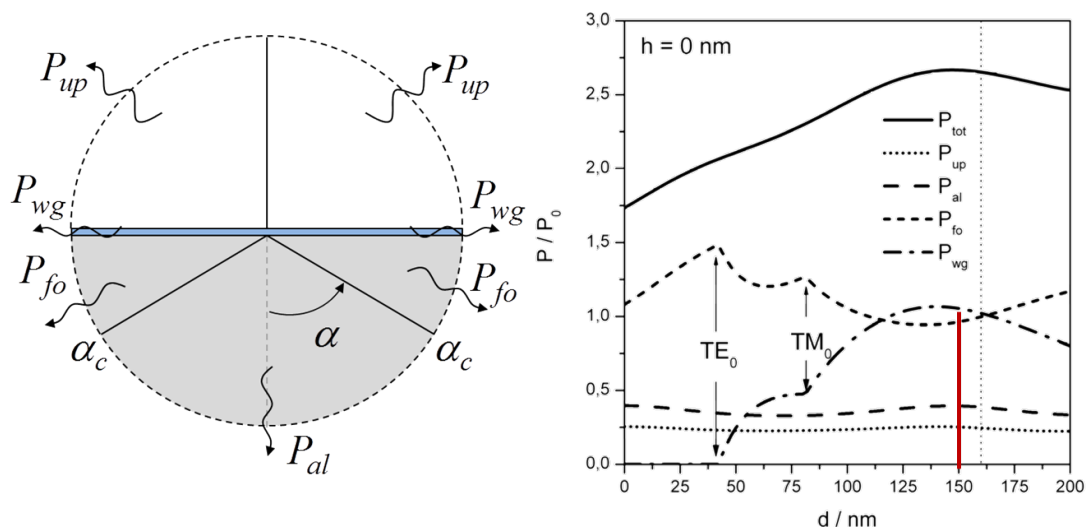


Figure 2.13: Definition of terms and calculated efficiencies from [34, 35] - (Left) shows the definitions of P_{up} , P_{wg} , P_{fo} , P_{al} , α_c (Right) shows distribution of total power emitted by a dipole at the interface $h = 0$ nm, as a function of waveguide thickness. Red vertical line is for thickness of our waveguide 150nm.

Table 2.1: Emitted power by dipole layer extracted from Figure 2.13

Power	Normalized Power	Fraction of P_{tot} in %
P_{tot}	2.67	100.0%
P_{up}	0.25	9.4%
P_{wg}	1.059	39.7%
P_{fo}	0.96	36.0%
P_{al}	0.39	14.6%

could come from underlying model, analytical vs estimation from mode density. And their model did not explain the distribution of power.

Now let's consider these calculations in our platform's scenario. Same model also applies to analyte fluorophores captured or flowing very close to surface which were excited by the guided light from PL layer. Our system measured P_{al} which is only $\approx 15\%$ of the P_{tot} . Instead P_{wg} (40%) or P_{fo} (36%) seems to be better choice to measure emitted fluorescence. PL layer emission follows same distribution but has much high power coupled-in e.g. for MEH-PPV $P_{in}=650\text{nW}$ and F8BT $P_{in}=50\text{nW}$ [27] than analyte. And due to spectral overlap in emission regions, it is impossible to selectively filter only PL emission. In case of P_{fo} , it will be guided in the glass substrate. Critical angles for PL layer and fluorophore emissions for peak wavelengths are 43° and $> 62^\circ$ respectively. This could be used as an advantage by placing absorbing layer at 43° and only detecting at $>62^\circ$. But again, the overlapping emission spectra would plague this approach as well. Long lifetime narrow emission PL material similar to ADS055RE combined with on-waveguide bandpass filters or an electrically pumped organic laser could be a better solution, could be investigated in future.

2.6 Conclusions

The platform was based upon PL coupling and evanescent excitation using a single mode waveguide. It was evaluated with multiple combinations of PL layer materials and labeled analyte which was goal of this work. Theoretical explanations of the problems were described.

The performance of current system may not be adequate for high sensitivity requirement application (LOD \approx ng/ml or better). But it does not require much hardware. Practically it can made to fit on palm size system, of course without microfluidic pump. But if there is a way to implement vertically dispensing simple fluidic assembly, the platform could be exploited in low end applications such as environmental and agricultural sensors or simple protein measurements such as albumin.

Sequence of processing steps is one of the difficulty. Functionalization of the chip is harsh process consisting ultrasonication in water, dipping in silanes, rigorous washing and heating. These can not be performed after fabrication of encapsulated PL layer at the center of chip or vice versa. During this work, a safer path of first functionalizing and then PL deposition was followed. The functionalized area was protected by fixing the microfluidic parts immediately. Since the PL material is air sensitive all remaining process steps were carried out inside the glove box atmosphere (≤ 3 ppm O_2 and H_2O). Additionally to remove any excess solvent chip was annealed at 60° for 30 mins inside the glovebox. These were non-standard steps which might have affected functionalization. But we don't see this as a major limitation because surface chemistry based on simple printing techniques are being developed[37] which can be applied after PL layer fabrication. A huge opportunity is seen for using this platform with organic lasers, especially with electrically pumped organic lasers. However the field progress has much to catch up on that front. Measurements made with this work are summarized in the following table 2.2

Table 2.2: Summary of BioPLC work

PL Layer	Capture Mechanism	Analyte	Concentration detected or LOD
MEH-PPV	Drop cast	Screenmag red fluorescent magnetic microbeads	310 $\mu g/ml$ (0.031wt%)
MEH-PPV	Primary antibodies	Surelight P3 Secondary labelled Antibodies (IgG)	100 $\mu g/ml$
ADS055RE	Primary antibodies	Surelight P3 Secondary Antibodies (IgG)	10 $\mu g/ml$
F8BT	Primary antibodies	Surelight P1 Secondary Antibodies (IgG)	7 $\mu g/ml$

3

BioCOP

3.1 Introduction

Typically optical biosensor lab-on-a-chip platform consists of three functional layers: mechanical, optical and fluid handling. Excitation light is guided to the sensing area where analyte markers are in-flow or captured. Often these layers are treated separately leading to excessive hybrid assembly costs. Absence of monolithic integration is one of the major hurdle between laboratory research and industry/consumer. Furthermore, the consumable includes a glass substrate which is costlier than plastic. For fluorescence based sensors, classical techniques involving epi-fluorescence or trans-illumination have large background signal[38]. Total internal reflection fluorescence(TIRF) microscopy drastically improve signal-to-noise ratio [39]. However dichroic mirror is a necessity for both approaches and total optical path length is large. This makes it difficult to package into a hand-held device.

Work done for BioCOP (stands for **Bio Compact Optical Point-of-Care**) platform is able to combine evanescent excitation principle along with integration of fluidics, light in-coupling and guiding optical structures into a smaller, plastic chip. The complete system has potential to fit in hand-held like form factor such as a typical tablet computer device.

Summary of challenges described above and our approach to tackle them are summarized in the table 3.1.

Table 3.1: BioCOP - Targeted challenges and proposed solution.

Challenge	Proposed Solution
Fluorescence Excitation	In-coupling gratings embossed into plastic substrate for TIRF
Microfluidic Integration	Simultaneous two sided embossing of microfluidic channel along with gratings
Mechanical Support	Substrate is monolithic - supports both optics and fluidics, also acts as chip holder as well

The idea underlying theme of the chapter is summarized in next section. A European patent has been filed based on this idea and is currently under review.

3.2 Overview of Idea

A plastic substrate with thickness t much greater than wavelength of light λ ($t \gg \lambda$) is embossed with diffraction gratings on one side. Light can be in-coupled from monochromatic source such as laser or broadband source such as LED into this waveguide using methods such as end-face coupling, prism coupling, in-coupling gratings. A simple schematic of proposed idea is shown in figure 3.1.

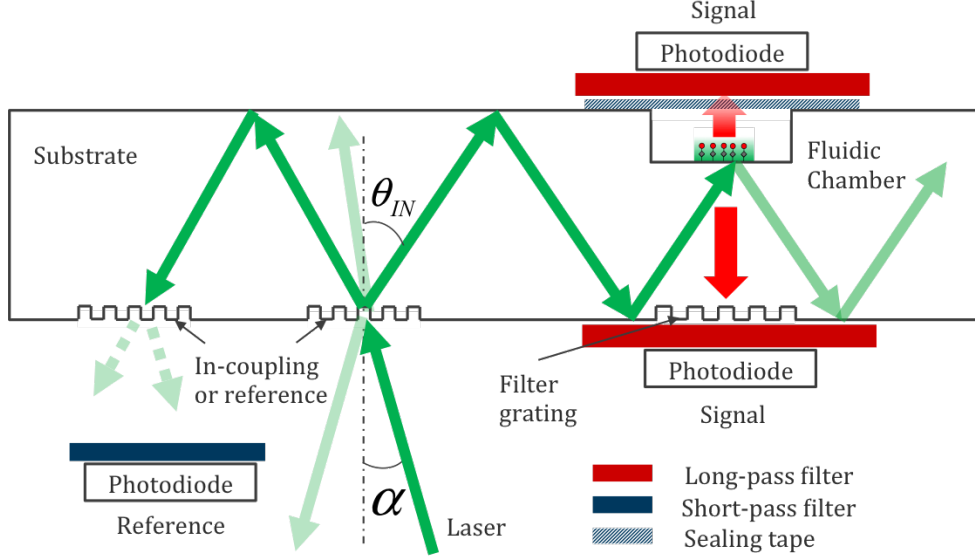


Figure 3.1: Schematic of BioCOP Chip - Coupled-in laser beam is guided by total internal reflection (TIR) and incident underneath microfluidic channel surface exciting TIRF. Gratings are used for in-coupling and referencing. Photodiodes detect both fluorescence and reference. A filter grating embossed under fluidic channel filters scattered laser.

The grating coupling offers numerous advantages. Once fabricated it is an integral part of the waveguide structure. Hence, its coupling efficiency remains constant and is not altered significantly by vibrations or ambient conditions. Grating can be coated with protective low refractive index thin films (such as MgF_2 or Cytop polymer®, $n \approx 1.3$). They can be fabricated by mass fabrication techniques such as embossing, injection molding or even roll-to-roll fabrication. Its design can be tuned and high efficiency of in-coupling can be achieved[40].

A microfluidic chamber having depth smaller than thickness of substrate ($h < t$) is embossed on the opposite side. Depth is designed such that there is enough distance for guided beam to travel underneath bottom of the chamber and other side of the chip. The channel can be sealed by a transparent adhesive tape. A laser beam incident upon in-coupling grating at angle α is diffracted into the substrate with angle θ_{in} . If θ_{in} is greater than critical angle of surrounding medium and substrate interface, then beam is totally internally reflected (TIR) and guided with minimal loss.

Placement of gratings and microfluidic on the chip are chosen such a that TIR happens at least once underneath the fluidics area. This produces an evanescent field which decays exponentially away from the interface. Though no energy is transmitted across, the field can interact with medium above the boundary. Since this field extends only up to a fraction of wavelength λ , it can interact with the molecules within short

range; typically 50-500 nm depending upon wavelength, difference of refractive index between two media and θ_{in} . If the biomolecules with fluorophores are immobilized such close vicinity, excited fluorescence could be detected by placing photodiodes above and/or below the fluidic channel.

Another grating named reference grating out-couples a fraction of guided light out of the chip used for monitoring intensity changes in guided light. A long-pass filter is used in front of signal detectors to filter out any scattered excitation light. A short-pass filter may be used in front of reference monitor filtering out any fluorescence emission. A filter based on grating is also present, fabricated below the fluidic channel. This filters scattered green light and allows to pass fluorescence emission.

In the next section we will choose materials, specifications and then design the sensor chip, hereafter referred as BioCOP Chip.

3.3 Chip Design

3.3.1 Substrate Material

It was important to choose a material which satisfies regulatory and technological requirements. Therefore hot embossing/injection molding compatibility and approval for bio-chemical sciences, to be more specific approved for IVD(in-vitro diagnostics) use; were primary criteria for selecting substrate material. It was interesting to find that there is no approved list of 'material class' from which one can choose. Documents such as EU/Japanese/US Pharmacopoeia, Bio-compatibility Test ISO 10993-5 only specify guidelines and test requirements. Every manufacturer has to submit its material for approval accordingly.

Table 3.2 presents important characteristics of materials to consider in relation to fabrication process. Acronyms are as follows: Poly(methyl methacrylate) (PMMA), polycarbonate (PC), cyclic olefin co/polymer (COC/COP), polystyrene (PS), Polyethylene terephthalate (PET) and polypropylene (PP).

Table 3.2: Relevant characteristics of various thermoplastics. T_g is glass transition temperature and Auto FL is auto-fluorescence.

Material	T_g (°C)	Auto FL @ 532nm	Birefringence
PMMA	100 to 110	Low-Med	Low
PC	150 to 160	Med	High
COC/COP	80 to 130	Low	Low
PS	130 to 150	High	Low
PET	60 to 80	Med	Med-High
PP	-10 to 0	Med	Med

Glass and plastics have inherent fluorescence known as auto-fluorescence. It creates unwanted background signal, limits sensitivity and limit of detection (LOD). Plastics have higher auto-fluorescence than glass. Due to increasing interest in fluorescence based PoC platforms few groups have extensively characterized auto-fluorescence of above listed materials[41, 42, 43]. Taking BoroFloat glass as reference; PMMA, COC and PDMS possess lowest auto-fluorescence. Since PDMS is not compatible with embossing/injection molding, COC and PMMA were short-listed. Birefringence of short-listed materials vary among manufacturers. For example TOPAS Advanced Polymers

[44] COC has lower birefringence than PMMA while [45] report the opposite for another COC make. Therefore a simple test was performed by twisting a piece of PMMA and COC observing under polarizer. Among samples of PMMA and COC in our lab COC shows least birefringence. Lower birefringence is necessary if used with unpolarized sources or else the design will behave differently for TE and TM part of the light. As a result, COC was chosen as substrate material while keeping PMMA as backup and PC as a last resort. In conclusion, COC has most desirable characteristics: low auto-fluorescence (low background), low birefringence, low water absorption and low moisture permeability(both necessary for long-term stability), high heat resistance , 0.4 - 0.7 % molding shrinkage and low out-gassing (both for hot embossing or injection molding compatibility). Low, uniform and consistent shrinkage is very important to maintain precise grating profiles after embossing.

Therefore we decided to develop the process for hot embossing on COC (TOPAS 6013M-07). Only slight disadvantage found was weak adhesive bonding without plasma pretreatment due to low surface energy of the polymer. But as is the case with many of the plastics listed above.

3.3.2 Fluorescence immunoassay

Choice of immunoassay is tricky depending upon target application, the platform used, cost involved etc. Developing an immunoassay is extremely tedious and expensive process. In order to avoid optimizing immunoassay, a simple IgG based heterogeneous assay was chosen. A whole range of fluorophores conjugated to secondary antibodies are available. A comprehensive list of fluorophores can be found on the website [46].

We chose dyes Surelight P1 and P3 developed by Columbia Biosciences. P1 and P3 dyes are extremely bright, stable and have very large extinction coefficients. Though they have large molecular weights ranging from 10-15 MDa. Immunoglobulin-G(IgG) are also quite large molecules ($M_w = 150kDa$). Each P1/P3 dye molecule can bind more than one antibodies per dye molecule¹. Since antibodies are present all around the molecule, large size does not create hindrance for binding reaction. They have been used in ultra-low molar detection assay[47, 48]. In short, they possess most desirable characteristics for a PoC device development. Table 3.3 shows summary of excitation wavelengths and corresponding dye combination for BioCOP platform.

Excitation sources are narrowed down to readily available low cost semiconductor laser diodes. Though 405nm laser is cost effective in terms of power output/EUR, it dramatically increases auto-fluorescence in plastics. At a later stage, 612/633 nm red laser and collimated super-bright LEDs could be tested.

Excitation	Wavelength	Fluorophore	Emission
Green	532nm	Surelight P1 (PBXL-1)	666nm
Red	633nm	Surelight P3 (PBXL-3)	660nm
Violet	405nm	Pacific Green/Blue	455nm / 500nm

Table 3.3: Selected fluorophores for given excitation wavelength.

Surelight P1 fluorophore with excitation source $\lambda = 532nm$ was chosen. It also give opportunity to compare BioCOP platform with BioPLC platform 2 where similar assay was used. Figure 3.2 shows relevant spectra of absorption emission of P1, 532m laser

¹answer to query from technical support at Abcam Inc.

line and responsivity of photodiode used. For validation of a bio-sensing platform

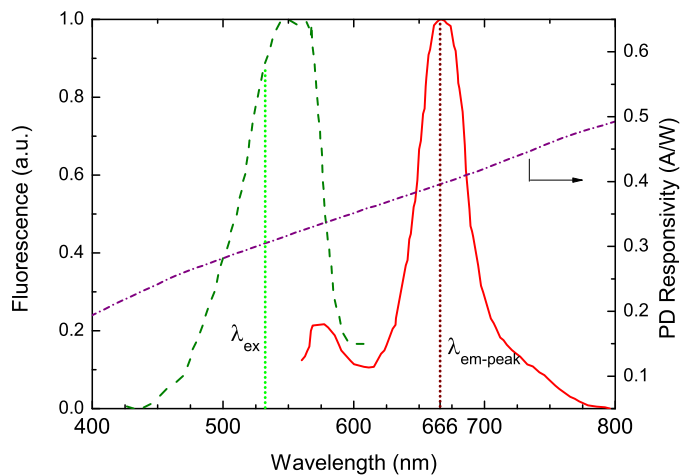


Figure 3.2: Fluorescence spectra of Surelight P1 - Plot shows excitation and emission spectra of selected fluorophore Surelight P1 along with 532nm laser and responsivity of the Si photodiode (Hamamatsu S2387)

dose-response test must be performed. Such a test could be performed either with one-dose-per-chip or serial-loading method. Normally for standard testing of an IVD one has to use former process. It involves running one chip from a set of chips applied with one concentration and many of such sets are repeatedly measured to get an idea of coefficient of variation (CV). However at very early stage of proof of concept, later approach could be easier to work with. A chip testing is started with lowest concentration to be measured and the response is recorded continuously then next concentration is applied and procedure continues until saturation or maximum concentration. Mostly chip can also be regenerated and reused. Few of such tests with same test conditions can estimate the performance of the platform. This serial-loading approach is planned to be used for BioCOP.

3.3.3 Two sided embossing

Fabrication point of view, gratings are 3-D structures of few cm^2 geometrical outline area, each element tens to hundreds of nm wide and the depth ranging from few tens to hundreds of nm. In contrast, microfluidic depth ranges from few tens to hundreds of micrometers and area outline is few mm^2 [49]. Such depth contrast makes it extremely difficult to emboss both structures on same side of the substrate while keeping accurate geometry and high throughput fabrication e.g in roll-to-roll process. Therefore embossing is made on opposite sides as shown in figure 3.1. However, this condition is neither mandatory nor is a limitation of BioCOP. In fact nanofluidics is an emerging field[50] and seen as rather an excellent opportunity to investigate in the future.

3.3.4 Total internal reflection (TIR) angle

Since the waveguide is sufficiently thick ($t \gg \lambda$ where $t > 1mm$ and $\lambda = 405, 532$ or $633nm$) we can treat the light guiding with geometrical optics model[51] Light coupled

into the substrate will be guided by TIR if incidence angle at substrate-medium interface is greater than the critical angle θ_c , i.e.

$$\theta_{in} > \theta_c \text{ where } \theta_c = \arcsin\left(\frac{n_{med}}{n_{sub}}\right) \quad (3.1)$$

Where n_{sub} and n_{med} are refractive indices of substrate and medium, respectively. Table 3.4 shows critical angles for commonly encountered optical interfaces.

Table 3.4: Critical angles θ_c for various optical interfaces including Zinc Sulphide(ZnS) and Phosphate Buffered Saline (PBS, pH=7.5)

Substrate material/n	λ 532 nm	Air 1.0003	H_2O 1.3337	PBS 1.335
COC	1.5361	40.6	60.3	60.4
PC	1.5919	38.9	56.9	57
PMMA	1.4947	42	63.2	63.3
Ta_2O_5	2.1	28.4	39.4	39.5
ZnS	2.2847	26	35.7	35.8

If θ_{in} is incident angle waveguide-medium, then condition obtained for design is: $\theta_{in} > \theta_c = 60.3^\circ$ for COC- H_2O and $\theta_{in} > \theta_c = 40.6^\circ$ for COC-Air interface.

3.3.5 Evanescent Field

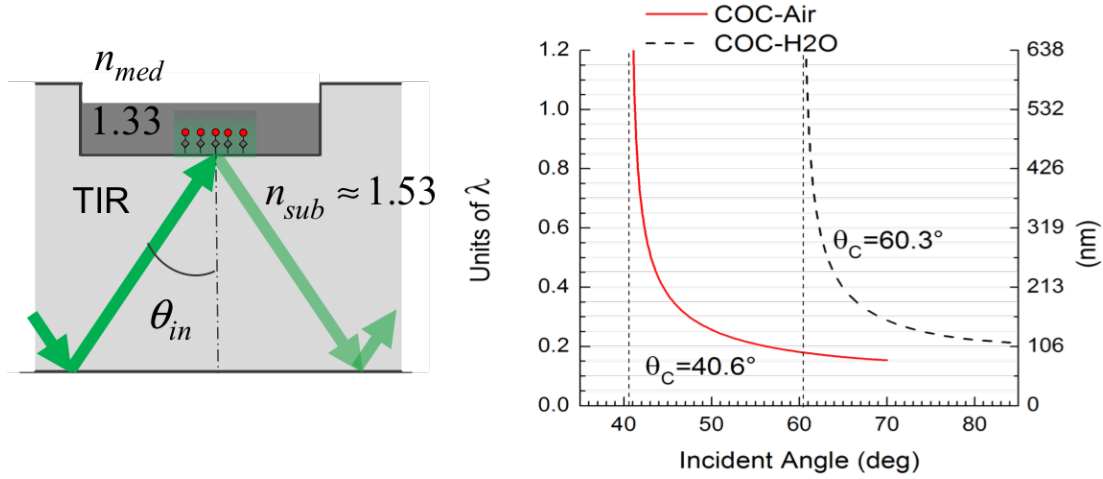


Figure 3.3: Variation of penetration depth d with TIR angle - When $(\theta_{in} - \theta_c) \approx 0.1^\circ$, $d \approx \lambda$

During total internal reflection although no energy is transmitted across the interface, an evanescent field exists at the interface. The intensity of light (in W/cm^2) decays exponentially away from the interface (along x-axis) given by,

$$I(x) = I(0)e^{-x/d} \quad (3.2)$$

where d is penetration depth in meters given by the equation

$$d = \frac{\lambda_0}{4\pi} \frac{1}{\sqrt{n_{sub}^2 \sin^2 \theta_{in} - n_{med}^2}} \quad (3.3)$$

This condition is true when no other interface (with $n > n_{med}$) is in close proximity (separation $>$ wavelength). Otherwise energy can be transferred via evanescent coupling used in technique such as slot waveguide resonators[52].

The plot of penetration depth for COC-Air and COC- H_2O interface is shown in figure 3.3

When $(\theta_{in} - \theta_c) \approx 5^\circ$, $d \approx 0.4\lambda$, and for $(\theta_{in} - \theta_c) \approx 10^\circ$ it is about 0.25λ . For highly surface sensitive technique i.e. to excite molecules very close to the interface (≈ 50 - 100 nm) small penetration depth is desired. For our sensor, a larger penetration depth means higher intensity close to interface resulting in higher fluorescence excitation. However this could also increase contribution from molecules flowing away from interface. Therefore a trade-off between signal gain over background and excited volume is necessary. While this parameter linearly controls how much volume is excited, the major determining factor is spot-size of incident beam.

3.3.6 Placement of gratings and fluidics

Following figure 3.4 shows a detailed schematic of the chip showing all the parameters required for further design calculations. At this moment, grating is considered only as entry point for the beam into the substrate at required angle θ_{in} .

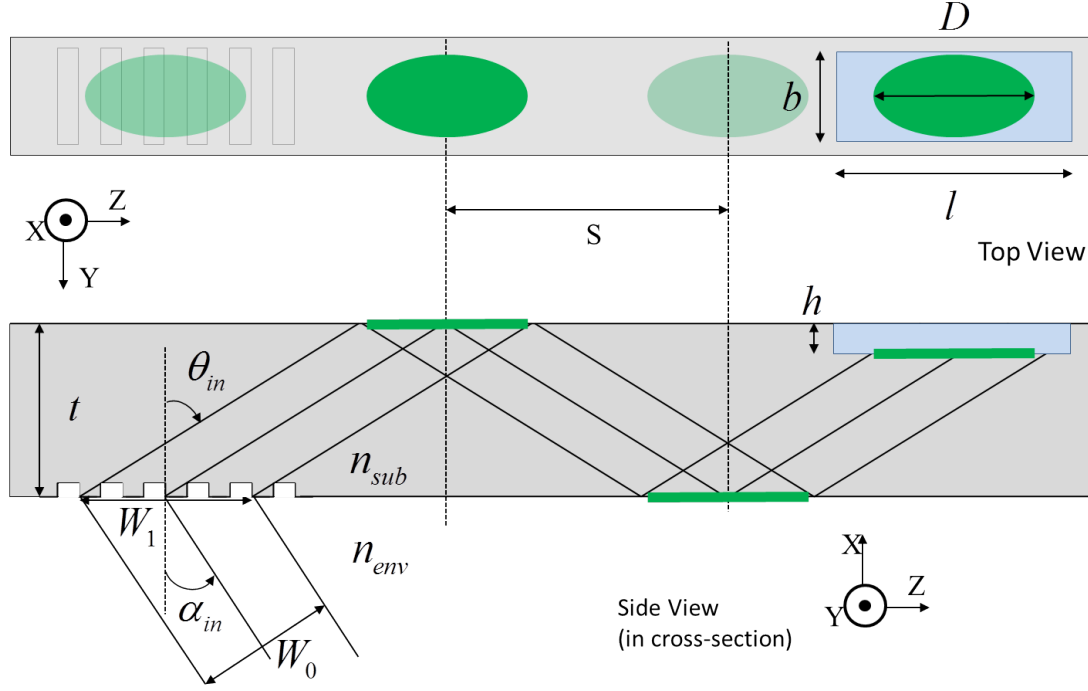


Figure 3.4: BioCOP Chip Detailed Schematic - Shows all parameters

Where,

t = thickness of the substrate

α_{in} = incidence angle on grating surface

θ_{in} = in-coupled angle into substrate

W_0 = beam width of laser output

W_1 = incident beam width for angle α_{in}

S = distance between center of two consecutive TIR spots

l, b, h = length, width, depth of microfluidics respectively

Because of non-normal incidence beam shape will expand only along one axis becoming elliptical while the other axis would be unchanged. Enlarged width W_1 is,

$$W_1 = W_0 / \sin(90^\circ - \alpha) = W_0 / \cos \alpha \quad (3.4)$$

Also the separation S between TIR spots irrespective of their side is,

$$S = t \times \tan \theta_{in} \quad (3.5)$$

If N number of TIR bounces are required for beam between grating to fluidics area, then total perpendicular distance S_{tot} between them is,

$$S_{TOT} = S(N + 1) = t \tan \theta_{in}(N + 1) \quad (3.6)$$

Since optimal θ_{in} is fixed; photodiode size, sealing tape side margin and fabrication tolerances are primary constraints.

Finally total optical path length Z_t starting from in-coupled position to the bottom surface of micro-fluidics is (figure 3.4),

$$Z_t = (N + 1)\sqrt{t^2 + S^2} - \frac{h}{\cos\theta_{in}} \quad (3.7)$$

or could also be written as,

$$Z_t = \frac{t(N + 1)}{\cos\theta_{in}} \quad (3.8)$$

3.3.7 Excitation beam width

Minimum width l_{min} of microfluidic chamber must be larger than incident beam spot-size underneath, to avoid scattering from the edges of fluidics. Some of the terms related to spot size are presented in coming paragraphs.

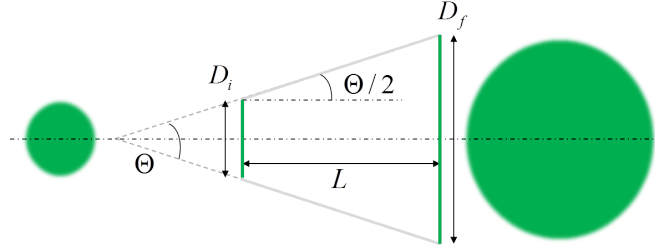


Figure 3.5: Divergence Definition - Shows schematic of spot size measured at two different points along beam axis.

Collimation of a beam is defined by its divergence. If D_f and D_i are final and initial beam diameters measured at length difference of L then full divergence angle Θ as shown in 3.5 is given by,

$$\Theta = 2 \arctan\left(\frac{D_f - D_i}{2L}\right) \quad (3.9)$$

$$\therefore D_f = 2L \tan(\Theta/2) + D_i \quad (3.10)$$

If incident spot-size on the grating is $D_i = W_1 = W_0/\cos\alpha$, then after traversing optical path Z_t , final spot-size underneath fluidic area is,

$$D = 2Z_t \tan \frac{\Theta}{2} + \frac{W_0}{\cos(\alpha)} \quad (3.11)$$

Since $\Theta \ll 1^\circ \implies \tan(\Theta/2) \approx (\Theta/2) \therefore$ the equation simplifies to,

$$D \approx Z_t \Theta + \frac{W_0}{\cos\alpha} \quad (3.12)$$

Fabrication tolerances and alignment margins also add up in the final chamber size. These values are fixed to total of 0.5mm. To get a clear picture of interdependence of these parameters, they are plotted in the Figure 3.6. For $N=4$, substrate thickness significantly affects spot size. Furthermore thicknesses 4-5mm are way too thick, also difficult for two sided embossing. preferred range is 1-3 mm. At current stage, larger

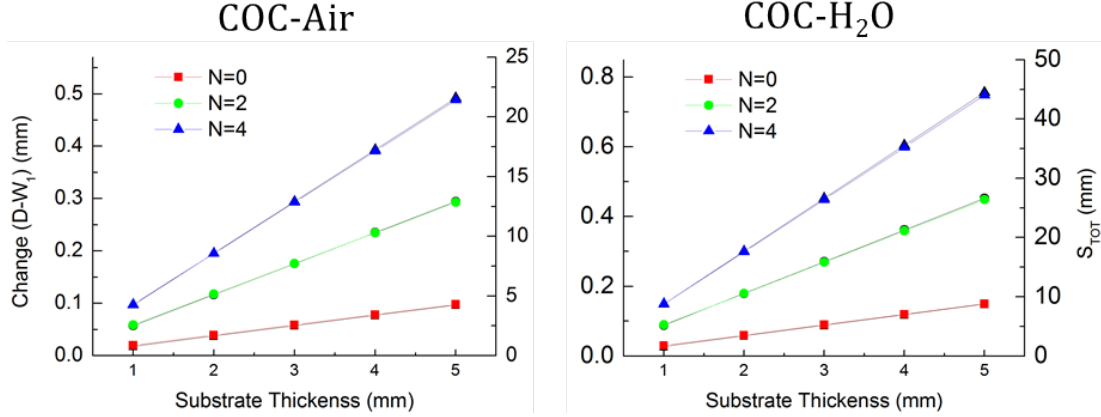


Figure 3.6: Varying parameters for design decision. - Shows increase in spot size ($D - W_1$) with number of bounces N and substrate thickness t , for both air and H_2O interface.

separation (S_{TOT}) is desirable as allows larger tolerance. Therefore $t = 3mm$ was chosen as a starting point.

The laser diode chosen is DJ532-10(Thorlabs 532 nm, 10 mW, DPSS Laser). It has divergence of 12 mrad. That means if $D_i=1mm$ then after 10 cm distance diameter would be $D_f = 2.2mm$.

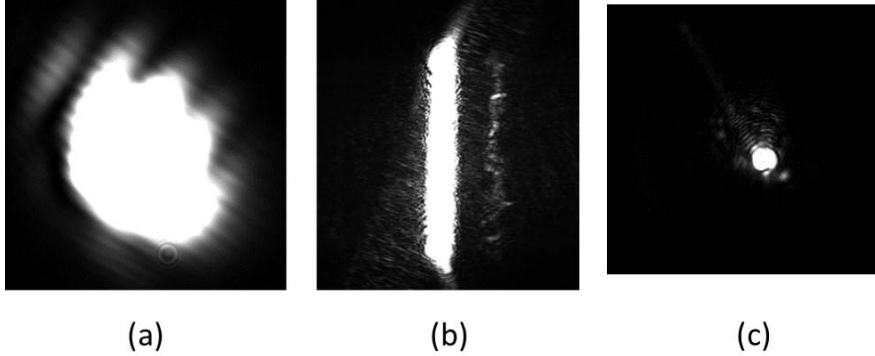


Figure 3.7: Spot size measured on CMOS imager without imaging lens - (a) Direct laser output, $L=24.5\pm 0.1cm$, $D_f = 1.24 \pm 0.1mm$ (b) Focused and recollimated into a line by two cylindrical lenses ($f = 50mm$ and $f = 5mm$), iris, $L=13.8\pm 0.1cm$ after iris, $D_f = 0.7 \pm 0.05mm$ (c) Focused by single plano convex lens $f = 50mm$, $D_f = 130 \pm 13\mu m$, $L=50 \pm 1mm$ after lens

In order to measure spot-size of our laser diode, beam was directly incident (at much lower power than 10mW) upon image sensor of a monochrome CMOS camera, without any imaging lens. Following figure 3.7 shows images obtained with different beam shaping optics. Each measurement is with same exposure time ($400\mu s$) and constant current laser driver between 135-140 mA. From (a), we can back-calculate the initial diameter of laser beam to be $900 \pm 50\mu m$.

From equation 3.6, 3.8 and 3.12 we can come up with following design considerations. Angle α influences D the most, therefore make it as close as possible to zero i.e. design grating for normal incidence or near-normal incidence. If final reader size does not increase beyond hand-held, use minimal focus-collimation optics e.g. a single aspherical lens. These considerations are summarized in table 3.5

Table 3.5: Design considerations for chip dimensions, placements of gratings and microfluidics

Priority	What to do?	Where to take care of or/and Why?
High	Reduce $\alpha \rightarrow 0$	Grating design for normal incidence
Medium	Reduce W_0, Θ	Minimal optics for beam focus and re-collimation
Low	Optimize N, t	Depends upon tolerances, S_{TOT}
None	θ_{in} is fixed	Fixed due to optimum penetration depth

3.3.8 Mask Design

Work described till here allows to design mask layout. For easy reference, mask schematic for a single chip with calculated dimensions is illustrated in figure 3.8. A single chip is $66 \times 15 \text{ mm}^2$ wide and 3 mm thick. TRIAGE system described in section 1.2.1 which is $\approx 104 \times 39 \text{ mm}^2$. By comparison BioCOP chip is 66% smaller and therefore has enough space for including additional components such as blood filter, fluidic delay lines, in the future. As mentioned earlier chip has two sides: grating and fluidics side. The in-coupling grating is situated between fluidics chamber and reference grating. These gratings can be used interchangeably due to identical design. Grating pads are kept much larger to allow linear translation of spot across the chip. A filter grating which we will discuss in forthcoming section 3.5.5, is placed just beneath the chamber on the grating side. There is adequate space on both edges (about 19-22mm) to hold the chip. Microfluidic chamber is 10mm x 1mm x 0.1mm in size and curved rectangular shaped.

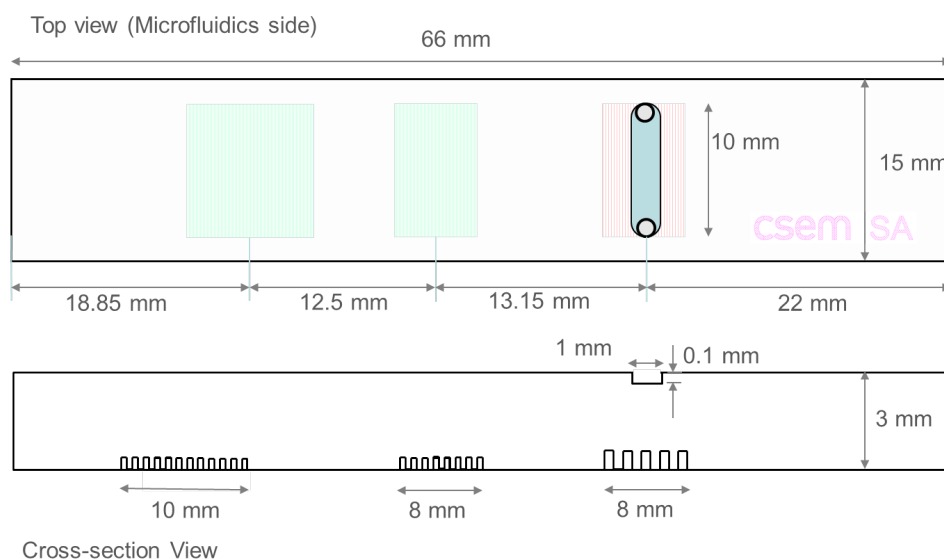


Figure 3.8: Mask schematic indicating all designed dimensions.(not to scale)
 - (Top) Top view as seen from fluidics side and (Bottom) Cross sectional view showing placement of components with respect to each other.

Figure 3.9 shows mask layouts made with CleWin mask design software. Figure 3.9 (b) and (c) shows grating side mask and fluidics mask along with their alignment marks. Figure 3.9 (a) shows five chips placed on one wafer. Embossing is typically done with Ni shims which are opaque. Due to unavailability of optical alignment, large

sized orthogonal marks are placed close to the edge of shim outline(not shown in the figure). These strategies allow manual alignment within precision of $\geq 500\mu\text{m}$. This

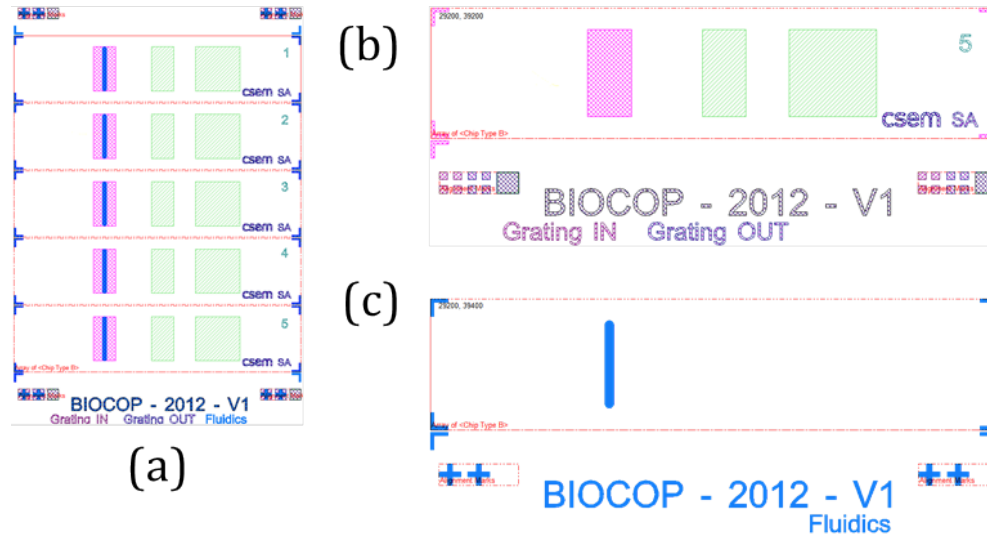


Figure 3.9: Complete 5-inch wafer mask. - (a) Shows 5 chips designed on one 5-inch wafer. (b) Grating side layout (c) Fluidics side layout

layout permits tuning of diffraction angle in the range as follows.

Using grating in the center: With $N = 2$, 49.5° to 60.8° , With $N = 0$, 74° to 79°

Using grating on side: With $N = 4$, 54° to 64°

3.4 Electrical Design

For amplifying the photodiode currents a microcontroller controlled amplifier board was designed. The gain required was in the range of $10^8 - 10^{10}$ for signal photodiode and should be easily modifiable without manual intervention such as jumpers. Therefore out of selection of all transimpedance amplifier architectures integrating, switched input one was chosen. Burr-Brown (now Texas Instruments) has monolithic version of such design with on-chip capacitor and op-amp for integration, IVC102. It has extremely low input bias current of typically 100 fA (maximum 750 fA). Required gain can be obtained by changing the integration time between 10ms to 1s and/or capacitance. Board layout was specifically designed to minimize the leakage currents to input pin of op-amp. Another design choice was to keep integration time as multiple of 20ms (for frequency 50Hz) to minimize noise coming from power lines and stray light at same frequency. The board can be operated on battery as it has been designed with high efficiency DC-DC converter on-board. Photo of the board is shown in figure 3.10. The amplifier board was named as SUPERAMP for its "Superior Performance". The microcontroller on



Figure 3.10: - Implemented board of SUPERAMP. Third channel is not soldered.

board was selected from AVR ATmega series. A watch crystal (32.768 KHz) was used as time base for control waveform of the IVC102 amplifier. This provided low drift and stable timing for amplification. The firmware for the microcontroller was written in C programming language using CodeVision AVR studio. The board has trigger input to start amplification cycle and trigger output to indicate end. It can also be put into low power mode while keep running amplification process. A 3-channel version was designed for BioCOP and another 6-channel one was designed for project Photo-FET (next chapter). Typical control and amplification waveform with 500ms integration time are shown in figure 3.11. Waveform on left is for dark mode and right one is under ambient illumination. Channel 1 and 2 (yellow and cyan) are control waveforms from controller while channel 2 (pink) is for amplifier. In dark the amplified voltage is about $\approx 15\text{mV}$ meaning $\approx 3\text{pA}$ current.

For another test for amplifier we connected a near perfectly dark photodiode (fixed inside an sealed steel tube and contacts brought outside by a coaxial plug) to the amplifier. Same photodiode was also measured with a high resolution source measurement unit (SMU) Keithly 2636 and tri-axial cable. With SMU we measured photo-current of $\approx 200 - 300\text{fA}$. Using our amplifier we measured voltage of $\approx 10\text{mV}$ for 1s integration

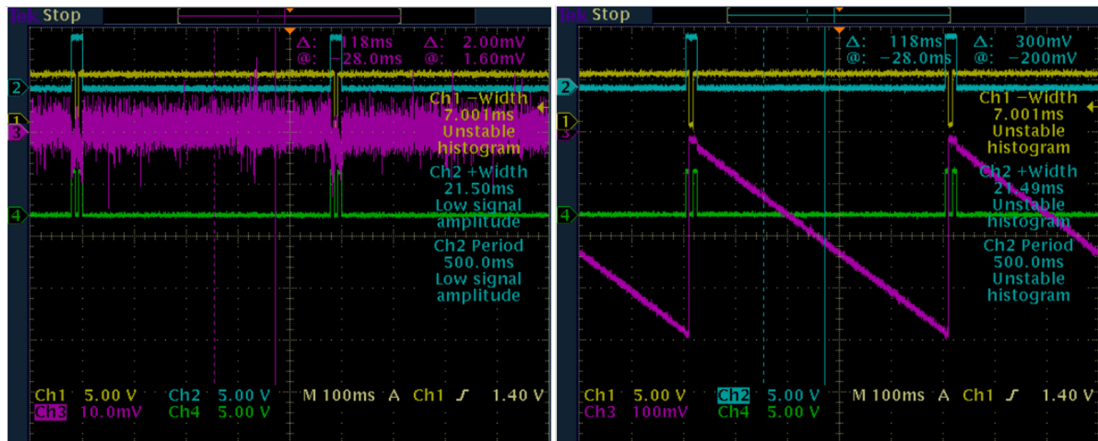


Figure 3.11: - (left)Dark (right)Under ambient lighting conditions.

time and 100pF capacitor which translates to measured dark current of $\approx 900fA$. This was done at 24°C temperature. The difference between SMU and amplifier measurement could come from shift from tri-axial to coaxial connection to the board.

3.5 Grating Design

In this section, important aspects of grating design are introduced first. Then a range parameters are calculated and finally simulation results and fabrication specifications are presented.

3.5.1 Grating Performance Parameters

Optical diffraction gratings are typically fabricated as periodic variation of refractive index. They can work in reflection or in transmission mode. Figure 3.12 shows a typical transmissive grating embossed into a substrate with refractive index n_{sub} and surrounding medium index n_{med} . A grating can diffract a single wavelength at multiple angles allowed by equation 3.13. These are called diffraction orders.

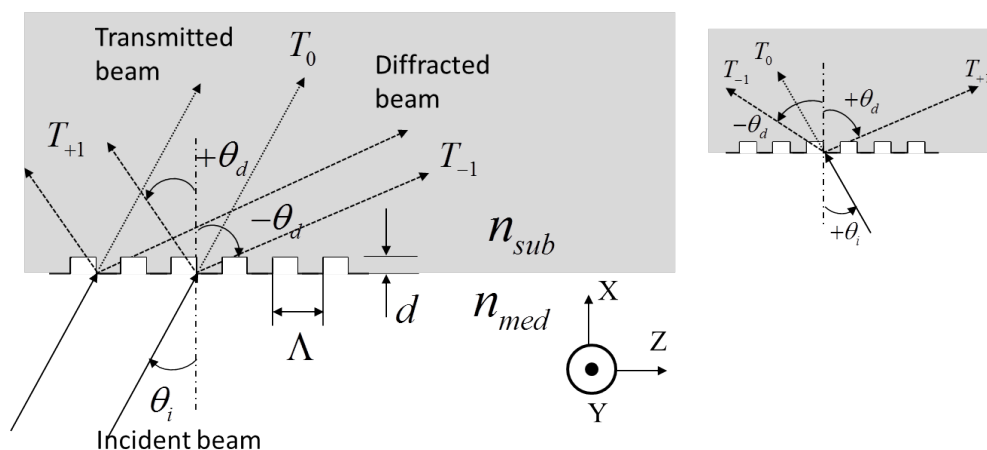


Figure 3.12: Typical transmission grating - It has rectangular profile with period Λ , depth d . T_0, T_{+1}, T_{-1} shows transmitted order $m=0, +1$ and -1 . Specular reflection R_0 is not shown. Diffracted orders on the same side as the normal w.r.t. T_0 are +ve, opposite side are -ve. Angles on the same side of normal are positive otherwise negative.[53]

Grating equation

The angular relationship of the diffraction orders generated by a grating is given by,

$$(n_{med} \sin \theta_i - n_{sub} \sin \theta_d) = \frac{m\lambda}{\Lambda} \quad (3.13)$$

The index m is the mode or diffracted order number. Grating period is Λ , θ_i and θ_d are incident and diffracted angles respectively. The sign convention in the equation assumes that angles on the same side of grating normal have same sign. For orders, m is positive if it is on the same side as grating normal with respect to 0^{th} order beam. In figure 3.12, transmitted orders T_0, T_{-1}, T_{+1} and reflected order R_0 are shown. Direct transmission or specular reflection is 0^{th} order which always exists. Existence of remaining orders for given λ depends upon Λ and incident angle. This equation is valid for incidence from air ($n=1$).

Diffraction Efficiency η

For a particular mode, it indicates how much of incident optical power is diffracted into that mode. Efficiency decreases with increase in mode number, if other parameters are kept constant[53]. Hence, first order gratings are used to maximize η and in turn

total optical power coupled into substrate. Calculation of diffraction efficiency is not trivial. It is function of many parameters such as grating depth, polarization and wavelength of incident light, refractive indices of materials involved. Therefore rigorous electromagnetic techniques are used to calculation of efficiency.

Dispersion

When a poly-chromatic light beam is incident upon the grating, it will disperse optical spectrum into it's individual wavelengths. For single wavelength laser diode dispersion is not relevant. A collimated LED beam combined with a bandpass filter could be a viable option however more analysis is needed.

Most useful form of dispersion relation is,

$$\frac{d\theta_d}{d\lambda} = \frac{m}{\Lambda \cos \theta_d} \quad (3.14)$$

Free Spectral Range (FSR)

FSR is band in input spectrum where wavelengths from adjacent diffraction orders do not overlap. When using LED it calculates specifications of bandpass filter. To avoid overlap for m^{th} order FSR must be at least,

$$\Delta\lambda_{FSR} = \lambda_{long} - \lambda_{short} = \lambda_{short}/m \quad (3.15)$$

Stray Light

Manufacturing of gratings is not perfect which causes some of the light scattered into unwanted directions. This stray light is unfocused and may propagate in random directions. Such scattering emerges from defects, unclean surface and other regular or irregular features. For small period gratings $\Lambda < \lambda$ stray light is more pronounced. Periodic defects in groove structure produces stray light which is focused along with diffracted orders. Such stray light will be important for PoC sensor as it will impose more work on the spatial filters. In this work proper handling precautions are taken. However thorough measurement and analysis of stray light is not carried out.

All properties explained until this point are summarized in the following table 3.6.

Table 3.6: Diffraction grating properties

Property	Definition	Determined by
Grating equation	$\sin \theta_i + \sin \theta_d = \frac{m\lambda}{\Lambda}$	m = mode number, Λ =period
Efficiency	how much of incident optical power is diffracted into given mode	groove profile; (n,k) of surface material, grating depth and period; polarisation and wavelength of incident field.
Dispersion	variation of diffraction angle θ_d with wavelength, α constant	$\frac{d\theta_d}{d\lambda} = m/(\Lambda \cos \theta_d)$
FSR	band over which the wavelengths from adjacent orders do not overlap.	$\Delta\lambda_{FSR} = \lambda_{long} - \lambda_{short} = \lambda_{short}/m$

3.5.2 Zinc Sulphide (ZnS) High Index Coating

High index dielectric over-coatings increase field confinement inside the grating which in turn, if designed properly could enhance diffraction efficiency. The evaporation conditions affect the index of thin dielectric coating. Additionally how thick coating is formed also affects the grating performance under non-idea evaporations. Dielectric coating of zinc sulphide ($n=2.2847$ @ $\lambda = 532nm$) is used during simulations and fabrication. Following figure 3.13 shows the grating geometries fabricated ($\Lambda = 440nm$, depth $\approx 320nm$) with no ZnS coating and with 80nm and 150nm coating thickness. Thermal evaporation technique is used with boat to substrate distance of approximately 50cm at pressure $< 5 \times 10^{-5}mbar$.

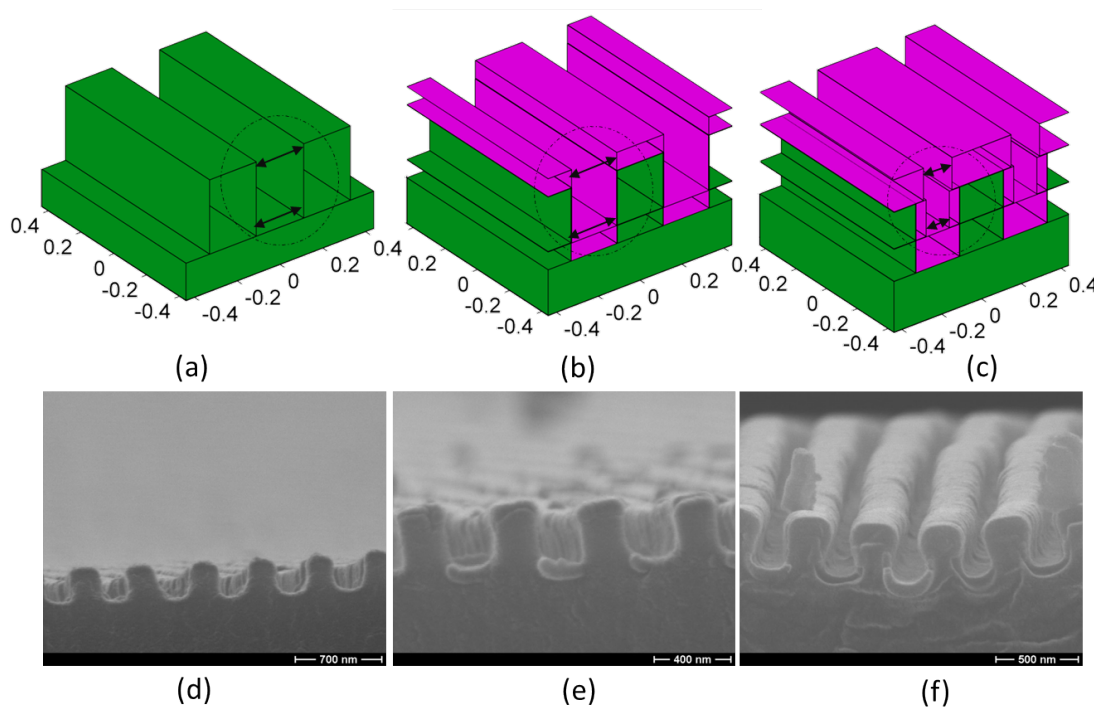


Figure 3.13: ZnS coating on embossed grating - $\Lambda = 440nm$, depth = $320nm$ First row images (a)No ZnS, (b)50nm(c)150nm shows simulation profiles approximating the real structures in the images on second row. (d)ZnS=0nm Square profile is maintained(e)50nm ZnS, Negligible sidewall has formed.(f)150nm ZnS larger sidewalls and mushroom like structures are formed. (SEM images obtained from Mr. Fabian Lütolf, fellow PhD student at CSEM SA.)

As observed from figure 3.13 (d), embossed grating is rectangular. After evaporation of 50nm of ZnS, the groove profile is maintained with a negligible sidewall. However as ZnS thickness is $\approx 0.5\lambda$, it has formed significant sidewalls and in turn changing the effective period of the grating. A simple linear relationship model is included in the simulation for creating grating geometry (thanks to Mr. Guillaume Basset, R&D Engineer at CSEM SA). A parameter named WallT (abbreviation for "sidewall thickness") is introduced during layer-by-layer shaping. It calculates the sidewall as fraction of thickness/period ratio. Simulation geometry in Figure 3.13 (b) is with 5% sidewall and (c) is with 25% sidewall. The effect on chip performance due to this non-uniform evaporation is discussed in later sections.

(Note: The machine here is small and only used for thin ZnS layers for quick prototyping. For large multi-wafer evaporation with thicker ZnS, an industrial scale chamber is usually used. Due to some unavoidable circumstances larger evaporator was unavailable. As a consequence smaller machine was used during fabrications of samples for this project. Therefore this section is relevant for discussion.) Parameters of gratings in simulations that can be optimized are: **depth, thickness of ZnS coating and period**. For quick reference final design specifications are summarized in the following table 3.7.

Table 3.7: Final Design Specifications for design wavelength $\lambda=532\text{nm}$

Specification	Symbol	Value
Design Wavelength	λ	532nm
Refractive Index	n_{SUB}	1.5361
Grating Period	Λ	(for air) 266nm - 817nm (for H_2O) 266nm - 612nm
Incidence Angle	α	close to 0 deg
Diffraction Order	m	+1 or -1
Diffraction Angle θ_{in}	Air-COC	>40.6
	H_2O -COC	>60.3
In-coupling efficiency	η	Maximise for given diffraction angle θ_{in}

3.5.3 Grating Simulations

Designing for first-order gratings is important to maximize power coupling into the waveguide. From equation 3.13 we can deduce the range for grating period. Grating equation induces condition $(m\lambda/\Lambda) \leq 2$ for additions of two sines to be meaningful. For $\Lambda < \lambda/2$, the grating acts as zero-order grating, no first order exists. If $\lambda/\Lambda \ll 1$ i.e. period much larger than wavelength, large number of diffraction orders will exist. Therefore for 1st order ($m=\pm 1$) gratings, $\lambda/2 < \Lambda < \lambda$ is appropriate range. As a result, boundary values for our grating period are $266\text{nm} \leq \Lambda \leq 531\text{nm}$.

Purely analytical models for diffraction efficiency calculation do not exist. Therefore they are simulated with Rigorously Coupled Wave Analysis(RCWA) technique[54]. GD-Calc®, a Matlab based RCWA library package was used. Simulation process steps are as follows - specify grating geometry in Matlab code, define incident field, GD-Calc then calculates scattered reflected and transmitted field for each diffracted order and in turn η can be calculated. Gratings fabricated within this work are fairly rectangular and symmetric (duty cycle $\approx 50\%$).

Range of incident angles are calculated using lower limit for diffracted angle as θ_c using grating equation 3.13. They are summarized in the table 3.8.

Top half of table 3.8 is for COC-Air interface and useful reference for dry phase assay. While bottom half is for COC- H_2O interface for wet phase assay.

3.5.4 Simulation results

Simulations were performed for range of periods, depths and ZnS thicknesses (thanks to Dr. David Leuenberger for help, R&D engineer at CSEM SA.). All simulations are

Table 3.8: Incident angles and corresponding diffracted angles for each grating period. This range provides penetration depth of in the range $\approx \lambda$ to $\lambda/4$. T_{-1} order will be used only for monitoring in-coupled light.

Period nm	Incident Angle degree	$\theta_{in} (T_{+1})$ degree	$\theta_{in} (T_{-1})$ degree
<i>COC-Air</i>			
340	-34 to -20	40.8 to 52.7	NA
380	-23 to -10	41 to 53	NA
398	-19 to -6	41.1 to 53.3	NA to -69.7
440	-11 to 0	41.5 to 51.9	-65.7 to -51.9
500	-3 to 8	41.1 to 51.5	-46.6 to -37
<i>COC-H₂O</i>			
340	-13 to -4	60.7 to 76.7	NA
380	-4 to +5	61.1 to 75.5	-73.1 to -58.7
398	0 to 8	60.5 to 73.9	-60.5 to -51.2
440	8 to 15	61.4 to 72.8	-44.1 to -38.2
500	16 to 24	60.7 to 73.2	-30.8 to -25.3

made for unpolarized laser beam. Optimal results obtained are shown in following figure 3.14. Top part of the plot depicts the diffraction efficiency map of T_{+1} as function of wavelength, incident angle. Bottom part shows resultant diffracted angle map. Thin red line in the graph is guide for $\lambda = 532$ nm. Grating parameters are: period $\Lambda = 340$ nm, grating depth $d = 200$ nm and ZnS coating of 170 nm. As seen from the map, at 532 nm with incident angle of -13° to 0° we achieve peak diffraction efficiency. The diffracted angle is close to critical angle.

A detailed mapping of diffraction efficiency ($\approx 50\%$) with design wavelength 532 nm is shown in figure 3.15. Period 320 nm $\leq \Lambda \leq 360$ nm gives optimal performance within all set specifications.

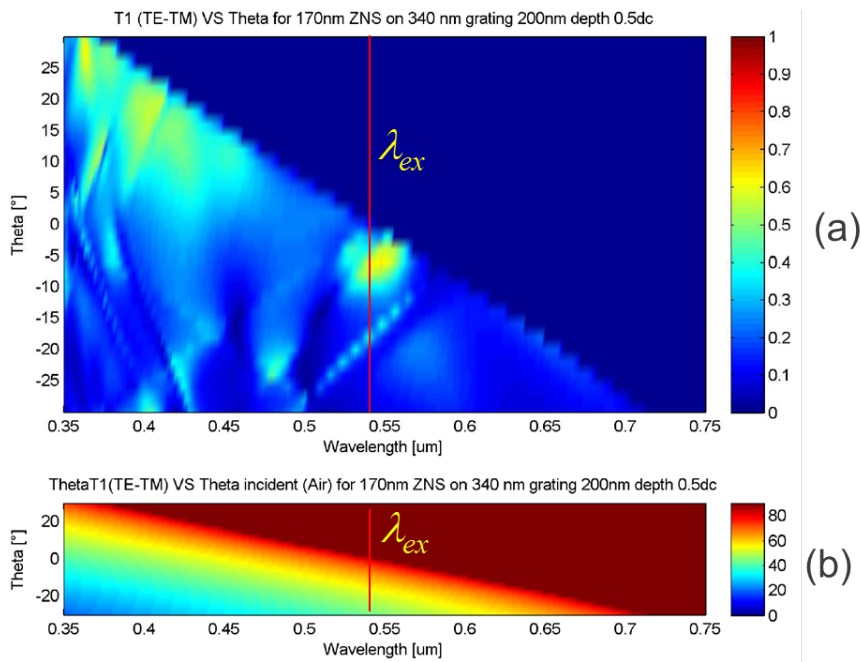


Figure 3.14: Diffraction efficiency map - (a) Grating geometry in 3D. Substrate is COC(green), ZnS overcoating and medium around is air (b)diffraction efficiency of unpolarized T_{+1} order as function of incident angle and wavelength. (c)Diffracted angle variation. Red line marks the $\lambda=523\text{nm}$.

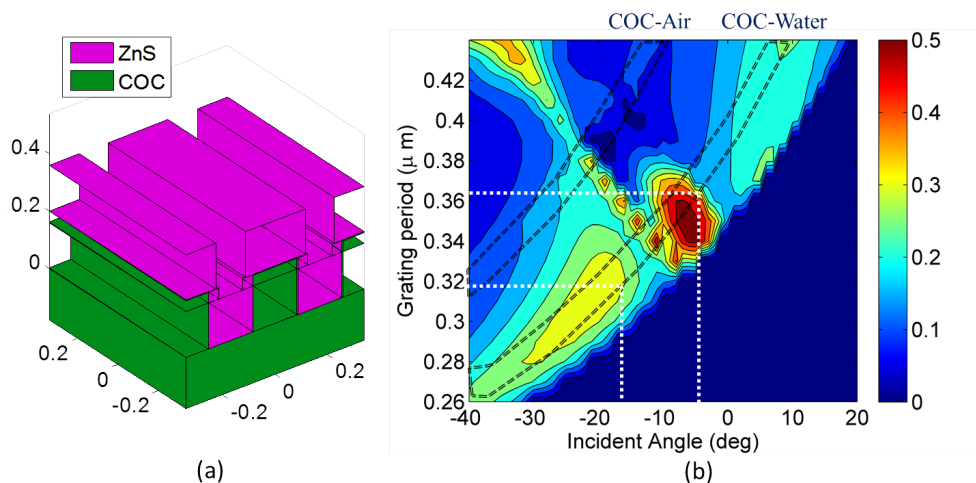


Figure 3.15: Diffraction efficiency map - $\lambda = 532\text{nm}$, depth=200nm, ZnS 170nm, Black dotted area are guides for useful diffraction angle range. White lines are ranges for maximum and minimum grating period and corresponding incident angles.

3.5.5 Grating filter

Resonant grating filters are widely used for filtering out lasers. In our sensor chip, we decided to try out integration of such a grating based filter. Figure 3.16 shows the way this concept was tested.

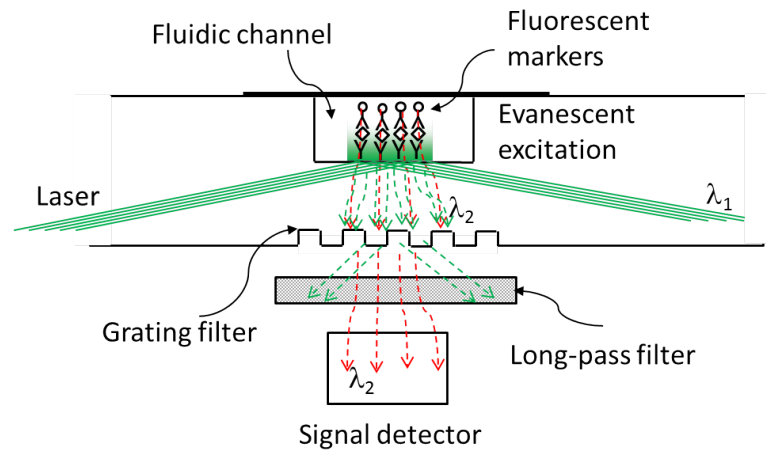


Figure 3.16: Position of grating filter in the chip. - Laser light scattered due to fluidics surface will be rejected by filter while wavelength $> 600nm$ will be transmitted.

Here the requirement on the filter was to reject any scattered green light (532nm) at normal incidence or any direct transmission (T_0). It should allow to pass light of wavelength greater than 600nm i.e. the emission band of the fluorophore.

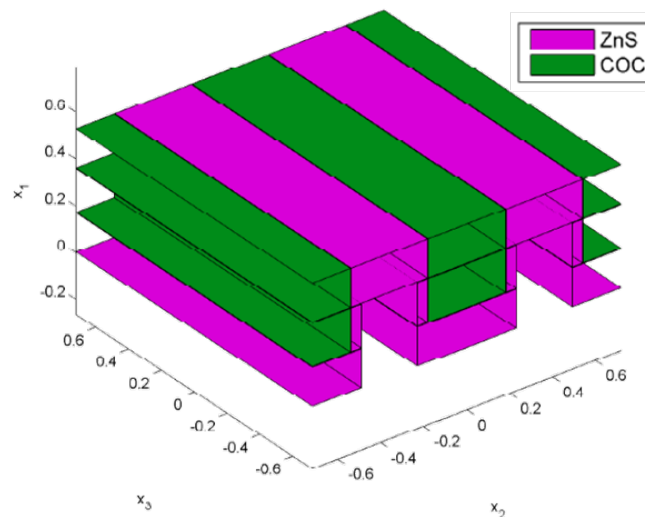


Figure 3.17: Filter grating simulation geometry. - Being out-coupling structure, it is upside down. Top part is COC then ZnS coating and then at the bottom is air.

The simulation geometry used for filter grating is shown in figure 3.17. Simulation results are displayed in 3.18. Simulations show that for 0^{th} order, incidence angle bands 0° to $\pm 15^\circ$, ± 25 to $\pm 55^\circ$ are blocked effectively. Due to narrow incident angle regions where it allows to pass green light we need to use long-pass filter. $T_{\pm 1}$ orders are not dominant. We note that filter grating with current design can not eliminate longpass filters used in front of photodiode. It will act as a supplement integrated into the chip.

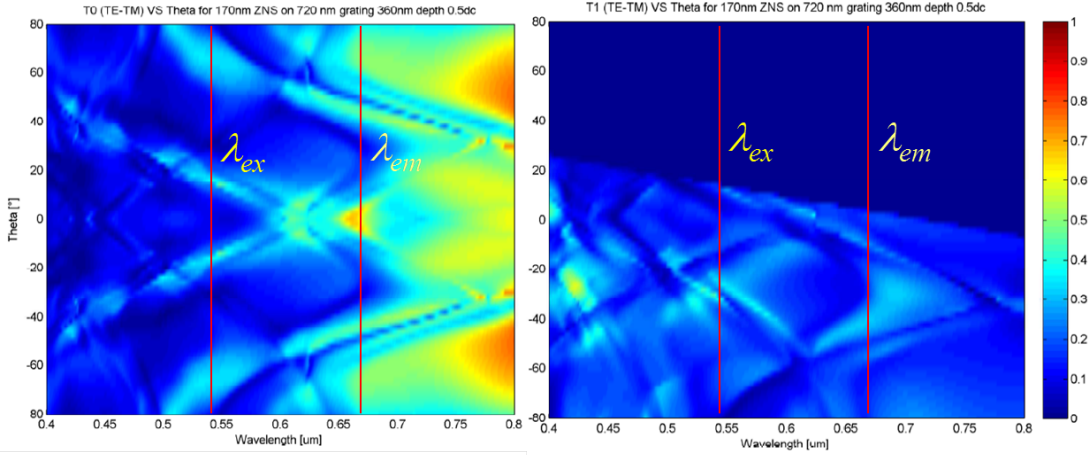


Figure 3.18: Diffraction efficiency maps of filter grating. - $\Lambda = 720nm$, Depth = $360nm$, ZnS thickness of $170nm$. (left) T_0 order direct transmission fluorescence emission ($> 665nm$) is coupled out with $> 60\%$ efficiency (right) T_{+1} order is non-dominant for both $532nm$ and $> 666nm$

Finally, table 3.9 summarize the fabrication parameters for in-coupling and filter grating.

Table 3.9: Fabrication Parameters

Parameters	In-coupling/reference grating	Filter grating
Period Λ	320 - 360nm	720nm
Depth d	200nm	360nm
Duty Cycle	50%	50%
Overcoating ZnS	170nm	170nm

3.6 Fabrication of Chip

The gratings are fabricated by holographic exposure of photoresist on quartz substrate. Test structures embossed into sol-gel from such a quartz substrate are shown in figure 3.19 as SEM cross-section. These structures are then etched into quartz to achieve specified grating depth. The sinusoidal groove shape made during holography is made into square by in-house process on master nickel shim (Ni-shim). More replica of master shim are made for use during actual embossing process. Both the in-coupling and filter gratings are fabricated on the same substrate by two holographic exposures for two different periods. Respective grating pads are made using the mask designed in previous sections. Using the process described above, in-coupling/reference grating shim with $\Lambda = 340nm$, depth = $200nm$ and filter grating shim with $\Lambda = 700nm$, depth = $360nm$ were fabricated.

The process for microfluidics Ni-shim with structure depth of $100 \mu m$ was developed. Mask layout for the microfluidics chamber is rounded rectangle in shape with length $l = 10mm$, width $b = 1mm$ and depth $h = 0.1 mm$. The pattern was printed on a transparent foil with very high resolution ($3600 dpi$). This test pattern was transferred onto a chromium mask by UV photolithography. Mask pattern was transferred into a

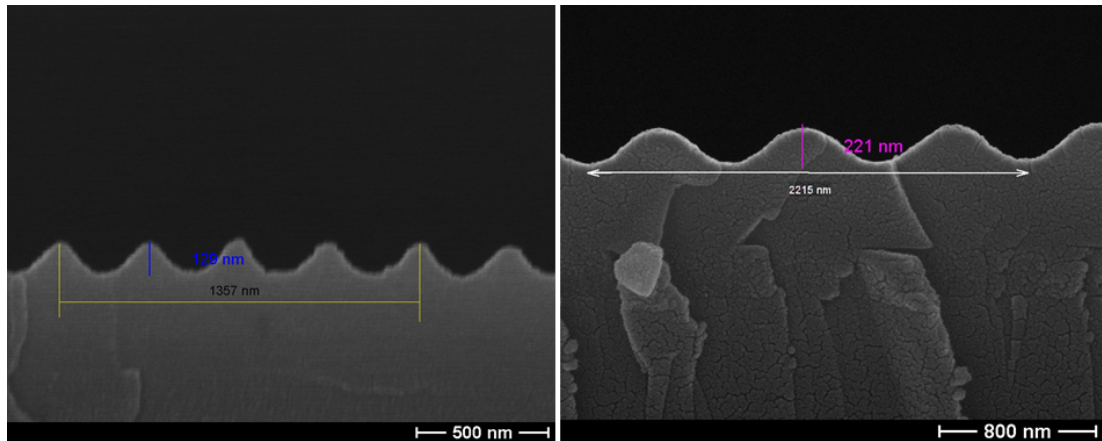


Figure 3.19: SEM cross-section of embossed test substrates from quartz masters - (Left) In-coupling grating $\Lambda_{meas}=340\text{nm}$, depth = 129nm (right) Filter grating $\Lambda=738\text{nm}$, depth = 221nm

thick photoresist (SU-8 or likewise) deposited on a blank Ni-shim. After development of resist $100\mu\text{m}$ nickel was grown to match the depth of fluidics. Finally resist was stripped to complete the process. Figure 3.20 shows SEM of final resist pattern before final Ni growth was performed.

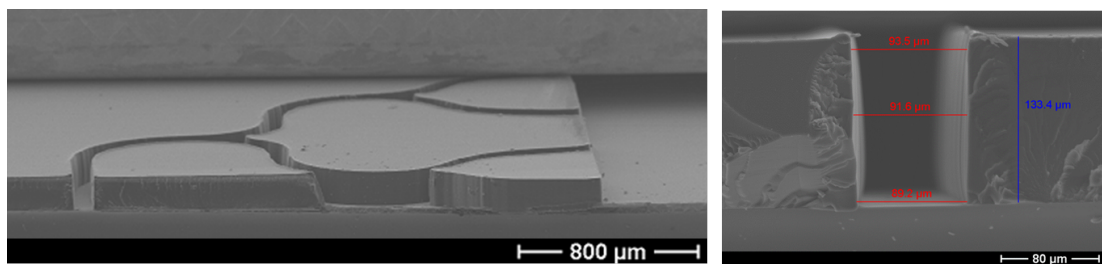


Figure 3.20: Fluidics transferred into resist on a Ni-shim - Shows clear and smooth surfaces on sides and bottom surface.

For embossing of BioCOP chip, a COC substrate (3 mm thick, 5 inch square) was sandwiched between glass plate, Kapton®tape, silicon sheet and Ni-shim from both sides. The process of hot-embossing was carried out in an embossing machine by pre-heating at 90° and then heating above the glass transition temperature of COC ($160\text{--}190^\circ\text{C}$) at full load of 35kN. After the process is complete the sandwich was removed out of the machine and de-molded close to room temperature. Embossed substrate were immediately protected by blue adhesive-less foil on both sides. Grating side was evaporated with 170nm ZnS in either of the chambers mentioned before. Following figure 3.21 (b),(c) shows final fabricated chip from grating and fluidics side respectively. Figure 3.21 (a) is provided as a reference for mask layout.

Another design of mask containing fluidic chamber along with passive fluidics lines and inlet/outlet reservoirs was fabricated. The mask layout and final fabricated chip with same procedure before are shown in figure 3.22.

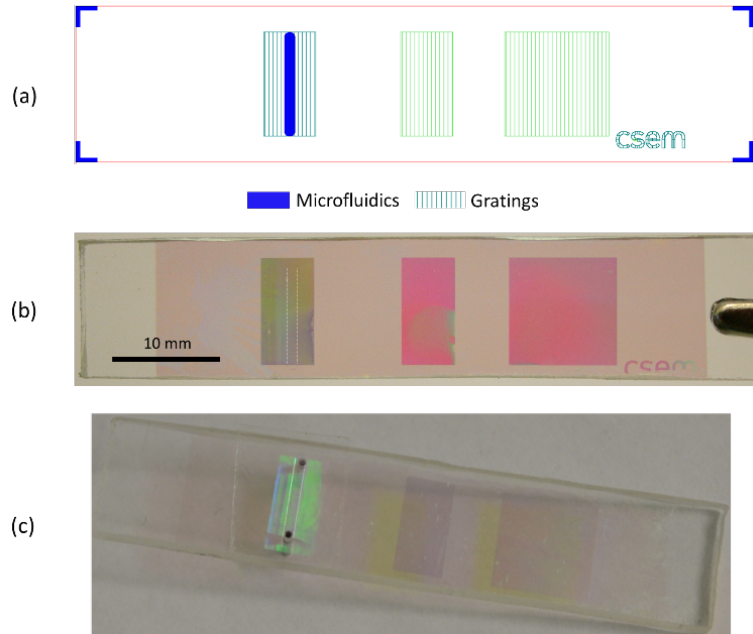


Figure 3.21: Fabricated chip photos along with mask reference for single chip.
 - (a) Shows the mask layout for a single chip for both fluidic and grating layers (b) and (c) shows photos of the chip from grating and fluidic side respectively.

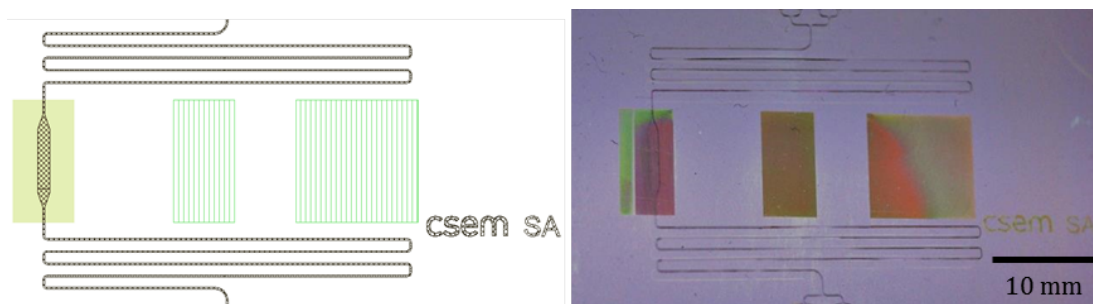


Figure 3.22: Chip with passive fluidics design. - Left image shows mask layout and right image shows photo. Dimensions for placement are same as in small chip, except with the addition of fluidic delay lines. Reservoirs are not completely visible.

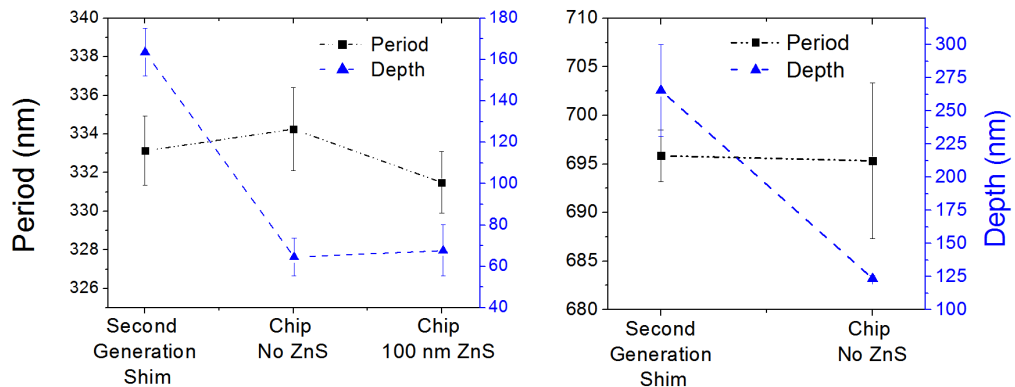


Figure 3.23: Grating characterization AFM statistics - Left graph shows data for 340nm grating (reference and in-coupling). On right is the data for 700nm grating (filter)

3.7 Characterization

Grating surfaces on the final chip were characterized by Atomic Force Microscopy (AFM). Some of the images from AFM analysis are given in appendix . For comparison, gratings on a second generation Ni-shim, chips fabricated without ZnS and with ZnS are profiled. The results obtained are presented in following figure 3.23

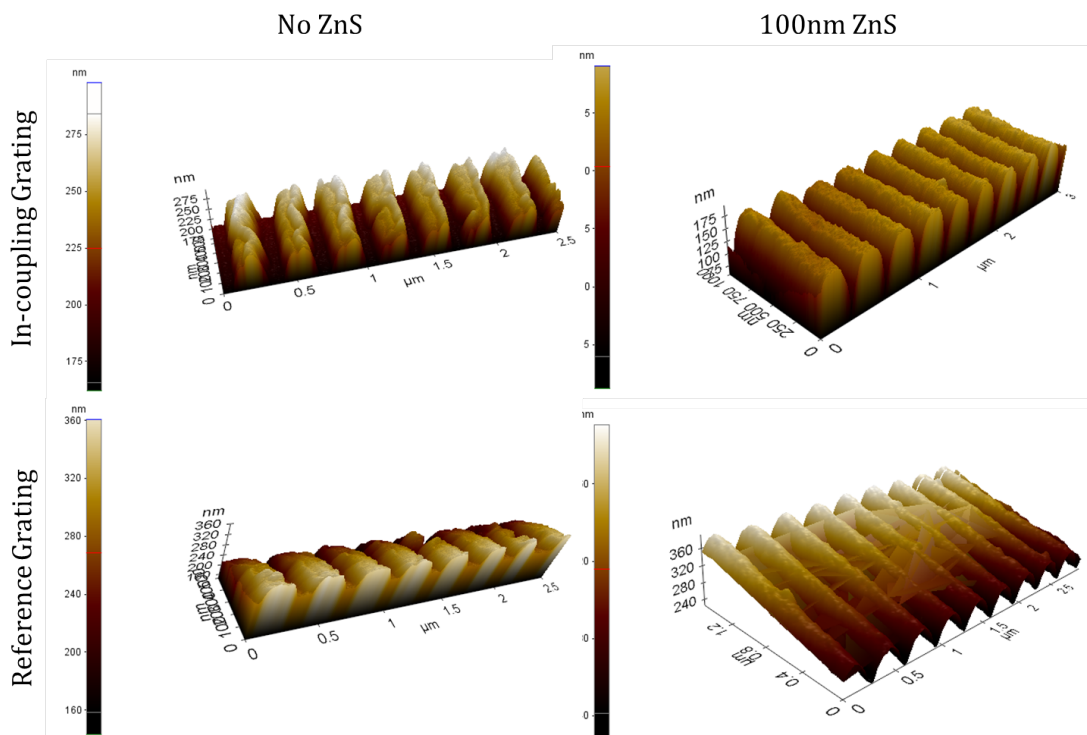


Figure 3.24: AFM Images of in-coupling and reference grating -

Second generation shims were close but not exactly to the design specifications. For 340nm grating, mean period = 333nm, depth=160nm and for 700nm grating, mean period=700nm, depth 227nm. After embossing into COC though grating period remained

fairly the same, depth had downfall of more than 50%. Shim quality problems were due to nickel galvanization machine which had recovered from a recent breakdown. For 340nm gratings, a small change of period was observed. This perceived change in period is due to "sidewall formation" as discussed in previous sections.

It is know that thermally evaporated ZnS films are rough [55]. For our chip that would create additional stray light and may increase background signal a little. But ZnS layer adds more than 15-20% increase in coupling efficiency which should compensate for it.

For spectral characterization, collimated white light was normally incident upon gratings and zero order transmission was measured. Figure 3.25 (a),(b) and (c) shows measurement for 340nm gratings, on three different chips (id 3, 4, 5). There is variation of transmission dip among different chips. On the same chip, there is slight variation between two 340nm gratings. Same graphs also contain simulated T_0 curves for each grating. An extensive set of simulations were performed in order to match the experimental data. Simulation parameters are noted in each of the graph. It was found out that sidewall thickness parameter (WallT) is most influential factor for matching.

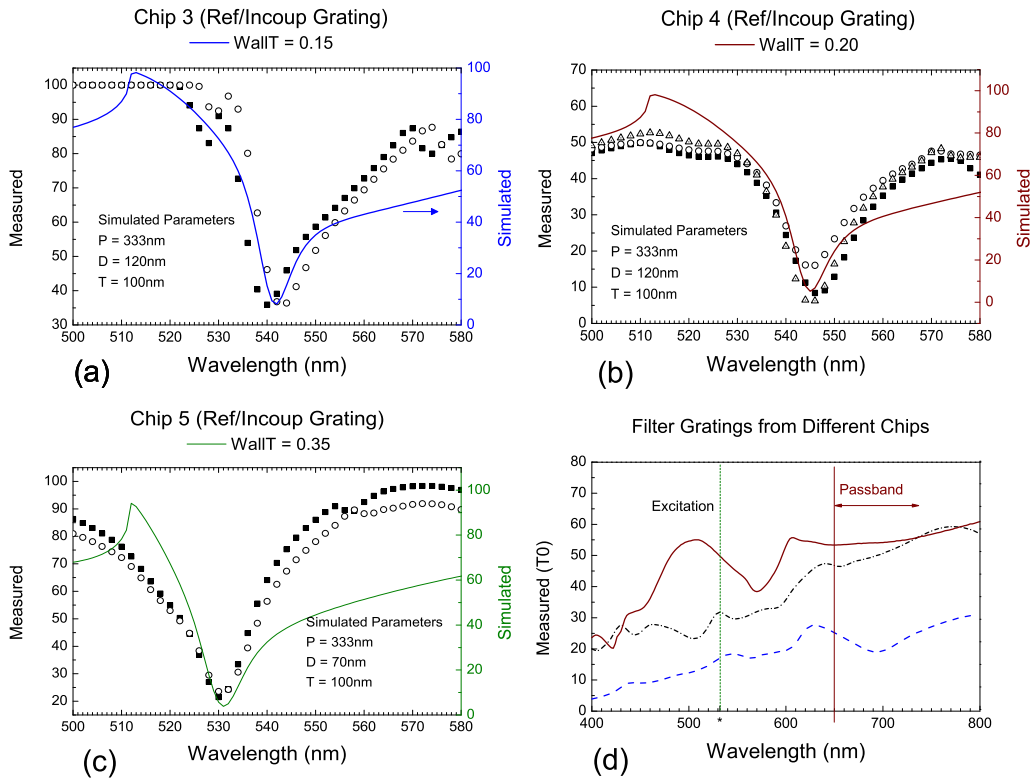


Figure 3.25: Matching of measured and simulated T_0 data. - (a),(b),(c) T_0 measured(symbols) and simulated(lines) for 340nm gratings. (■) grating in the center, (○) grating on side. (d) Filter grating measured data only

It was not possible to fit filter grating data with the range of parameters that were tried out. Additionally, as seen from figure 3.25 (d), three filters on different chips did not show similar characteristics. They did not indicate strong blocking of 532nm compared with pass-band as it was designed.

Figure 3.26 shows microfluidics characterization done by profilometer and optical microscope. Most chips showed similar profiles and were clean. A small upward convex shape of the channel could be result of early de-molding but that can be taken care of in the future. Channel edge quality was within acceptable tolerances.

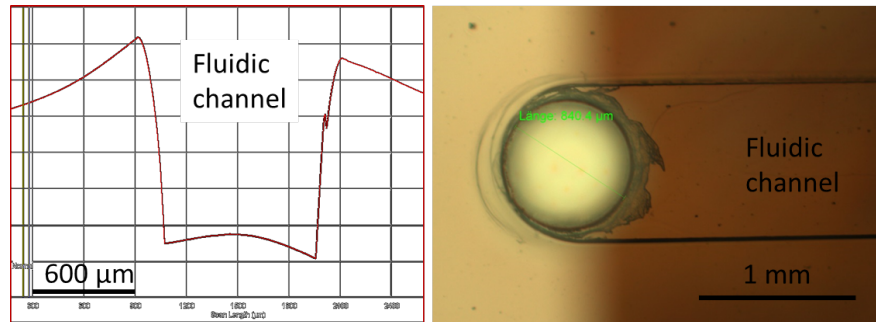


Figure 3.26: Characterization of embossed fluidics. - Left plot shows profilometer scan across fluidics channel. Right image shows optical microscope of half channel with drilled hole for steel tubing.

3.7.1 Selection of filters

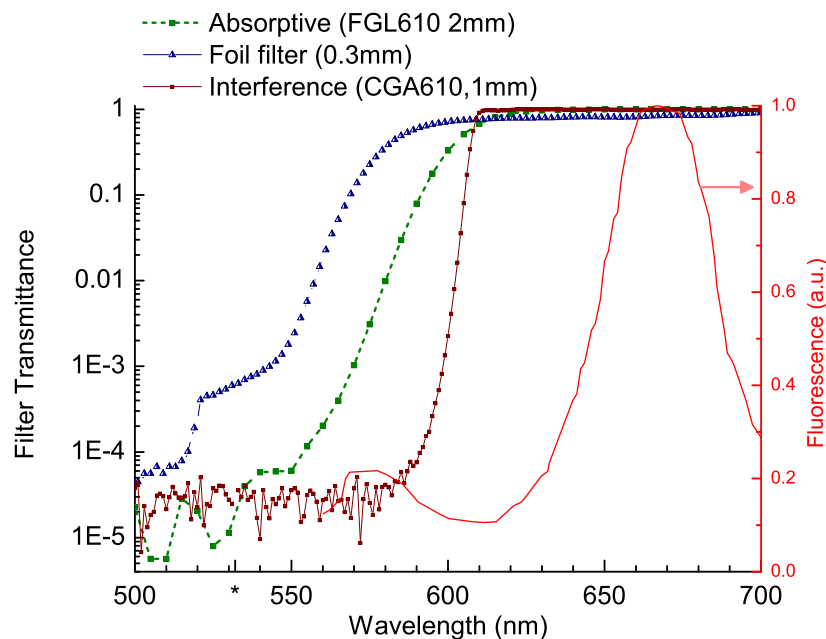


Figure 3.27: Comparison of longpass filters of type: interference (Newport), thick glass (Thorlabs) and thin foil(Lee Filters) color filters. - Show measured transmission data for three filters. Red curve is emission of Surelight P1 for reference.

Use of crossed polarizers would be an ideal filtering choice for laser. However a 2° misalignment between polarizers causes 3-fold increase in light leakage[56]. Therefore it is not a viable option to be used in platform. Proper selection of long-pass filter is difficult choice. Attenuation in stop band of long-pass filter must be plotted with semi-log scale as shown in figure 3.27 to get a clear idea.

Filter characteristics are angle dependent. Therefore we created a simple experiment to test these filters in a realistic scenario. A laser beam was diffused by using scotch tape

and allowed to fall on an optical power meter (Newport 1805C). Power was recorded with and without the filter. Figure 3.28 shows the clean and scattered laser spot by scotch tape and also schematic of the test.

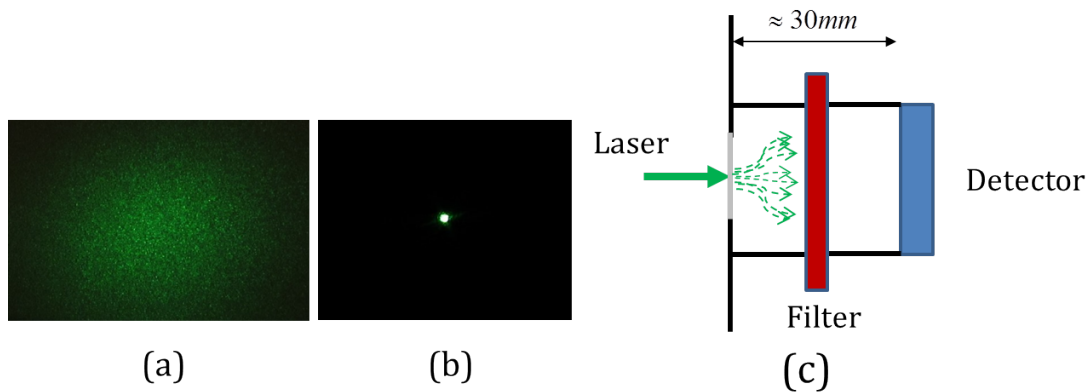


Figure 3.28: Realistic filter testing - (a) Laser scattered by scotch tape incident on white curtain. (b) Clean laser spot (c) Schematic of test arrangement. Optical path is well shielded.

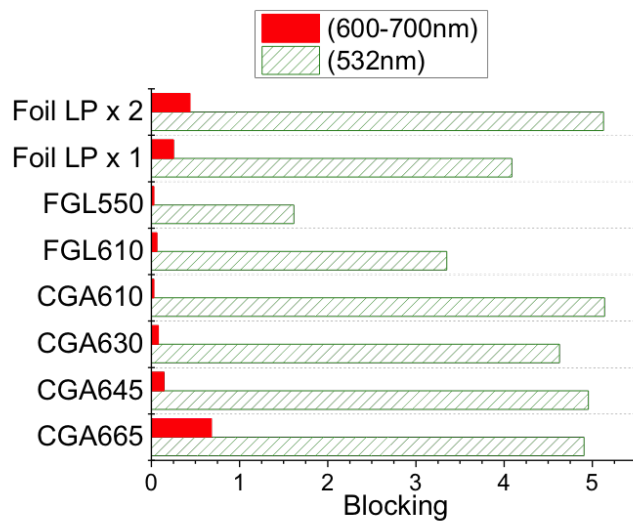


Figure 3.29: Laser excitation and pass-band blocking of long-pass filters. - CGA are interference filters from Newport (1mm thick). FGL are colored glass filters from Thorlabs (2mm thick). Foil LP are thin color filters from Lee (0.3 mm thick). Values are attenuation in optical transmission.

The test was carried out for 7 different filters and the results obtained as optical transmission values are in table ???. Fluorophore emission was simulated with a 3mm LED with similar spectra and similar test was performed. Red attenuation values are listed rather than transmission for easier interpretation. From these measurements, the best filter would be CGA610 or second choice be foil filters. Though they have 25% reduction in signal, they are extremely thin, cheap and very effectively block the laser. This is very important for lowering the baseline signal and also improving overall sensitivity.

3.8 Biosensing Experiments

3.8.1 Experiment-01 Dose-response

The microfluidic sensing region is coated with perfluorophenylazides (PFPA) linked dextran hydrogel using similar process described in paper [57]. Primary antibodies (rabbit IgG) are attached to the hydrogel. (Surface functionalization on these chips was performed in collaboration with Landquart center of CSEM SA). Secondary antibodies (anti-rabbit IgG) labeled with Surelight P1 fluorescent marker in PBS (pH=7.2) is used as analyte. The excitation source is a 532 nm DPSS laser diode (Thorlabs DJ532-

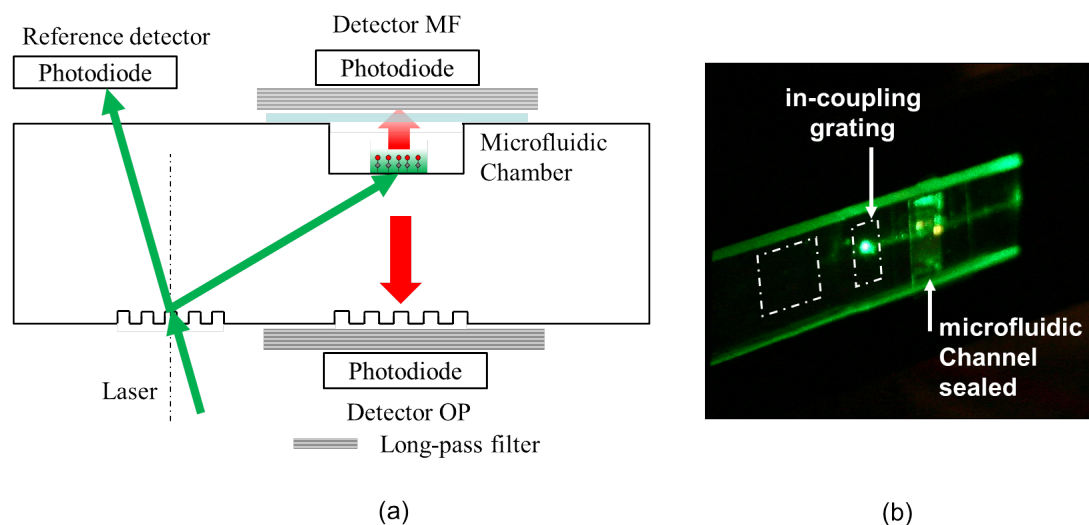


Figure 3.30: Experiment schematic and photo of illuminated chip. -

10) mounted in a thermoelectrically cooled mount and a constant current laser diode controller. The emission from laser diode is collimated (divergence = 12 mrad) and is unpolarized. The chip is fixed into a custom designed holder. The holder has windows on the one side to allow laser input, fixing of detectors and entry for microfluidic tubes. The holder is fixed on the X-Y translation stage which is mounted on a rotation platform. This freedom of motion allows adjusting the incident angle and the position of the TIR spots exactly under the microfluidics. The detectors are Si-photodiodes (S2387 series, Hamamatsu) which are fixed with long-pass interference filters (CGA610, Newport). The filters are laser cut to match the size of the photodiodes. The photodiode output is amplified by an op-amp transimpedance amplifier. The gain of the amplifier can be adjusted from 10^5 to 10^7 V/A.

Laser current set to 150mA gave $P_{OUT}=1.2$ mW optical power at the input of the grating. The angle of incidence on the grating is $4 \pm 0.5^\circ$ which leads to diffracted angle into waveguide $\approx 76.7^\circ$. Spot-size of the beam before incident upon the grating is $900\mu\text{m}$ and underneath the fluidic channel is 1.09mm (using equation 3.12).

The chip is connected to a peristaltic pump (Ismatec IPC-N) which allows maintaining laminar flow into the channel. The flow rate used during the complete experiment is $20 \mu\text{L}/\text{min}$. Initially we passed $800 \mu\text{L}$ of PBS through the chip to rehydrate the hydrogel and measured the baseline signal. After that we injected six different concentrations of the analyte 1, 5, 10, 25, 50, 100, $250\mu\text{g}/\text{mL}$. Each concentration was dosed with $350 \mu\text{L}$ solution. After each dose was completed a washing step was carried out

with 400 L of PBS. Figure 3.31 (a) shows the real time response obtained during this experiment.

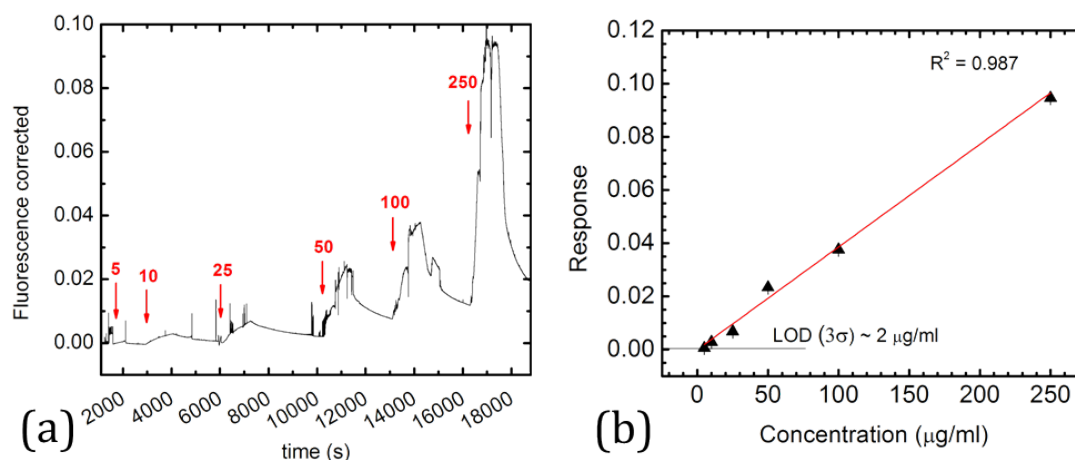


Figure 3.31: Immunoassay experiment data. - (a) Data from the whole experiment. (b) Extracted response from the plateau of each dose. $1 \mu\text{g/ml}$ is not shown as it is same as baseline.

Data extracted from plateau of each dose is plotted in figure 3.31 (b). The limit of detection calculated is $\approx 2 \mu\text{g/ml}$ (132 pM, M_w of IgG+P1 is $15.15 \times 10^6 \text{Da}$).

Scope for Improvement

1. Final spot-size was slightly larger (1.06mm) than width of fluidic region (1mm). Therefore laser beam was scattered by the edges. ► This could be solved by making the spot smaller and/or increasing fluidic width.
2. Diffracted angle in the waveguide was 76.7° which means penetration depth of $\approx 110 \text{nm}$. ► We could reduce diffracted angle to increase the penetration depth and as a result fluorescence signal
3. As soon as we start washing step, the response falls rapidly. This could mean ineffective binding of antibodies to the surface and we are measuring bulk fluorescence. ► This was tested by fluorescence microscopy and results are presented in the next section.
5. Excitation was on during entire time of experiment (about 4 hours) could have photo-bleached the fluorophores. ► Timed shutter or pulsed excitation fluorophores may remain stable for longer time.

3.8.2 Experiment-02 Fluorescence Microscopy

The process with PFPA based surface chemistry was not fully established. Therefore to find out about its quality on BioCOP chips we made a controlled study. Set of 8 chips was divided into groups of 2 (a),(b), (c) and (d). Each chip surface was cross-linked with PFPA and carboxy-dextran hydrogel was attached. (a) and (b) surfaces were loaded with primary antibodies to act as capture mechanism while (c) and (d) were without. (a) and (c) surfaces were blocked with Ethanolamine and (b) and (d) were blocked with additionally 0.2% BSA. Then secondary antibodies with fluorophores were flown in the channel (concentration= $250 \mu\text{g/ml}$) just like real biotest and later washed

with PBS for at least 20 minutes. Then the fluorescence microscopy was performed on the chips and the images of one chip from each set is shown in figure 3.32.

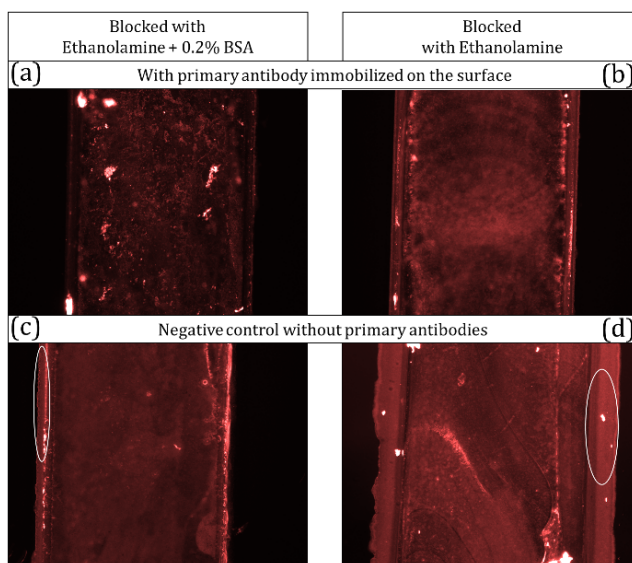


Figure 3.32: Fluorescence microscope images inside the fluidic channel. - (a),(b) Surfaces with primary antibodies blocked (c,d) No antibodies on surface only hydrogel attached via PFPA linker. All surfaces are blocked by Ethanolamine only or additionally with Bovine Serum Albumin(BSA). Area marked with white ellipses show fluorescence outside fluidic area only in (c),(d) due to leakage under sealing tape.

We measured mean gray level at the center of channel, in all images. Chips blocked with ETA + BSA showed lowest mean levels while chips blocked only with ETA showed highest. Chips with or without primary antibodies did not show much difference. This could be result of high amount of non-specific binding. All chips show very non-uniform distribution of fluorescence and also show large clusters of antibodies seen as bright red/white spots. However under such conditions we should have seen larger signal during previous experiment which we did not. Surface chemist at CSEM Landquart pointed out that $250\mu\text{g}/\text{ml}$ is very high concentration and it might have affected the results. This corresponds to the experiment where we measured a massive signal for this concentration but it dropped quickly after washing step. Due to time constraints at this point, (in the frame of my thesis work) it was decided not to work on surface chemistry and look for an alternative.

The search lead to Arrayon Biotechnology SA (Neuchâtel, Switzerland), a start-up from CSEM SA. Chips for next experiments are treated with Arrayon's chemistry - OptoDex®.

3.8.3 Experiment-03 Dose Response

Many improvements were made before next dose response test. A mechanical shutter based on a hobby servo motor was introduced into optical path between laser beam and grating. It was controlled by an Arduino board (www.arduino.cc). The board was commanded to open/close the shutter by main acquisition program. To reduce scattered green light, beam was focused and re-collimated into a line-shape by using two plano-convex cylindrical lenses ($f = 50\text{mm}$ and $f = 5\text{mm}$) as illustrated in figure

3.7 (b). Inside sensing setup many light absorbing black papers were placed to absorb scattered laser. Sensing area is functionalized with OptoDex® and primary antibodies (mouse IgG) are attached to layer in dry state by photo activation [58, 59, 60]. OptoDex binds primary antibodies and then blocks any further non-specific binding. The quality of functionalization was verified by Arrayon independently as part of service. During test, incident angle on grating was $\alpha = -6^\circ$ which results in diffracted angle $\theta_{in} = 76.4^\circ$ and penetration depth $\approx 125\text{nm}$. No $T-1$ order exists and therefore T_0 beam was used for reference with a pinhole and neutral density filter to reduce incident power on reference photodiode.

Initially PBS was flown for more than 30 mins to hydrolyze the surface. Then doses were injected ($387\mu\text{l}$) as follows : 0.985, 4.85, 8.32, 15.32 and 29.12 $\mu\text{g/ml}$. Real time response obtained is shown in the figure 3.33 (a) and dose response extracted from plateau of each dose is shown in figure 3.33 (b). The red fit is done with logistic model and LOD calculated from graph is $\approx 0.1\mu\text{g/ml}$ (6.6 pM) which is an excellent result.

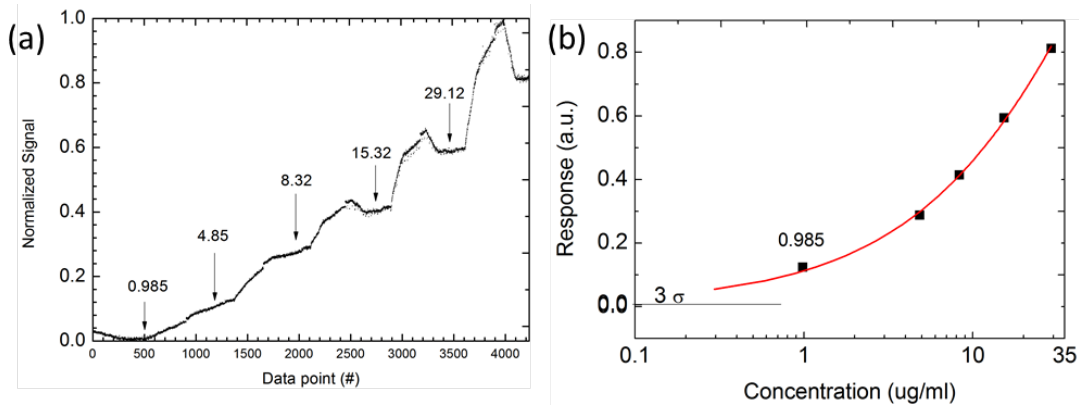


Figure 3.33: Dose-response test data - (a) Doses applied starting from 0.985, 4.85, 8.32, 15.32 and 29.12 $\mu\text{g/ml}$. Arrow indicates when dose was injected. (b) Extracted data , lowest measured dose is marked for reference.

Starting from lowest concentration response was increasing steadily. For lower two concentrations until signal did not decrease during PBS washing step. Which might suggest proper binding of secondary antibodies. As concentration increased signal also increased however we start seeing the PBS washing effect resulting in decrease of signal and then plateau.

3.8.4 Experiment-04 Dose-response

After promising result obtained from previous experiment we decided to repeat it starting from concentration of 50ng/ml . However we decided to increase penetration depth to try if that increases fluorescence signal gain without increasing the background signal. The incident angle on the grating was set to -15° which gives diffracted angle of close to 60.6° (Grating period 333nm assumed. Gratings on chips were characterized by this time during the work). This leads to penetration depth of $\approx 400 - 450\text{nm}$. Now the tricky part is that if the diffracted angle is less than 60.3° then light at fluidic surface would not undergo TIR, instead it will transmit through falling directly on the detector on front side. This will lead to huge increase in background signal.

For this experiment the doses were: 50, 100, 200, 400, 800, 1000, 5000 ng/ml. The response recorded and data extracted from response curve are shown in 3.34 (a) and (b) respectively.

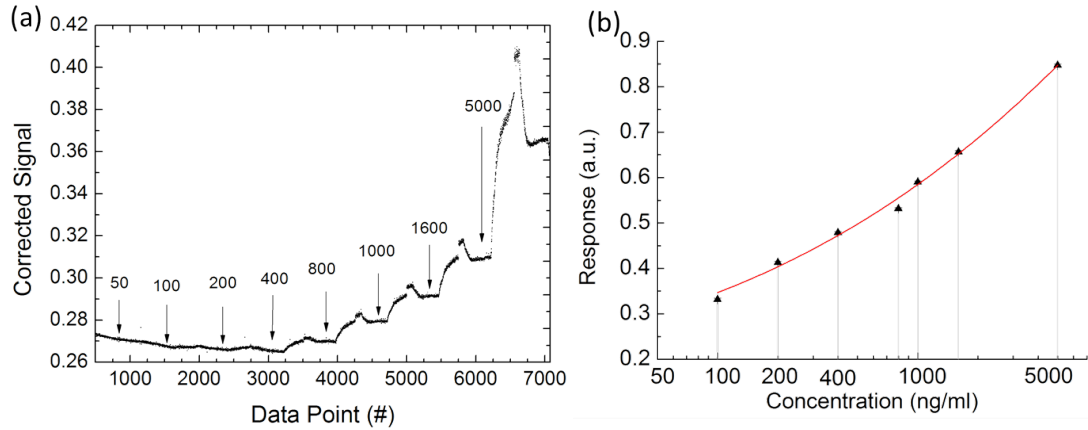


Figure 3.34: Dose-response test data. - (a) Real time response for doses: 50, 100, 200, 400, 800, 1000, 5000 ng/ml. (b) Extracted data. 50ng/ml was same as baseline.

The background signal did not increase as it would have if diffracted angle was smaller than critical angle. So we could assume that penetration depth was indeed close to what was planned. Furthermore the detection limit found in previous experiment correlates with the lowest concentration that was measured - 100 ng/ml (6.6 pM).

3.9 Final Updated Design

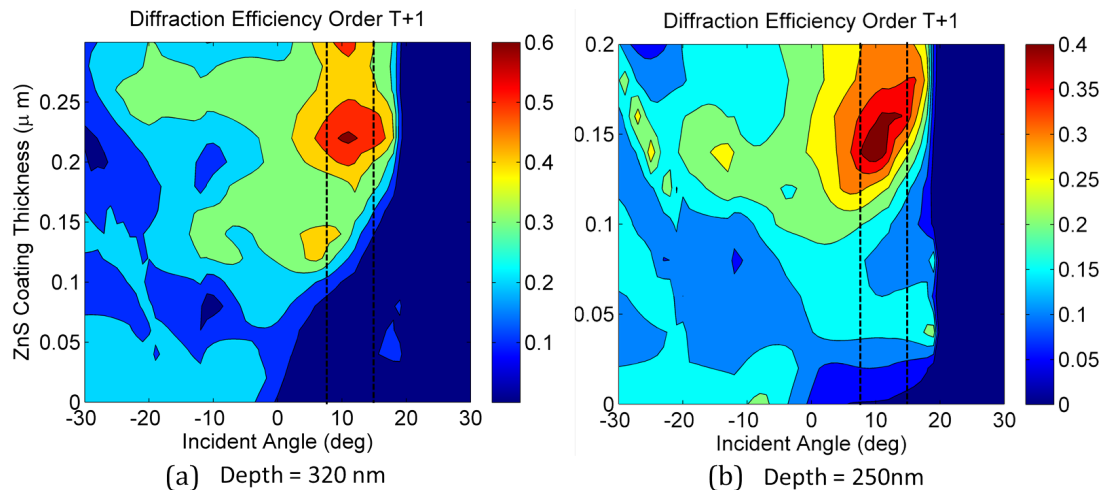


Figure 3.35: Diffraction efficiency map for T_{+1} order - Grating parameters are $\Lambda = 440\text{nm}$. (a) depth=320nm. (b) depth=250nm. Variation of incident angle and ZnS thickness. Regions suitable for sensor chip are marked by lines dashed lines.

As discussed in section 3.7, filter grating was not working as per the design, hence its removal was necessary. It was not possible to modify master substrate therefore from in-house library of shims, period = 440nm, depth=320nm grating was chosen. Figure 3.35 (a) shows the diffraction efficiency map for this exact grating as a function

of incident angle and ZnS thickness. Simulations show results for both 250nm and 320 nm depth. They show similar pattern with peak efficiency at 10° incident angle and ZnS thickness \approx 0.6-0.7 times depth (200nm and 150nm respectively).

We had designed very little flexibility for microfluidic chamber width. Width is increased from 1mm to 4mm.

Tests with newly designed chips are undergoing and their results should be available soon. Preliminary experiment carried out with single dose of 50 μ g/ml and using a chip without ZnS coating showed \approx 6 times signal gain over the baseline.

3.10 Conclusions

Starting from idea to step-by-step design of BioCOP platform was completed. The formulation developed is highly versatile for making any changes in a very systematic way. It takes into account complete optical path from laser diode to sensing surface inside fluidic chamber.

We also found the effect of sidewall formations during ZnS overcoating. To correct for this phenomenon we introduced an adjustment parameter in the simulation of gratings. Based on design specification obtained we designed a set of highly efficient (50% for unpolarized light) in-coupling gratings for $\lambda = 532nm$ into a COC substrate (3mm thick), for appropriate in-coupling angle into the substrate supporting TIR guiding. We also designed an integrated filter on the chip based on grating for blocking laser at incidence angles near normal incidence. The complete design and simulation formulation is available in the form of highly extensible Matlab code.

Based on the designed parameters chips were fabricated by simultaneous hot embossing of sub-wavelength gratings ($\Lambda = 340nm$, depth = 200nm) and high depth fluidic structure (depth=100 μ m). The characterization of the chips was carried out using AFM, transmittance measurement and optical microscopy. The gratings fabricated on the chip measured final depth being \approx 50% less than designed. This resulted in reduced in-coupling efficiency.

Nevertheless, three full scale dose-response tests were carried out. From first experiment many problems were identified and solutions were developed. Second and third experiment saw a drastic improvement finally achieving limit of detection of 100ng/ml (6.6 pM). The LOD estimated from second dose-response curve was in fact confirmed by the last experiment.

The baseline levels of all experiments are higher than expected (should be close to zero). With 1e-5 optical attenuation filter, how does the light escape and goes into the detector? The answer is two fold. Due to reduced grating efficiency ratio of stray light to designed order is higher. Furthermore laser beam continues to bounce from walls chip contributing to excessive parasitic reflections. Therefore further work needs to be done for reducing baseline to minimum. This can be achieved by increasing diffraction efficiency for only one diffracted mode. By carefully tuning the length of the chip beam can be recycled to bounce multiple times at the sensing area increasing the excitation power. Signal gain can be improved by extracting Supercritical Angle Fluorescence (SAF). Integration of the schemes demonstrated by [61] and [10].

Summary of three experiments is shown below in table 3.10.

This work on BioCOP platform has provided:

- Integration of optimized components into a monolithic sensor chip

Table 3.10: Dose-response tests summary

Exp. #	Surface	Pen. Depth nm	Low/High Dose $\mu\text{g/ml}$	LOD Det. $\mu\text{g/ml}$	LOD Est. $\mu\text{g/ml}$
1	PFPA-hydrogel	110	1 to 250	5	2
2	OptoDex	125	0.985 to 29.12	0.985	0.1
3	OptoDex	400-450	0.05 to 5	0.1	0.1

- Proof-of-concept experiments indicate LoD of 100ng/ml for IgG assay
- Optimized first order diffraction gratings for design wavelength of 532nm
- Zero-order blocking filter for 532nm with pass-band above 666nm.
- Complete functional system for further testing
- Enhanced capability for combining evanescent field with signal enhancement effects

Photo-FET

To date, Lab-on-a-Chip type devices with integrated fluidics are not available for true Point-of-Care (PoC) applications, specifically directly to patients. (with exception of blood glucose meters based upon resistance changes due to glucose-oxidase reaction[62]). Although the chips themselves are cheap and small, they must generally be used in conjunction with bulky optical light-sources and detectors. The lack of an integrated, versatile detection scheme is a major obstacle to the deployment to PoC device.

Organic photonic devices have inherent advantages over their inorganic counterparts[63]. Worthy mentioning are low cost fabrication on plastic substrates with very high throughput and chemically tunable to desired characteristics. Viability of using organic light emitting diodes (OLED) and organic photodiodes (OPD) into biosensing applications together or separately have been demonstrated by numerous groups[64, 65, 66].

Organic field effect transistors for light generation and detection are relatively newcomers in the field of optoelectronic devices. In this chapter we evaluate current state-of-the-art organic photonic devices applied to a PoC sensing platform. This work was part of an EU project Photo-FET (acronym for Photonic Field Effect Transistors). The consortium involved in total six partners working towards developing an integrated organic photonic platform for detection of cardiovascular health markers in PoC setting. Partner Molecular Vision (MV) Ltd. (<http://www.molecularvision.co.uk>) is a diagnostics start-up (now acquired by Abingdon Health group, UK) who has developed a product based upon OLED and OPD devices[67, 68, 69, 70, 71]. Other partners included CNR Bologna (<http://www.bo.ismnr.it>) for making light emitting transistors and later light sensing transistors; Saes Getters (<http://www.saesgetters.com/>) for encapsulation related technologies; Polytechnic Milan POLIMI (<http://cnst.iit.it>) for integrated passive optics and Imperial College London (<http://www3.imperial.ac.uk/plasticelectronics>) for developing light sensing transistors and low-autofluorescence foil filters.

We had responsibility of integrating all these individual components and technology into a single packaged platform. We also collaborated with Saes Getters to develop an automated encapsulation tool inside a glove-box for organic devices which is now functional at CSEM SA. CSEM also worked together with MV to design and manufacture 3-channel passive microfluidics chip used during the project. More information on Photo-FET could be found from reports submitted to EU commission or on project website (<http://www.bo.ismnr.it/photofet/>).

I will keep the chapter content limited only to describe my contributions to integrate hybrid and state-of-the art technologies into a real world sensing platform.

4.1 Introduction

The platform is based upon trans-illuminated fluorescence excitation and detection as illustrated in figure 4.1. A light emitting (LE-FET) and light sensing (LS-FET) field effect transistors are fixed on two side of a plastic microfluidic chip. They are positioned in such a way that light generation region of LE-FET and light detection region of LS-FET are directly facing each other through open slit or a window. The open slit or window is the reaction chamber of the assay. The fluidic window is sealed from both sides with a transparent tape. A long-pass filter is placed before LS-FET and similarly a short-pas filter is placed after LE-FET. The analyte flows across the microfluidic channel in between this stack. When light from LE-FET passes through the channel it excites fluorescence which is then detected by the LS-FET on the other side. The analyte could be flowing through the channel or immobilized on the sealing film. The filter stack is optimized to block unwanted part of the spectrum of LE-FET and only allow to pass as much as possible only fluorescent emission. The light source could also be an OLED or an inorganic LED. Similarly the detection could be made with an OPD or a Si photodiode, if required.

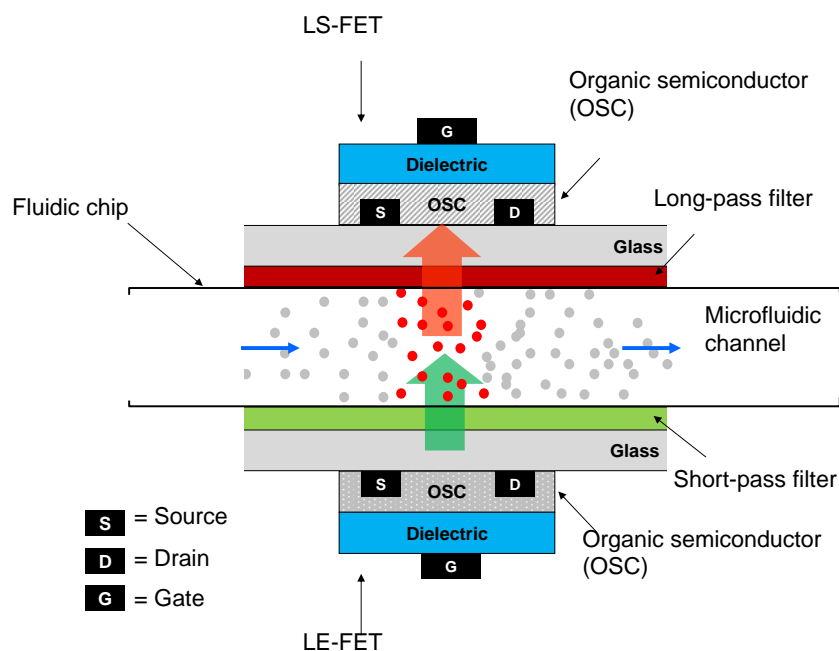


Figure 4.1: Working principle and architecture of Photo-FET platform. - Microfluidic reaction chamber with a transparent window is sandwiched between LE-FET and LS-FET. Fluorescent analyte flowing through or immobilized inside the chamber is excited by LE-FET emission and generated fluorescence is detected by LS-FET. Spatial filtering with short-pass filter after LE-FET and long-pass filter before LS-FET is included.

4.2 Device physics

Critical aspects for a light emitting FET are; efficient electron and hole injection from metal electrodes, active semiconductor materials sustain ambipolar field-effect transport and efficient electro-luminescence emission, and trap-free dielectric surfaces to support effective mobility of both electrons and holes at the dielectric/active material interface.

Fundamental difference between a vertical geometry OLED and planar device such as LE-FET is that charge transport occurs in the plane of device at dielectric/organic interface[72]. In next two sections I will explain device physics of LE-FET and LS-FET.

4.2.1 LE-FET

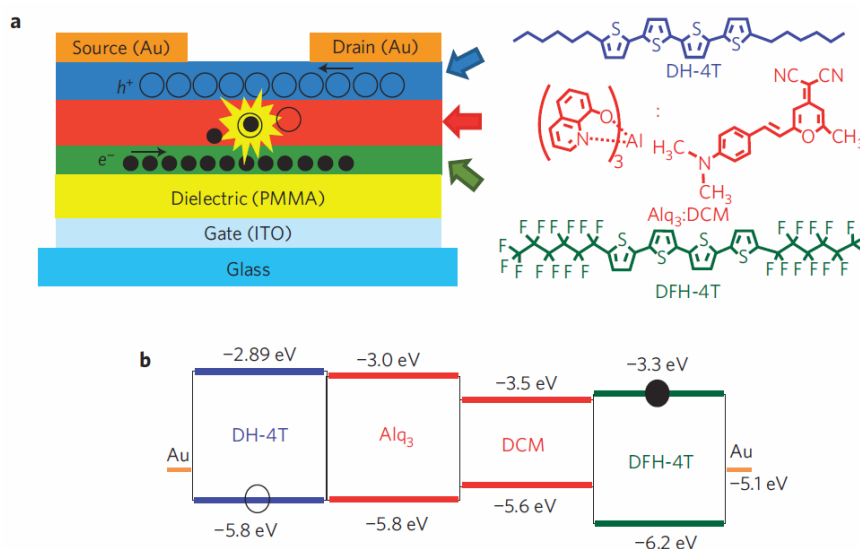


Figure 4.2: LE-FET device physics adopted from Ref [73]. - (a) Schematic of tri-layer LE-FET with each organic layer molecule shown on the side (b) Energy level diagram of tri-layer indicating HOMO and LUMO levels of organic molecule with Fermi level of gold contacts.

There are few different architectures of LE-FET that can be fabricated such as single layer unipolar, horizontal p-n heterojunction, bilayer whose external quantum efficiency (EQE) is not reported more than 0.5-0.6%. Because they suffer from exciton quenching and photon losses as light emission region is close to metal electrode. In Photo-FET we used tri-layer heterostructure LE-FET which demonstrates EQE=5% which is two times higher than OLEDs (2.2%) based on same materials [73]. The device architecture, organic layers and energy level diagram of such a device is shown in figure 4.2.

FET is fabricated on glass substrate with 150nm ITO (Indium Tin Oxide) and 450nm PMMA ($\epsilon = 2.6$) acting as gate contact and dielectric respectively. The active region is made of three organic layers. First and third layer (green and blue) are field-effect electron transporting (n-type, 7nm) and hole transporting (p-type, 15nm) semiconductors. The middle layer (red) is light emitting host-guest matrix (40nm). On top of device 50nm gold contacts are evaporated through shadow mask to make source and drain contacts. As seen in figure 4.2 (b), lowest unoccupied molecular orbital

(LUMO) of n-type material is higher than LUMO of guest matrix (-3.3eV vs -3.5eV) while highest occupied molecular orbital (HOMO) of p-type is lower than guest (-5.8eV vs -5.6eV). This allows electrons jumping down from n-type to host(DCM) and holes jumping up from p-type to host(DCM) via guest(Alq3). The sublimation process is optimized to form interface morphology of continuous multi-stack. An ambipolar FET fabricated without host-guest matrix showed balanced mobility of $0.01\text{cm}^2/\text{Vs}$ with no light emission. When the device is operated within unipolar regime ($|V_{DS}| = |$

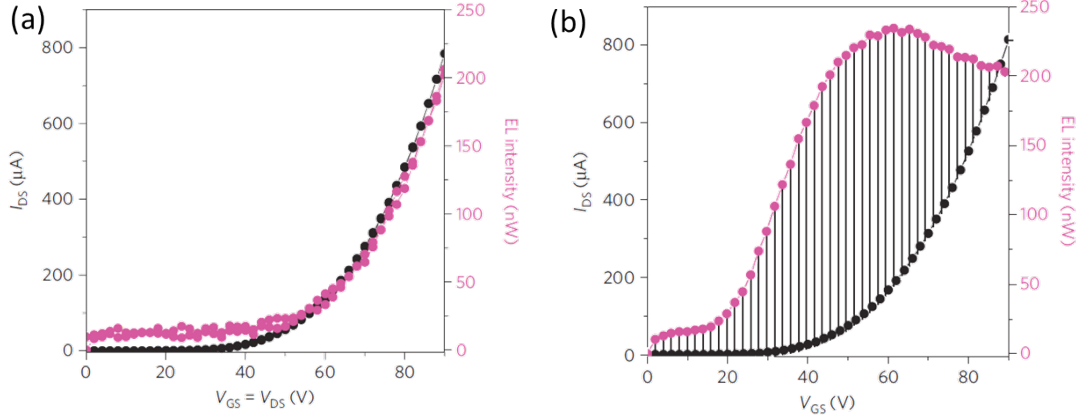


Figure 4.3: Electroluminescence and charge density correlation of LE-FET adopted from Ref. [73] - (a) Unipolar regime linear correlation $|V_{DS}| = |V_{GS}|$ (b) ambipolar regime $|V_{GS}| < |V_{DS}|$, $V_{DS} = 90\text{V}$

$V_{GS}|$) a diode-like light emission occurs characterized by linear correlation between electroluminescence and current density as seen in figure 4.3 (a). When biasing is adjusted to allow simultaneous charge injection from source and drain ($|V_{GS}| < |V_{DS}|$) then a new mechanism of electroluminescence is observed as seen in figure 4.3 (b) produced by an ambipolar current.

Under ambipolar regime, light-generation takes place far from electrodes thereby preventing photon losses and exciton quenching. Electrons and holes percolate from transporting layers to middle guest-host layer where excitons are formed. LE-FET light out-coupling efficiency is $\sim 27\%$ which is higher than a typical OLED $\sim 20\%$.

4.2.2 LS-FET

Organic field effect transistors (OFET) are studied extensively and demonstrated for backplane switching[74], RFID tag[75], sensing applications[76]. Light sensing OFETs (LS-FET) were reported by ref [77, 78, 79] opening up new opportunities. LS-FET can be fabricated with different architectures but we will focus on top-gate architecture which was used during Photo-FET shown in figure 4.4 (a). Gold contacts are evaporated on glass substrate to act as source and drain terminals. A blend of P3HT (Poly(3-hexylthiophene-2,5-diyl)) and PCBM([6,6]-Phenyl C71 butyric acid methyl ester) in chloroform/chlorobenzene is spin coated. This forms a heterojunction semiconductor forming domains of p-n junctions inside the thin film. After annealing to remove the solvent substrate is spin coated with 300-500 nm fluorinated dielectric Cytop®($\epsilon = 2.1$). After annealing dielectric film, gate contact of aluminium (50-80nm) is evaporated on the top.

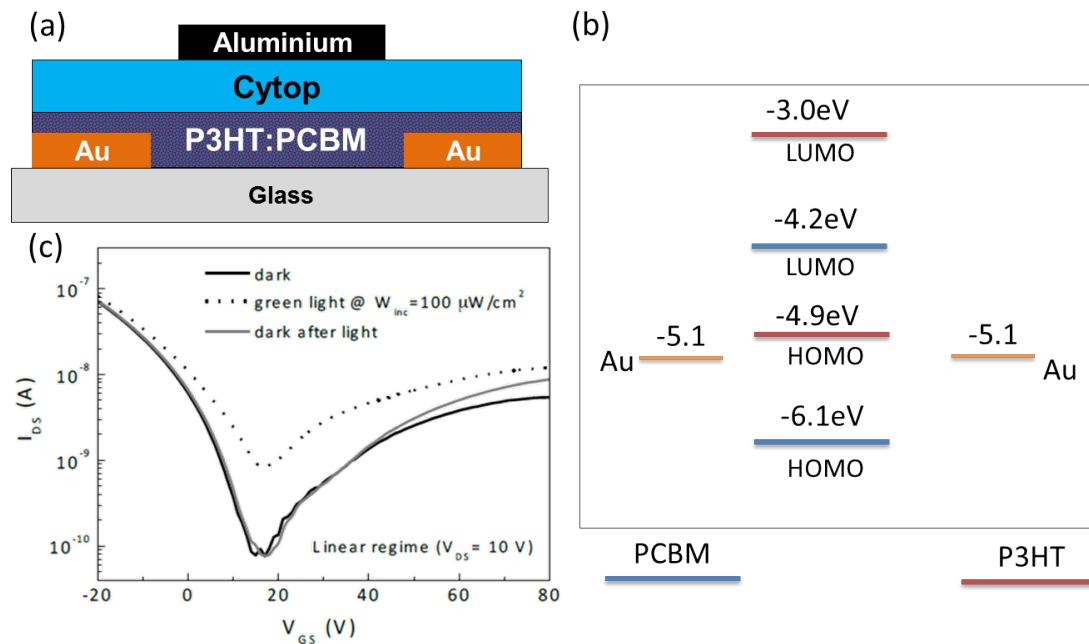


Figure 4.4: Working principle of Light sensing field effect transistor (LS-FET) - (a) Top gate architecture (b) Energy level diagram (c) Current voltage characteristics in dark and with green light, $100 \mu W/cm^2$

Figure 4.4 (c) shows current-voltage (I-V) characteristics of LS-FET at $V_{DS} = 10$ V and $V_{GS} = -20$ to $+80$ V, in dark (continuous lines) and under illumination of green light at $100 \mu W/cm^2$ optical power. The ambipolar V-shape in I-V characteristics is clearly visible. Photocurrent gain of 10 is achieved with no change in dark current level before and after illumination.

4.3 Design

4.3.1 Mask Layouts

ITO contacts for all devices are deposited and pre-patterned on the glass substrate. For LE-FETs all organic layers are deposited by thermal sublimation and therefore a shadow mask is needed for selective area evaporation of organic layers. Semiconductor layer and gate dielectric for LS-FET are solution processed by spin coating. For source/drain metallic contacts on LE-FET and Aluminium gate contact for LS-FET, another shadow mask is required.

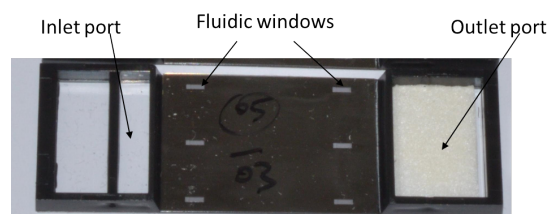


Figure 4.5: Photo-FET Fluidic Chip - Made in black polystyrene by injection molding. Fluidic channels are on backside of the chip.

Three channel microfluidic chip has six reaction chamber windows each $1 \times 3 \text{ mm}^2$ in size, three rows and two columns format as shown in figure 4.5. Therefore all devices needed to be in the same 3x2 format following exact dimensions. The size of each

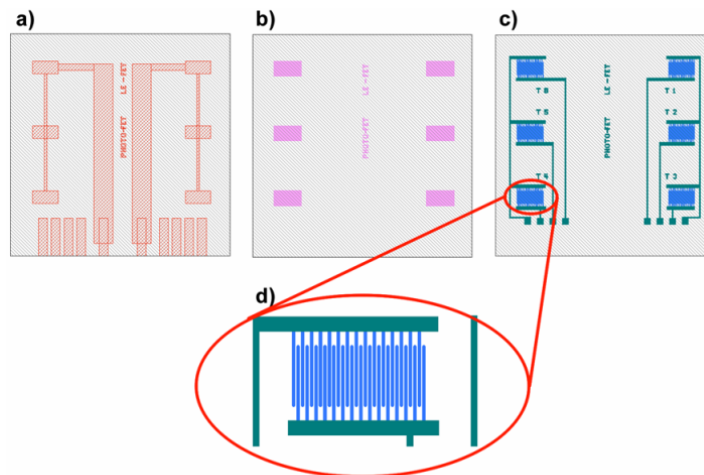


Figure 4.6: LE-FET mask layouts - (a) Mask for gate contact of ITO (b) Organic layers mask (c) Source drain contacts gold evaporation mask.

individual device was modeled and calculated. These devices needed to be well encapsulated to protect from degradation. The specifications for encapsulation process were acquired from Saes Getters. Optimal dimensions for substrate size, encapsulation glass and glue size, alignment margins were taken into account and the mask were designed in collaboration with partners involved in fabrication of LE-FET and LS-FET. Figure 4.6 shows the mask layouts designed for LE-FET. Figure 4.7(a) shows how encapsulation glass is positioned on the top (shadow area) and electrical contacts from source and drain (green lines) are brought outside of encapsulation connecting to ITO pads on the bottom edge of the substrate. Figure 4.7(b) shows how encapsulation constraints are taken into account when designing the mask. Many of these specifications were placed inside a scripting language in the mask design software CleWin allowing quick changes of parameters without laborious work.

From this point onwards we will assume that LE-FET and LS-FET devices were fabricated as per above designs. Now we will focus mainly on integration of these devices in a sensing platform.

4.4 Problem of contacting ITO Pads

All electrical contacts to both types of devices are finally connected to ten ITO pads on one edge of the substrate. Each one is 3-terminal devices which totals to 18 terminals - 2 contacts for common source (6), 2 contacts for common gate(6) and 6 individual drain contacts (6). Since the LE-FET and LS-FET need to be mounted back-to-back the most sensible way for interfacing was to fabricate a custom holder consisting of two halves that are screwed together, once all the components are placed. Figure 4.8 (left) shows the cross-section of the holder. The electrical interconnects between the ITO lines of the LE-FET or LS-FET and the PCB (green) for the connection to external measuring equipment are provided by gold Zebra connector (orange). And figure 4.8 (right) shows

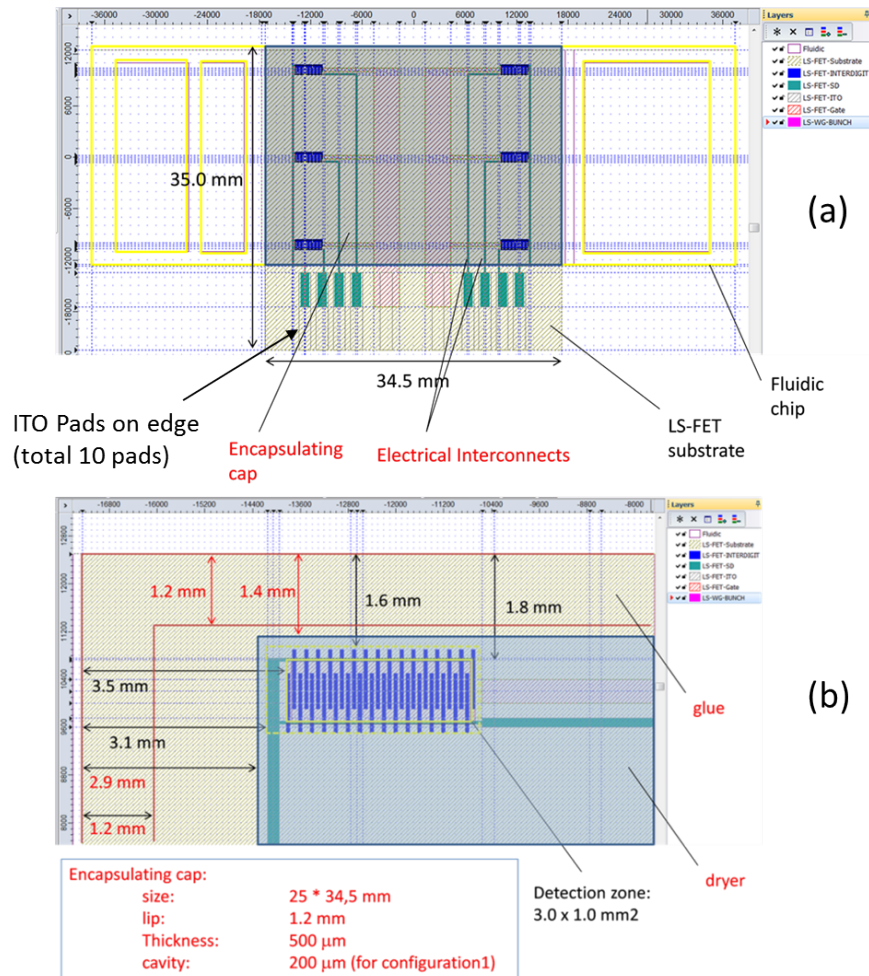


Figure 4.7: (a)LE-FET mask overlapped in mask design software - Shows top-view of encapsulation geometry shown for the case of LS-FET along with mask layout(b)Shows close-in of the encapsulation strategy for a single detection zone, part of the glue frame and the dryer (getter). Similar strategy was adopted for LE-FET design.

the 3D-CAD assembly of the same. Reliably contacting ITO pads separated only by 1mm or is not possible by any other method. The zebra connector technique is used in LCD monitors to contact screen glass with driver backplane.

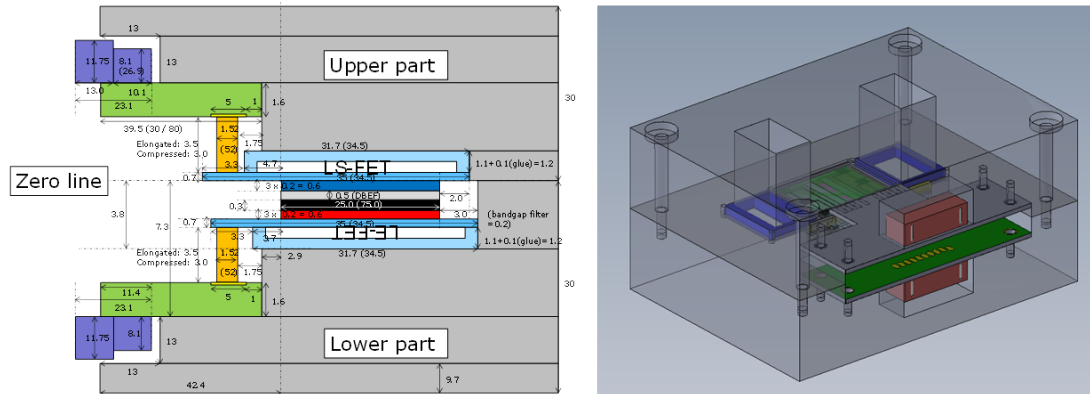


Figure 4.8: - (left) Cross-section of Gen 1 holder for testing LE-FET and LS-FET(right) 3D assembly of the whole stack

Figure 4.9 shows how devices are assembled into the holder. LS-FET is fixed in the (a) in contact with zebra connectors and then fluidics chip is inserted. That is why LS-FET is not visible in (a). LE-FET is fixed in (b). During measurements two halves are placed on top of each other tightly holding two devices with well aligned emission and detection regions of each pixel.

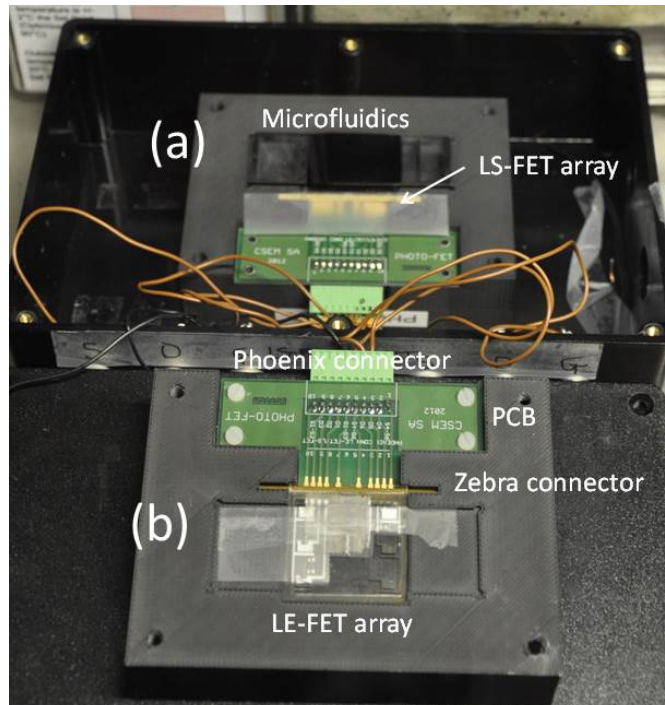


Figure 4.9: - PCB that establishes the contact between electronics and FET arrays via zebra contacts is fixed into holder. LS-FET is in (a) half inside the box and LE-FET in the (b)

At this point, we have successfully brought out electrical contacts from inside of an encapsulated device to outside world.

4.5 Spectral characteristics of integrated system

Transfluospheres are the fluorescent microbeads which are primary assay component in Photo-FET. The different spectral positions of LE-FET, Transfluospheres and short-pass (SP) and long-pass (LP) foil filters are displayed in figure 4.10.

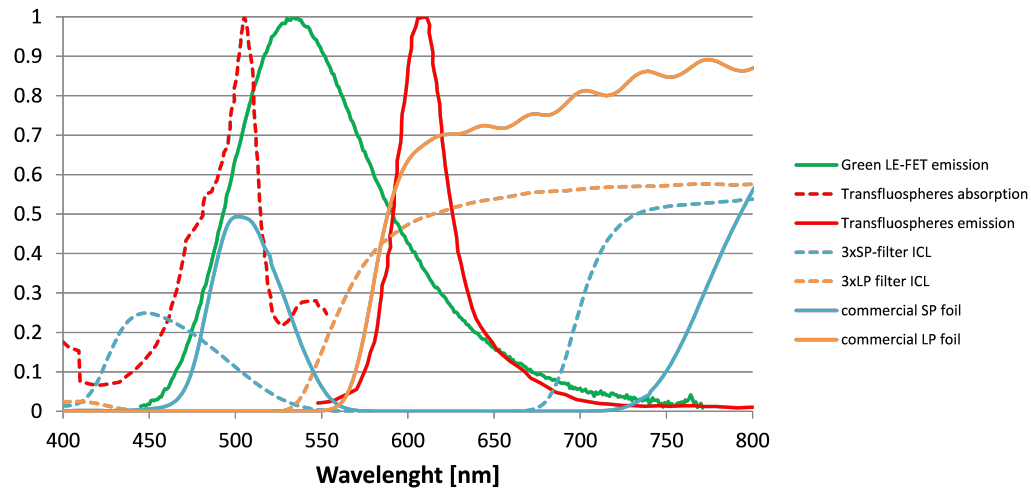


Figure 4.10: arg2 - Graph showing the emission spectrum of the green LE-FET (green curve), the absorption (red dotted curve) and emission (red solid curve) spectra of the Transfluospheres. The dotted blue and orange curve show the transmission spectra of a stack of 3 short-pass (SP) and a stack of 3 long-pass (LP) filters, respectively. The solid blue and orange line display the transmission spectra of a commercial short-pass and long-pass foil filter, respectively.

The emission of the LE-FET does not exactly match the absorption of the Transfluospheres, the spectral overlap is approximately 25%. In terms of filters the commercial SP foil is spectrally better matched with respect to the absorption spectrum of the Transfluospheres and has a five times higher transmission at the peak absorption of the Transfluospheres. A significant tail of the LE-FET emission exists extending up to 750nm. For the green-sensitive P3HT:PCBM based LS-FET and organic photodiodes this is not relevant since the sensitivity of these organic devices is near to zero for wavelength larger than 650 nm.

4.6 Testing FET devices

4.6.1 LE-FET - LS-FET face-to-face

In order to test the integration of LE-FET and LS-FET our strategy is to start from the simplest configuration, the face-to-face detection of emitted light from the LE-FET array by the LS-FET array. The first experiment is to make an I-V sweep of the LS-FET gate voltage from -40 V to +40 V, with and without light (see Figure 4.11). The LE-FET is biased at $V_g = -40V$ and $V_d = -40V$.

The blue and the red curve show the drain current with and without light, respectively. One can observe a clear shift between the two curves, meaning that the LS-FET is capable to detect the light emitted by the LE-FET. The shift within the curves of the same color stems from a hysteresis effect when sweeping from negative to positive gate

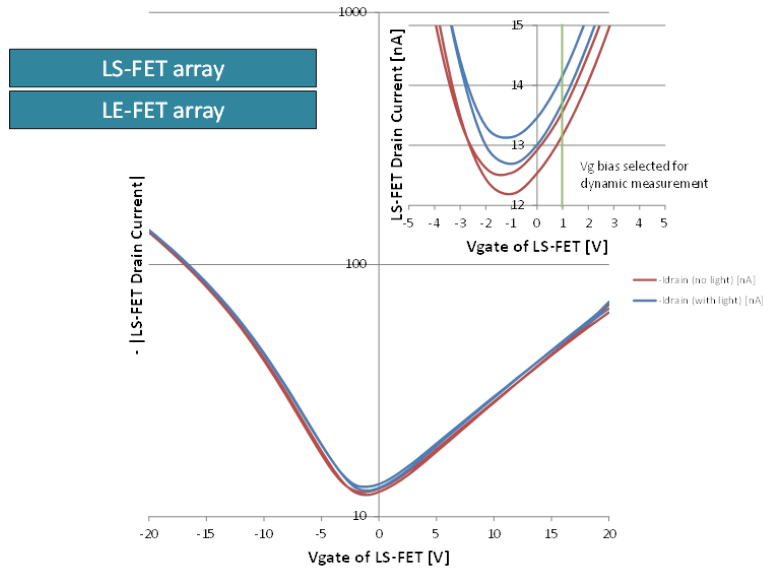


Figure 4.11: - Face-to-face detection of green LE-FET and green-sensitive LS-FET. The LE-FET is biased at V_g : -40V and V_d : -40V. The blue and the red curve show the IV characteristics of the LS-FET with the LE-FET switched on and off, respectively.

voltages or vice versa. At gate voltage of +1V we get good photocurrent gain and is therefore used in the subsequent dynamic measurements. The LS-FET drain current

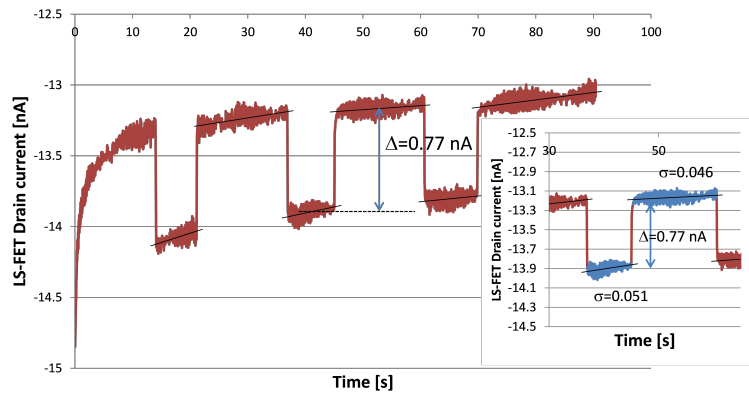


Figure 4.12: - Dynamic measurement showing LS-FET drain current with LE-FET alternately turned on and off. The LE-FET is biased at V_g : -40V, V_d : -40V. A bias of V_g : 1V and V_d : -10V is applied to the LS-FET. The average step difference between the on and the off state is 0.77 nA.

is monitored as a function of time while pulsing the LE-FET on and off (see Figure 4.12). A clear step-response can be observed. The average step difference between the on and the off state is 0.77 nA.

The electroluminescence of LE-FET is depicted in figure 4.13. The average step difference between the on and the off state is 0.77 nA. Considering that the LE-FET was driven at V_g : -40V, V_d : -40V, the emitted power in the green is roughly 105 nW, the sensitivity of the LS-FET for green light in the given configuration is 7.3 mA/W.

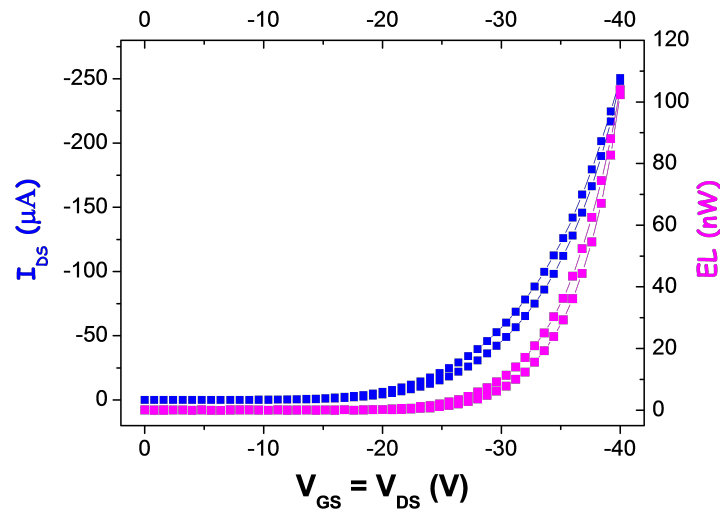


Figure 4.13: - I-V curve and electroluminescent power emitted by the green LE-FET.

4.6.2 LE-FET - Fluidic Chip - LS-FET

As a next step a blank microfluidic chip is inserted between the two devices (see Figure 4.14 (a)) and dynamic measurement is carried out by switching LE-FET on and off. As expected, the insertion of the microfluidic window has reduced signal change to 0.348 nA from off to on state. This reduction is due to the fact that the LE-FET displays Lambertian emission characteristics and any restriction of the emission angles by the microfluidic window reduces the light power accordingly.

In summary green emission from a pixel from LE-FET array was detected by an LS-FET pixel placed face-to-face, with and without a microfluidic window in between. To our knowledge is a unique result demonstrated for the first time. In the next section we will use LE-FET to excite fluorescence in Transfluospheres and Texas Red dye and will try to detect the fluorescent emission by LS-FET.

4.6.3 Fluorescence measurements

For fluorescence excitation and measurements, a transparent BDK tape was laminated onto bottom side of the microfluidic chip. Solutions of Texas Red and Transfluospheres were drop-casted multiple times on the tape inside the fluidic window region to form high concentration of fluorescent dye in the window.

No pulse could be detected on the LS-FET when tested with both Texas Red and Transfluospheres

Based on these results it was clear that during time frame of the project, bio-sensing would not be possible using LE-FET and LS-FET in pair. Decision was made to replace them by a blue OLED and an OPD.

4.7 Blue OLED and OPD

Figure 4.25 shows spectral positions same as before but green LE-FET emission replaced by blue OLED emission. In this case the overlap between OLED emission and the absorption of Transfluospheres is ideal.

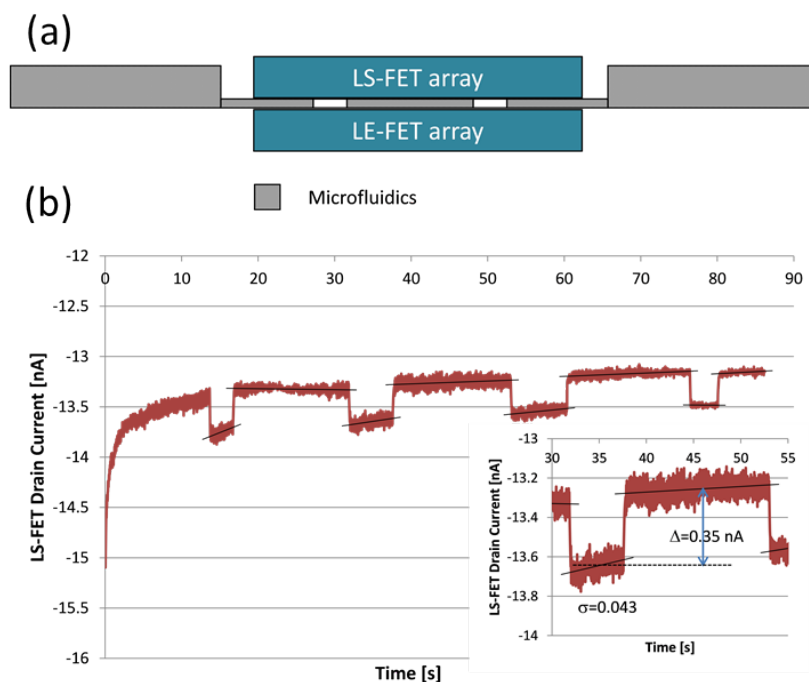


Figure 4.14: - Dynamic measurement showing LS-FET drain current with LE-FET alternately turned on and off. The LE-FET is biased at $V_g:-40V$, $V_d:-40V$. A bias of $V_g: 1V$ and $V_d: -10V$ is applied to the LS-FET. The average step difference between the on and the off state is 0.35 nA

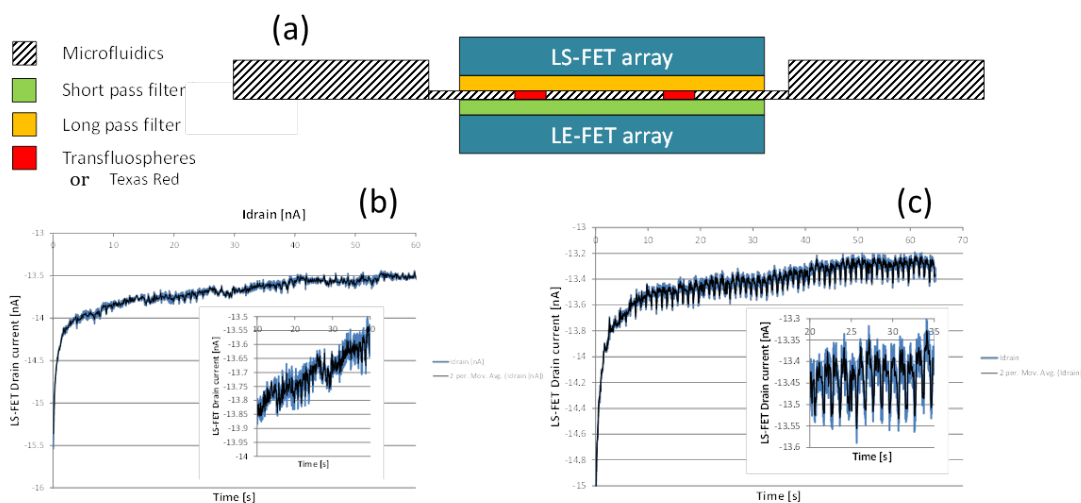


Figure 4.15: - (a) The emission from the LE-FET array is filtered by a short-pass filter foil and excites the highly concentrated Transfluospheres located on the transparent foil laminated to the lower side of the microfluidic cartridge. The fluorescent emission if any, is filtered by a long-pass filter foil and picked up by the LS-FET array. (b) Dynamic measurement showing LS-FET drain current as LE-FET is being switched. The LE-FET is biased at $V_g:-50V$, $V_d:-50V$. A bias of $V_g: 1V$ and $V_d: -10V$ is applied to the LS-FET. No pulse signal can be discriminated. (c) Same as (b) except dye is Texas Red and LE-FET is biased at $V_g:-45V$, $V_d:-45V$. A bias of $V_g: 1V$ and $V_d: -10V$ is applied to the LS-FET. No pulse signal can be discriminated.

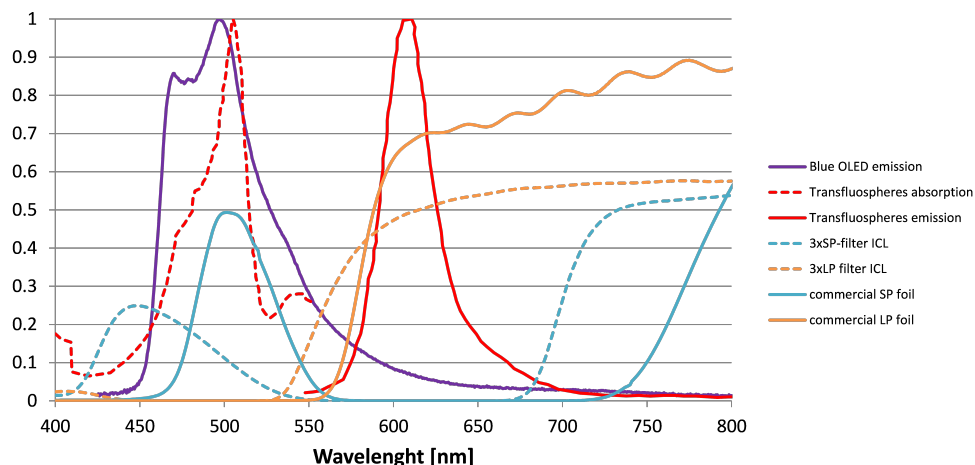


Figure 4.16: - Graph showing the emission spectrum of the blue OLED (violet curve) and the absorption (red dotted curve) and emission (red curve) spectra of the Transfluospheres. The dotted blue and orange curve show the transmission spectra of a stack of 3 SP and a stack of 3 LP filters from ICL, respectively. The solid blue and orange line display the transmission spectra of a commercial SP and LP foil filter, respectively.

Transfluospheres coated fluidic chip from FET testing was sandwiched as: Blue OLED array - short-pass filter - fluidics - long-pass filter - OPD array as shown in 4.17 (a). A dynamic measurement was carried out by pulsing OLED on and off and OPD current was monitored. Another pixel of OPD adjacent to active OPD was also monitored to check pixel cross-talk. Both OPD currents are shown as blue (active) and red (reference) in 4.17 (b). After this successful fluorescence test with OLED-OPD, we made a control experiment by inserting a blank fluidic chip instead of dye containing chip. For the same currents applied to OLED we saw no change in OPD current. This means that what was detected on OPD was indeed fluorescence signal from Transfluospheres.

4.8 Photo-FET Reader

Circumstances were such that out of all light generation and detection devices strongest combination might not be from same family of device. As we found out that LE-FET - LS-FET combination is not adequate. To be able to try all possible combinations, we proposed a modular, portable and yet versatile integrated reader hereafter named as Photo-FET reader or simply reader.

4.8.1 Mechanical Design

A schematic idea is presented in figure 4.18. It was designed into two types of reader each consisting of two halves - upper and lower. Upper halves support OPD, LS-FET or a silicon photodiode while lower halves support OLED, LE-FET or an inorganic LED. All lower halves are mechanically compatible with all upper halves. So in short any possible combination of light source with detector is possible. A mechanical 3D CAD of the reader in same 2x2 combination form is shown in figure 4.19.

The holders accommodate all the electronic boards inside the assembly. Two sections clip into each other with a continuous slot on the perimeter. This slot also acts

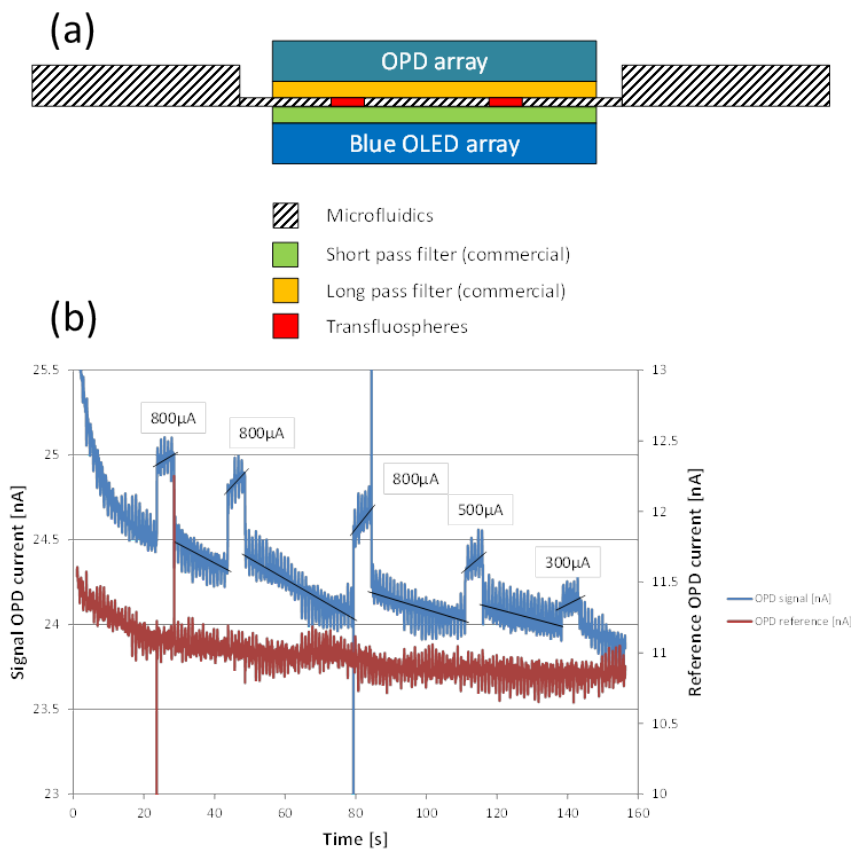


Figure 4.17: - (a) Blue OLED - SP filter - Transfluospheres - LP Filter - OPD configuration (b) Dynamic measurement showing current of OPD (blue curve) with blue OLED alternately turned on and off . OLED is driven with different currents ranging from 800 A down to 300 A mentioned on the plot. A reverse bias of -1V is applied to the OPD. For reference an OPD of an adjacent detection window with no excitation is measured, giving an indication about the cross-talk.(red curve)

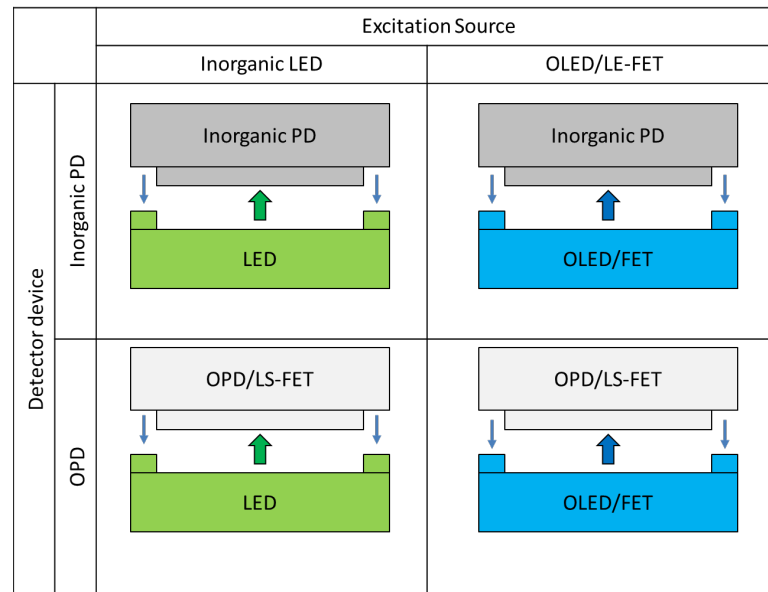


Figure 4.18: Modular integration concept - The final reader layout consists of 2 shells between which the microfluidic chip is placed. The shells contain inorganic LED or OLED/LE-FET and inorganic PD or OPD/LS-FET for the excitation side and the detection side, respectively.

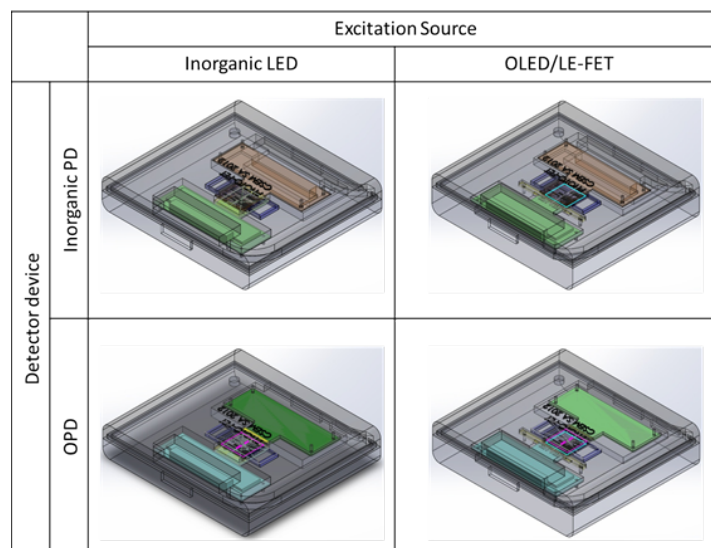


Figure 4.19: Photo-FET reader 3D CAD - CAD representation of the various combinations between excitation source and detector units.

as light shield to prevent ambient light entering the system. Furthermore this slot also provides cable guides. While clipping two halves together we have designed a locking guide in the corner. The electronic boards are hold tightly in place by screws.

4.8.2 Electrical design

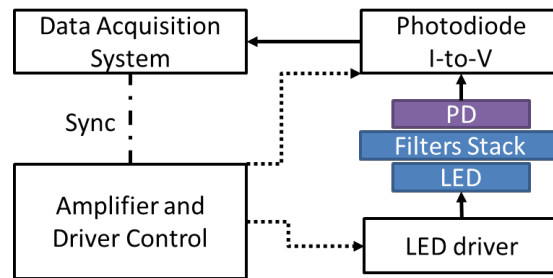


Figure 4.20: PHOTO-FET system architecture - The data acquisition is based on a NI DAQmx device, custom designed circuits for all devices.

The electrical design was divided into three parts namely a switched input integrating transimpedance amplifier for detectors, driver for OLED/LED/LE-FET and control module which was part of data acquisition device. A design schematic is shown in 4.20



Figure 4.21: - Photos of the 4 distinct PCBs: driving electronics for inorganic LEDs, driving electronics for OLEDs/LE-FETs, detection electronics.

Figure 4.21 shows all four electronic boards fixed into their respective holder halves. A software was developed in LabView to acquire, log and process the data.

Special contact mechanism engineered with gold plated zebra connectors and gold plated contacts on PCB provided a hassle free insertion of substrates along with electrical contacts. This mechanism is detailed in Figure 4.22.

Figure 4.23 demonstrates encapsulated blue OLED devices driven by integrated electronics.

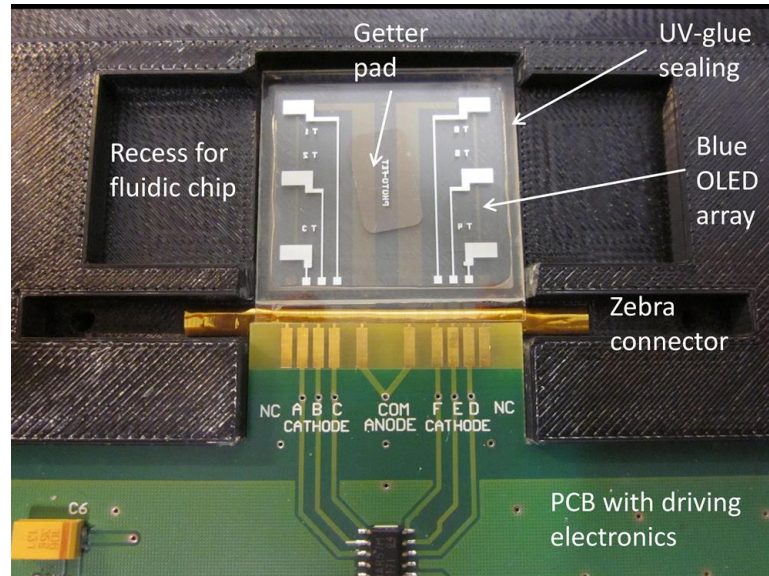


Figure 4.22: - Detailed inside view of OLED/LE-FET holder.

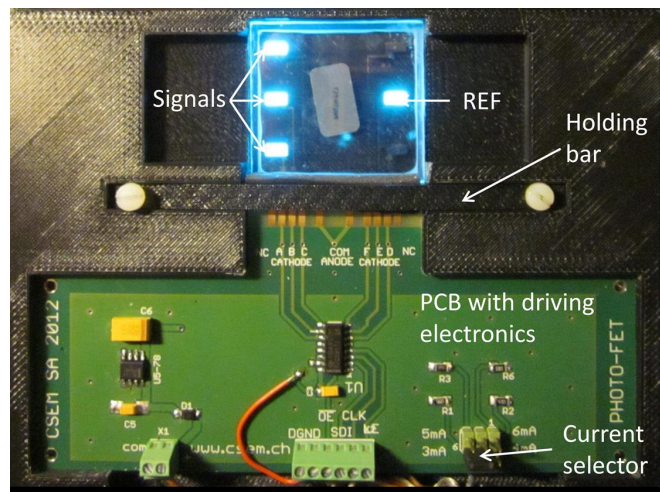


Figure 4.23: - A working blue OLED-array in Photo-FET array design placed in Photo-FET reader.

4.9 Benchmarking of Photo-FET Reader

Molecular Vision's (MV) current testing platform consisted of a single channel excitation and detection system made up of high brightness LED for excitation and a large area ($10 \times 10 \text{mm}^2$) silicon photodiode mounted on an precision x-y stage for perfect manual alignment. Measuring each pixel is a manually adjust and test process. This benchtop platform is shown in figure 4.24. Photo-FET reader on the other hand mea-

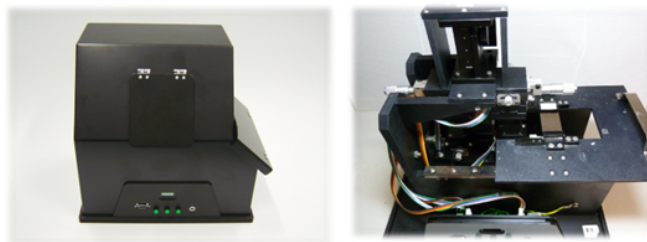


Figure 4.24: - MV's current benchtop test platform.

sured all six channels (3 main and 3 reference) simultaneously and is highly portable¹. Therefore as a final benchmarking, it was decided to perform use same test chips with MV's reader and repeat those tests with Photo-FET reader. Inorganic LED and silicon photodiodes combination was used for benchmarking. Figure 4.25 shows relevant spectral positions of LED with Transfluospheres. To cut near-infrared emission from LED an infrared blocking hot mirror was also used in both system.

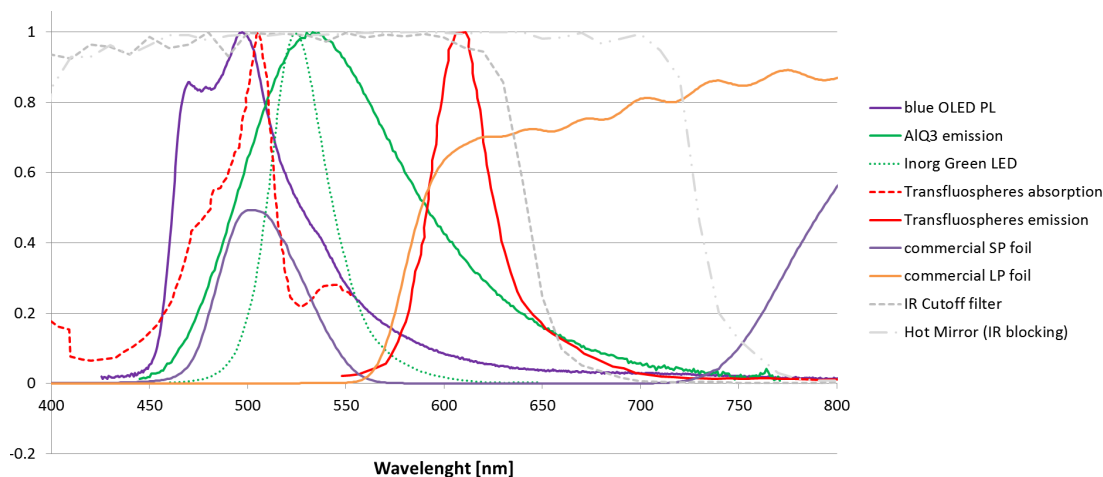


Figure 4.25: - Spectral characteristics of the system. Graph showing the emission spectrum of the blue OLED (violet curve) and the absorption (red dotted curve) and emission (red curve) spectra of the Transfluospheres. The solid light-blue and orange line display the transmission spectra of a commercial short-pass and long-pass foil filter, respectively. Emission of inorganic green LED (green dotted) and IR blocking filters with cut-off at 700 nm and 750 nm (grey dashed) are also shown.

Figure 4.26 shows test chip in cross-section. Green LED emission is filtered by a short-pass filter of blue and green specifically to pass only the wavelengths below 530nm. It passes through a linear polarizer foil and enters microfluidic chamber. The

¹I had carried the reader to Italy in my bag, transported to-from MV's office in London via courier, it still works.

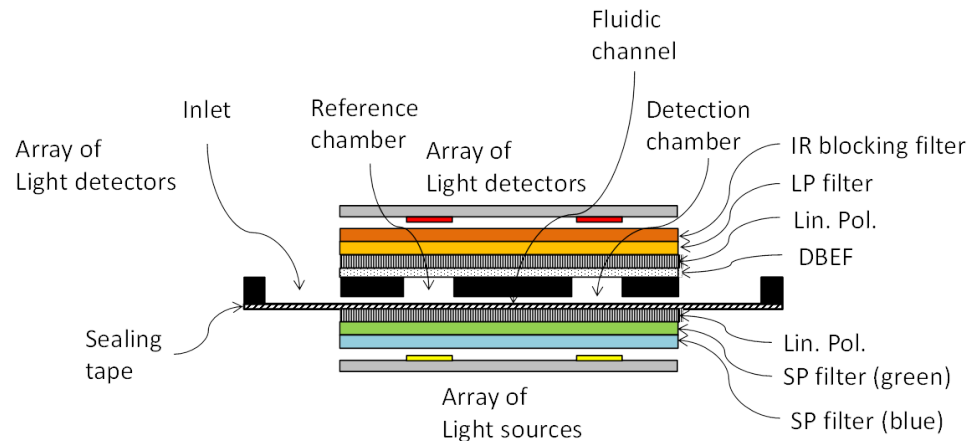


Figure 4.26: - Chip cross-section

three cardiac markers assay based on Transfluospheres namely Troponin-I, CK-MB and Myoglobin (one in each channel) runs passively through the chip. Analyte is captured on DBEF polarizer foil which is a reflective foil recycling the excitation light many times in the channel exciting more fluorescence. This emission along with part of excitation then passes through second crossed linear polarizer and long-pass filter to block almost all of green light from LED. IR filter blocks the electroluminescent tail from LED and silicon photodiodes on other side detect mainly the Transfluospheres emission.

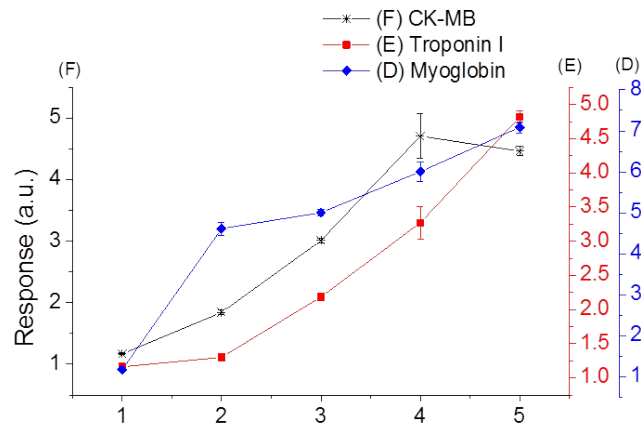


Figure 4.27: - Dose-response curve obtained with Photo-FET reader

Figure 4.27 shows dose response obtained with five chips measured at CSEM SA which were pre-measured by MV. They have similar response. At this point platform was validated with single test.

Later on, as a part of deliverable of the project, MV carried out extensive testing with the reader and the results of comparison between MV's benchtop reader and Photo-FET reader are presented in figure 4.28. Photo-FET reader performs equal or better than benchtop reader. In coefficient of variation (CV) tests (not shown here but in the final report of Photo-FET) too Photo-FET reader performed better or equal with benchtop reader.

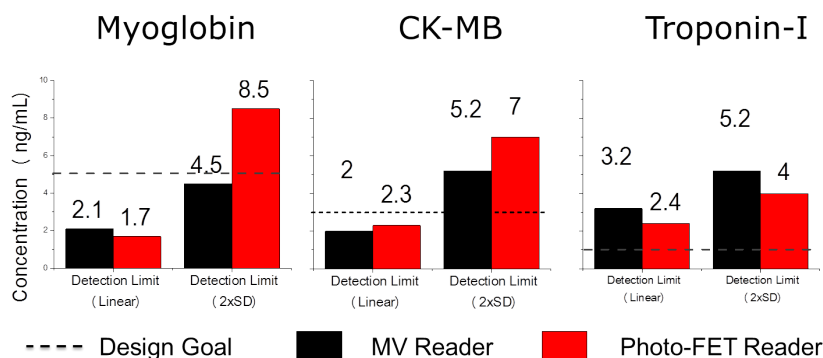


Figure 4.28: - Final Performance Comparison between MV's benchtop reader and Photo-FET reader.

4.9.1 OLED - Si Photodiode Test

We also performed same test with 5 chips using OLED and silicon photodiode pair. The response for each concentration is shown in 4.29 (a) and extracted response is in (b). As observed, though the signal is obtained it stays within the standard deviation of the signal. This may come from two main contributions - either long electroluminescent tail of blue OLED which is not blocked by filter stack or blue OLED power is simply not enough to excite fluorescence signal above background signal. (OLED $60\mu W/cm^2$ compared with in-organic LED which is 100s to 1000s $\mu W/cm^2$)

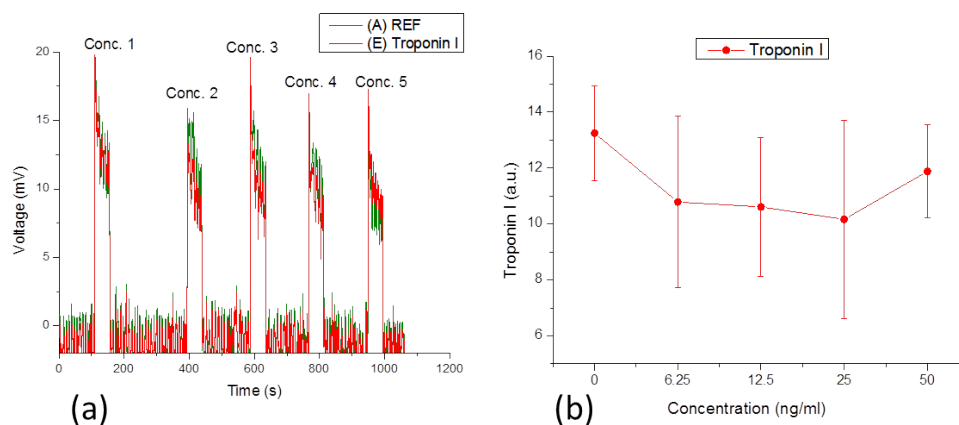


Figure 4.29: OLED - Silicon photodiode combination - Left shows real time response from chip to chip. Right graph shows individual dose extracted.

4.10 Conclusions

LE-FET devices are very promising for integration with sensing applications. In the head-on geometry in Photo-FET array structure, rectangular excitation pulses emitted by a green Alq3-based LE-FET were successfully picked-up and quantitatively measured with a green-sensitive P3HT:PCBM-based LS-FET. This is, to our best knowledge, a world premier! The absolute power emitted (\approx few hundreds of nW) by LE-FETs still has to improve to become more relevant into real world applications.

When tried to measure fluorescence excitation and emission by LE-FET and LS-FET respectively, no signal could be detected, using proper combination of filter stack. The signal is basically covered by the electronic noise even though the fluorophores concentration was much higher compared to typical concentrations used by MV.

The integration platform we developed is highly versatile and allows to test all the devices developed in the Photo FET project, including electro-optical and fluidic systems. Several combinations of light sources and detectors thanks could be benchmarked. Namely these include:

- inorganic light source and detector configuration, allowed benchmarking with the MVs existing bench-top device testing platform
- OLED platform (organic light source and inorganic detector)
- LS-FET and LE-FET platform

Multiple concentration assay chips from all three tests (myoglobin, troponin-I and CK-MB) were measured on both the MV's reader and the Photo-FET reader. Similar calibration curves were obtained. This demonstrated the successful development of a modular optical fluorescence reader capable of simultaneously measuring the amount of analyte in three different cardiac assays all on a disposable microfluidic based test chip. This is a significant result as it reduces the testing workhorse from a bench-top, single channel to a much more compact and portable format.

Conclusions and Outlook

Three different architectures of fluorescence detection based sensor platforms are demonstrated. Each one trying to solve different problems using various approaches.

BioPLC platform's main strength lies in efficient coupling of photoluminescent emission into a single mode waveguide without using gratings (> 25%). We started with a settings using MEH-PPV as PL layer which creates massive background signal due to large overlapping of emission spectra of PL and analyte fluorophore. From such sub-optimal combination, platform improved with each experiment going from a minimum detected concentration of $100\mu\text{g}/\text{ml}$ to finally reaching $7\mu\text{g}/\text{ml}$. It minimized the problem of PL layer decay by using F8BT layer combined with good encapsulation. Reduction in overlap was achieved by using large Stoke shift (>100nm) fluorophore Surelight P1. Prevention or further reduction of the overlap or absorbing the tail emissions must be primary goal of any future technical work. Because any strategy to enhance fluorescence signal gain from analyte will in turn also increase contribution from PL layer. We also manufactured a portable demonstrator for BioPLC platform.

BioCOP platform started with exploration of an idea to overcome integration problem. We identified a major problem of assembly of multiple components especially the fluidic channel. A solution of double sided simultaneous embossing of those structure was demonstrated. All the components were systematically designed along with detailed formulation. With fabricated designs dose-response curves were obtained. Experiments progressively improved the limit of detection (LOD) to $100\text{ng}/\text{ml}$ (6.6pM). During this work a programmable gain, integrating transimpedance amplifier circuit board was designed. The complete control system combined with precision clock control is available for use. The amplifier was extensively used in the Photo-FET project. Capability of design and fabrication of high in-coupling efficiency gratings on plastic substrates along with integrated fluidics was exploited and demonstrated.

Photo-FET project was an EU project which completed at the end of 2012. Overall the project was successful and we received good review from EU commission. Technically LE-FET and LS-FET integration was demonstrated into a portable platform. However the performance were not adequate regarding their bio-sensing capabilities. The Photo-FET reader developed during the project was highly successful performing equal or better than an expensive benchtop reader.

BioPLC platform is based upon single mode Ta_2O_5 waveguide deposited on glass. While BioCOP and PhotoFET are based upon mass producible plastic substrate. Their comparison from cost perspective is in table 5.1.

Table 5.1: Comparison of platforms from cost perspective

	BioPLC	BioCOP	PhotoFET
Consumable Substrate Cost	High	Very Low	Low
Fully disposable platform	Possible	No	Yes
Reader Cost	Very Low	Medium	Low

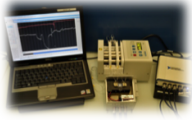

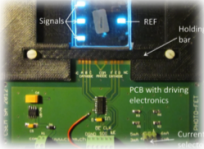

	Bio-PLC	Bio-COP	Photo-FET	TRIAGE®
LoD	 IgG assay 7 µg/ml (462 pM)	 IgG assay 100 ng/ml (6.6 pM)	 Myoglobin 1.3 ng/ml CK-MB 2.3 ng/ml Troponin-I 2.4 ng/ml (approx 100 pM)	 170 ng/ml 10 ng/ml 1 ng/ml

Figure 5.1: Platforms Comparison - Comparison of the platforms developed during the work. BioPLC and BioCOP platform used similar immunoassay and analyte. Photo-FET work is compared with the equivalent commercially available system.

From maturity point of view Photo-FET platform or Molecular Vision's platform is at very high maturity. Advantages of Photo-FET like direct through illumination is that it is independent from many of the optical and geometrical properties of the chip. MV is developing their product platform based on OPDs and in-organic LEDs and we hope to see their product soon.

BioCOP and BioPLC have both passed proof of concept stage and are in feasibility stage. BioCOP chip can be tuned to any given specification with minimal effort using formulations presented in the thesis. It has opportunity to explore more. Integration of other types of sensing schemes in the fluidic chamber could enhance the signal gain. It is not necessarily limited to evanescently excited fluorescence only.

Bibliography

- [1] CURTIS D CHIN, VINCENT LINDER, AND SAMUEL K SIA. **Commercialization of microfluidic point-of-care diagnostic devices.** *Lab on a chip*, **12**(12):2118–34, June 2012. 1
- [2] LUC GERVAIS AND EMMANUEL DELAMARCHE. **Toward one-step point-of-care immunodiagnosics using capillary-driven microfluidics and PDMS substrates.** *Lab on a chip*, **9**(23):3330–7, December 2009. 2
- [3] D. M. BRULS, T. H. EVERS, J. A. H. KAHLMAN, P. J. W. VAN LANKVELT, M. OVSYANKO, E. G. M. PELSSERS, J. J. H. B. SCHLEIPEN, F. K. DE THELJE, C. A. VERSCHUREN, T. VAN DER WIJK, J. B. A. VAN ZON, W. U. DITTMER, A. H. J. IMMINK, J. H. NIEUWENHUIS, AND M. W. J. PRINS. **Rapid integrated biosensor for multiplexed immunoassays based on actuated magnetic nanoparticles.** *Lab on a chip*, **9**(24):3504–10, December 2009. 2, 3
- [4] TERESA MAIRAL, INES FRESE, ENRIQUE LLAUDET, CARMEN BERMUDO REDONDO, IOANIS KATAKIS, FRITHJOF VON GERMAR, KLAUS DRESE, AND CIARA K O’ SULLIVAN. **Microfluorimeter with disposable polymer chip for detection of coeliac disease toxic gliadin.** *Lab on a chip*, **9**(24):3535–42, December 2009. 2
- [5] THOMAS LEEUW, EMMANUEL S BOSS, AND DANA L WRIGHT. **In situ measurements of phytoplankton fluorescence using low cost electronics.** *Sensors (Basel, Switzerland)*, **13**(6):7872–83, January 2013. 2
- [6] MICHAEL PAWLAK, EGINHARD SCHICK, MARTIN A BOPP, MICHAEL J SCHNEIDER, PETER OROSZLAN, AND MARKUS EHRAT. **Zeptosens’ protein microarrays: a novel high performance microarray platform for low abundance protein analysis.** *Proteomics*, **2**(4):383–93, April 2002. 2, 11
- [7] DOROTA WENCEL, JOHN P MOORE, NIALL STEVENSON, AND COLETTE McDONAGH. **Ratio-metric fluorescence-based dissolved carbon dioxide sensor for use in environmental monitoring applications.** *Analytical and bioanalytical chemistry*, **398**(5):1899–907, November 2010. 2
- [8] THOMAS RUCKSTUHL, CHRISTIAN M WINTERFLOOD, STEFAN SEEGER, AND PHYSIKALISCH-CHEMISCHES INSTITUT. **Supercritical angle fluorescence immunoassay platform.** *Analytical chemistry*, **83**(6):2345–50, March 2011. 2, 4
- [9] RUDOLF KRKA AND ALEXANDRA MOLINELLI. **Rapid test strips for analysis of mycotoxins in food and feed.** *Analytical and bioanalytical chemistry*, **393**(1):67–71, January 2009. 2
- [10] FRANCESCO BALDINI, ADOLFO CARLONI, AMBRA GIANNETTI, GIAMPIERO PORRO, AND COSIMO TRONO. **An optical PMMA biochip based on fluorescence anisotropy: Application to C-reactive protein assay.** *Sensors and Actuators B: Chemical*, **139**(1):64–68, May 2009. 2, 4, 56
- [11] YANLING QIAO, HONGMIN TANG, GERHARD R MUNSKE, PRASHANTA DUTTA, CORNELIUS F IVORY, AND WEN-JI DONG. **Enhanced fluorescence anisotropy assay for human cardiac troponin I and T detection.** *Journal of fluorescence*, **21**(6):2101–10, November 2011. 2, 5
- [12] DEREK TSENG, ONUR MUDANYALI, CETIN OZTOPRAK, SERHAN O ISIKMAN, IKBAL SENCAN, OGUZHAN YAGLIDERE, AND AYDOGAN OZCAN. **Lensfree microscopy on a cellphone.** *Lab on a chip*, **10**(14):1787–92, July 2010. 6
- [13] ONUR MUDANYALI, STOYAN DIMITROV, UZAIR SIKORA, SWATI PADMANABHAN, ISA NAVRUZ, AND AYDOGAN OZCAN. **Integrated rapid-diagnostic-test reader platform on a cellphone.** *Lab on a chip*, **12**(15):2678–86, August 2012. 6
- [14] LI SHEN, JOSHUA A HAGEN, AND IAN PA-PAUTSKY. **Point-of-care colorimetric detection with a smartphone.** *Lab on a chip*, **12**(21):4240–3, November 2012. 6
- [15] ISA NAVRUZ, AHMET F COSKUN, JUSTIN WONG, SAQIB MOHAMMAD, DEREK TSENG, RICHIE NAGI, STEPHEN PHILLIPS, AND AYDOGAN OZCAN. **Smart-phone based computational microscopy using multi-frame contact imaging on a fiber-optic array.** *Lab on a chip*, **13**(20):4015–23, October 2013. 6
- [16] QINGSHAN WEI, HANGFEI QI, WEI LUO, DEREK TSENG, SO JUNG KI, ZHE WAN, ZOLTÁN GÖRÖCS, LAURENT A BENTOLILA, TING-TING WU, REN SUN, AND AYDOGAN OZCAN. **Fluorescent Imaging of Single Nanoparticles and Viruses on a Smart Phone.** *ACS nano*, (Xx), September 2013. 6
- [17] HONGYING ZHU, IKBAL SENCAN, JUSTIN WONG, STOYAN DIMITROV, DEREK TSENG, KEITA NAGASHIMA, AND AYDOGAN OZCAN. **Cost-effective and rapid blood analysis on a cell-phone.** *Lab on a chip*, **13**(7):1282–8, April 2013. 6
- [18] AHMET F COSKUN, JUSTIN WONG, DELARAM KHODADADI, RICHIE NAGI, ANDREW TEY, AND AYDOGAN OZCAN. **A personalized food allergy testing platform on a cellphone.** *Lab on a chip*, **13**(4):636–40, February 2013. 6

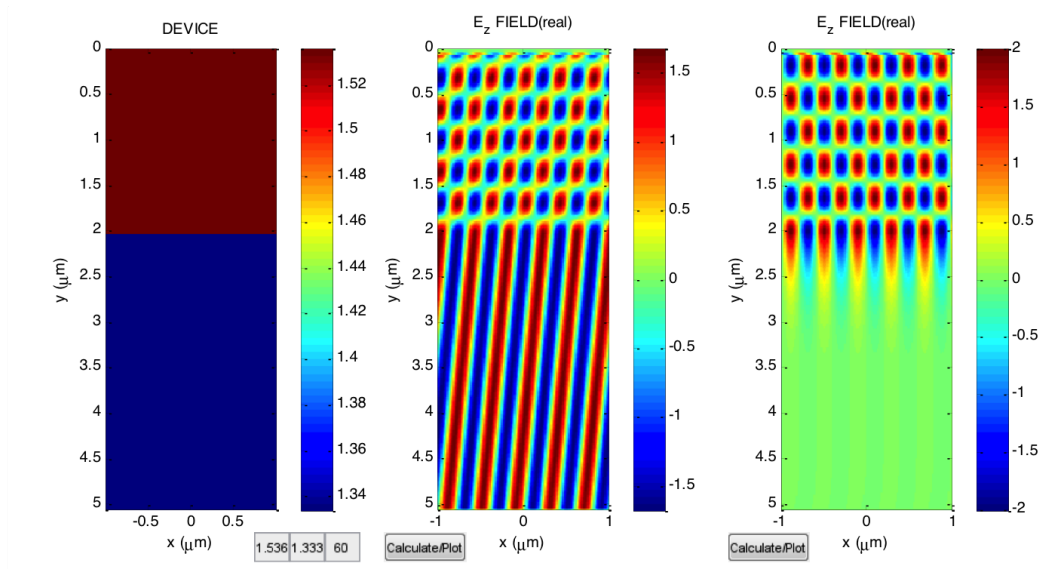
- [19] AHMET F COSKUN, RICHIE NAGI, KAYVON SADEGHI, STEPHEN PHILLIPS, AND AYDOGAN OZCAN. **Albumin testing in urine using a smart-phone.** *Lab on a chip*, pages 4231–4238, August 2013. 6
- [20] DAVID WILD, editor. *The Immunoassay Handbook*. Elsevier, 4th edition, 2013. 5
- [21] J.D. ANDRADE, R.A. VANWAGENEN, D.E. GREGONIS, K. NEWBY, AND J.-N. LIN. **Remote fiber-optic biosensors based on evanescent-excited fluoro-immunoassay: Concept and progress.** *IEEE Transactions on Electron Devices*, **32**(7):1175–1179, July 1985. 11
- [22] BJÖRN AGNARSSON, SAEVAR INGTHORSSON, THORARINN GUDJONSSON, AND KRISTJAN LEOSSON. **Evanescent-wave fluorescence microscopy using symmetric planar waveguides.** *Optics express*, **17**(7):5075–82, March 2009. 11
- [23] R. P. STANLEY M. RAMUZ, D. LEUENBERGER, C. WINNEWISSER. **LIGHT COUPLING DEVICE AND SYSTEM, AND METHOD FOR MANUFACTURING THE DEVICE AND SYSTEM.** 12
- [24] MARC RAMUZ, LUKAS BURGI, ROSS STANLEY, AND CARSTEN WINNEWISSER. **Coupling light from an organic light emitting diode (OLED) into a single-mode waveguide: Toward monolithically integrated optical sensors.** *Journal of Applied Physics*, **105**(8):084508, 2009. 12
- [25] MARC RAMUZ, DAVID LEUENBERGER, AND LUKAS BÜRGI. **Optical biosensors based on integrated polymer light source and polymer photodiode.** *Journal of Polymer Science Part B: Polymer Physics*, **49**(1):80–87, January 2011. 12, 20
- [26] ARJAN BERNTSEN, YVO CROONEN, COEN LIEDENBAUM, HERMAN SCHOO, ROBERT-JAN VISSER, JEROEN VLEGGAR, AND PETER VAN DE WELJER. **Stability of polymer LEDs.** *Optical Materials*, **9**(1-4):125–133, January 1998. 12
- [27] MARC RAMUZ. *Integration of Organic Optoelectronic Devices for Biosensing Applications*. PhD thesis, University of Neuchâtel, 2009. 16, 20, 21
- [28] H. SIRRINGHAUS. **Device Physics of Solution-Processed Organic Field-Effect Transistors.** *Advanced Materials*, **17**(20):2411–2425, October 2005. 17
- [29] KYOHEI KOIWA, HIROTAKE KAJII, AND YUTAKA OHMORI. **Fabrication and characteristics of ambipolar, light-emitting organic field effect transistors utilizing blended polyfluorene derivatives.** *physica status solidi (c)*, **8**(2):610–612, February 2011. 17
- [30] BERNARD WENGER, NICOLAS TETREAU, MARK E. WELLAND, AND RICHARD H. FRIEND. **Mechanically tunable conjugated polymer distributed feedback lasers.** *Applied Physics Letters*, **97**(19):193303, 2010. 17, 18
- [31] W LUKOSZ. **Light emission by magnetic and electric dipoles close to a plane dielectric interface III Radiation patterns of dipoles with arbitrary orientation.** *Journal of the Optical Society of America*, **69**(11):1495, November 1979. 20, 87
- [32] W. LUKOSZ. **Light emission by multipole sources in thin layers I Radiation patterns of electric and magnetic dipoles.** *Journal of the Optical Society of America*, **71**(6):744, June 1981. 20, 87
- [33] EDWARD H. HELLEN AND DANIEL AXELROD. **Fluorescence emission at dielectric and metal-film interfaces.** *Journal of the Optical Society of America B*, **4**(3):337, March 1987. 20
- [34] LUKAS NOVOTNY AND HECHT BERT. *Principles of Nano-Optics*. Cambridge University Press, 2011 edition. 20, 21, 87
- [35] R. BAUMNER, K. BODENSIEK, A. SELLE, T. FRICKE-BEGEMANN, J. IHLEMANN, AND G. MAROWSKY. **Efficiency of fluorescence coupling into planar waveguides.** *Proceedings of SPIE*, **7368**(551):736828–736828–7, 2009. 20, 21
- [36] CLAUS F. KLINGSHIRN. **Semiconductor Optics**, 1996. 20
- [37] LAURA GONZALEZ-MACIA, AOIFE MORRIN, MALCOLM R SMYTH, AND ANTHONY J KILLARD. **Advanced printing and deposition methodologies for the fabrication of biosensors and biodevices.** *The Analyst*, **135**(5):845–867, 2010. 22
- [38] GERT L DUVENECK, ANDREAS P ABEL, MARTIN A BOPP, GERHARD M KRESBACH, AND MARKUS EHRT. **Planar waveguides for ultra-high sensitivity of the analysis of nucleic acids.** *Analytica Chimica Acta*, **469**(1):49–61, September 2002. 23
- [39] MEL N. KRONICK AND WILLIAM A. LITTLE. **A new immunoassay based on fluorescence excitation by internal reflection spectroscopy.** *Journal of Immunological Methods*, **8**(3):235–240, September 1975. 23
- [40] I. A. AVRUTSKY, A. S. SVAKHIN, V. A. SYCHUGOV, AND O. PARRIAUX. **High-efficiency single-order waveguide grating coupler.** *Optics Letters*, **15**(24):1446, December 1990. 24
- [41] M B WABUYELE, S M FORD, W STRYJEW-SKI, J BARROW, AND S A SOPER. **Single molecule detection of double-stranded DNA in poly(methylmethacrylate) and polycarbonate microfluidic devices.** *Electrophoresis*, **22**(18):3939–48, October 2001. 25
- [42] KENNETH R HAWKINS AND PAUL YAGER. **Non-linear decrease of background fluorescence in polymer thin-films - a survey of materials and how they can complicate fluorescence detection in microTAS.** *Lab on a chip*, **3**(4):248–52, November 2003. 25

- [43] AIGARS PIRUSKA, IRENA NIKCEVIC, SE HWAN LEE, CHONG AHN, WILLIAM R HEINEMAN, PATRICK A LIMBACH, AND CARL J SELISKAR. **The autofluorescence of plastic materials and chips measured under laser irradiation.** *Lab on a chip*, **5**(12):1348–54, December 2005. 25
- [44] (TOPAS ADVANCED POLYMERS). **COC Product Information.** 26
- [45] CHUN-HAN WU, CHUN-HWA CHEN, KUO-WEI FAN, WEN-SYANG HSU, AND YU-CHENG LIN. **Design and fabrication of polymer microfluidic substrates using the optical disc process.** *Sensors and Actuators A: Physical*, **139**(1-2):310–317, September 2007. 26
- [46] (LIFETECHNOLOGIES). <http://www.lifetechnologies.com/europe/other/en/home/life-science/cell-analysis/labeling-chemistry/fluorescence-spectraviewer.html>. 26
- [47] J P MORSEMAN, M W MOSS, S J ZOHA, AND F C ALLNUTT. **PBXL-1: a new fluorochrome applied to detection of proteins on membranes.** *BioTechniques*, **26**:559–563, 1999. 26
- [48] S J ZOHA, S RAMNARAIN, J P MORSEMAN, M W MOSS, F C T ALLNUTT, Y H ROGERS, AND B HARVEY. **PBXL fluorescent dyes for ultrasensitive direct detection.** *Journal of Fluorescence*, **9**:197–208, 1999. 26
- [49] LUC GERVAIS, NICO DE ROOIJ, AND EMMANUEL DELAMARCHE. **Microfluidic chips for point-of-care immunodiagnostics.** *Advanced materials (Deerfield Beach, Fla.)*, **23**(24):H151–76, June 2011. 27
- [50] LYDÉRIC BOCQUET AND ELISABETH CHARLAIX. **Nanofluidics, from bulk to interfaces.** *Chemical Society reviews*, **39**(3):1073–95, March 2010. 27
- [51] BAHAA E. A. SALEH AND MALVIN CARL TEICH. *Fundamentals of Photonics.* Wiley Series in Pure and Applied Optics. John Wiley & Sons, Inc., New York, USA, August 1991. 27
- [52] C F CARLBORG, K B GYLFASON, A KAŹMIERCZAK, F DORTU, M J BAÑULS POLO, A MAQUEIRA CATALA, G M KRESBACH, H SOHLSTRÖM, T MOH, L VIVIEN, J POPPLEWELL, G RONAN, C A BARRIOS, G STEMME, AND W VAN DER WIJNGAART. **A packaged optical slot-waveguide ring resonator sensor array for multiplex label-free assays in labs-on-chips.** *Lab on a chip*, **10**(3):281–90, February 2010. 29
- [53] HANS ZAPPE. *Fundamentals of Micro-Optics.* Cambridge University Press, 2010. 37
- [54] T.K. GAYLORD AND M.G. MOHARAM. **Analysis and applications of optical diffraction by gratings.** *Proceedings of the IEEE*, **73**(5):894–937, 1985. 40
- [55] XIAOCHUN WU, FACHUN LAI, LIMEI LIN, JING LV, BINPING ZHUANG, QU YAN, AND ZHIGAO HUANG. **Optical inhomogeneity of ZnS films deposited by thermal evaporation.** *Applied Surface Science*, **254**(20):6455–6460, August 2008. 48
- [56] GIHAN RYU, JINGSONG HUANG, OLIVER HOFMANN, CLAIRE A WALSH, JASMINE Y Y SZE, GARETH D MCCLEAN, ALAN MOSLEY, SIMON J RATTLE, JOHN C DEMELLO, ANDREW J DEMELLO, AND DONAL D C BRADLEY. **Highly sensitive fluorescence detection system for microfluidic lab-on-a-chip.** *Lab on a chip*, **11**(9):1664–70, May 2011. 49
- [57] LI-HONG LIU AND MINGDI YAN. **Perfluorophenyl azides: new applications in surface functionalization and nanomaterial synthesis.** *Accounts of chemical research*, **43**(11):1434–43, November 2010. 51
- [58] NORBERT SPRENGER, HUI GAO, AND HANS SIGRIST. **Polysaccharides for functional biomolecule display on surfaces.** *BTi, Microarrays*, (September), September 2005. 54
- [59] OLIVER G WEINGART, HUI GAO, FRANÇOIS CREVOISIER, FRIEDRICH HEITGER, MARC-ANDRÉ AVONDET, AND HANS SIGRIST. **A bioanalytical platform for simultaneous detection and quantification of biological toxins.** *Sensors (Basel, Switzerland)*, **12**(2):2324–39, January 2012. 54
- [60] ISABELLE CAELEN, HUI GAO, AND HANS SIGRIST. **Protein Density Gradients on Surfaces.** *Langmuir*, **18**(7):2463–2467, April 2002. 54
- [61] THOMAS RUCKSTUHL, J ENDERLEIN, STEFAN JUNG, STEFAN SEEGER, AND PHYSIKALISCH-CHEMISCHES INSTITUT. **Forbidden light detection from single molecules.** *Analytical chemistry*, **72**(9):2117–23, May 2000. 56
- [62] JULIO RABA AND HORACIO A. MOTTOLA. **Glucose Oxidase as an Analytical Reagent.** *Critical Reviews in Analytical Chemistry*, **25**(1):1–42, September 1995. 59
- [63] STEPHEN R FORREST. **The path to ubiquitous and low-cost organic electronic appliances on plastic.** *Nature*, **428**(6986):911–8, April 2004. 59
- [64] JASON R WOJCIECHOWSKI, LISA C SHRIVER-LAKE, MARIKO Y YAMAGUCHI, ERWIN FÜREDER, ROLAND PIELER, MARTIN SCHAMESBERGER, CHRISTOPH WINDER, HANS JÜRGEN PRALL, MAX SONNLEITNER, AND FRANCES S LIGLER. **Organic photodiodes for biosensor miniaturization.** *Analytical chemistry*, **81**(9):3455–61, May 2009. 59
- [65] ERIN L RATCLIFF, P ALEX VENEMAN, ADAM SIMMONDS, BRIAN ZACHER, DANIEL HUEBNER, S SCOTT SAAVEDRA, AND NEAL R ARMSTRONG. **A planar, chip-based, dual-beam refractometer using an integrated organic light-emitting diode (OLED) light source and organic photovoltaic (OPV) detectors.** *Analytical chemistry*, **82**(7):2734–42, April 2010. 59

- [66] FRANCES S LIGLER. **Perspective on optical biosensors and integrated sensor systems.** *Analytical chemistry*, **81**(2):519–26, January 2009. 59
- [67] OLIVER HOFMANN, PAUL MILLER, PAUL SULLIVAN, TIMOTHY S JONES, C JOHN, DONAL D C BRADLEY, AND J ANDREW. **Thin-film organic photodiodes as integrated detectors for microscale chemiluminescence assays.** *Sensors and Actuators B: Chemical*, **106**(2):878–884, May 2005. 59
- [68] OLIVER HOFMANN, XUHUA WANG, JOHN C DEMELLO, DONAL D C BRADLEY, AND ANDREW J DEMELLO. **Towards microalbuminuria determination on a disposable diagnostic microchip with integrated fluorescence detection based on thin-film organic light emitting diodes.** *Lab on a chip*, **5**(8):863–8, August 2005. 59
- [69] XUHUA WANG, OLIVER HOFMANN, RUPA DAS, EDWARD M BARRETT, ANDREW J DEMELLO, JOHN C DEMELLO, AND DONAL D C BRADLEY. **Integrated thin-film polymer/fullerene photodetectors for on-chip microfluidic chemiluminescence detection.** *Lab on a chip*, **7**(1):58–63, January 2007. 59
- [70] OLIVER HOFMANN, XUHUA WANG, ALASTAIR CORNWELL, STEPHEN BEECHER, AMAL RAJA, DONAL D C BRADLEY, ANDREW J DEMELLO, AND JOHN C DEMELLO. **Monolithically integrated dye-doped PDMS long-pass filters for disposable on-chip fluorescence detection.** *Lab on a chip*, **6**(8):981–7, August 2006. 59
- [71] JOSHUA B EDEL, NIGEL P BEARD, OLIVER HOFMANN, JOHN C DEMELLO, DONAL D C BRADLEY, AND ANDREW J DEMELLO. **Thin-film polymer light emitting diodes as integrated excitation sources for microscale capillary electrophoresis.** *Lab on a chip*, **4**(2):136–40, April 2004. 59
- [72] MICHELE MUCCINI. **A bright future for organic field-effect transistors.** *Nature materials*, **5**(8):605–13, 2006. 61
- [73] RAFFAELLA CAPELLI, STEFANO TOFFANIN, GIANLUCA GENERALI, HAKAN USTA, ANTONIO FACCHETTI, AND MICHELE MUCCINI. **Organic light-emitting transistors with an efficiency that outperforms the equivalent light-emitting diodes.** *Nature materials*, **9**(6):496–503, June 2010. 61, 62
- [74] T OKUBO, Y KOKUBO, K HATTA, R MATSUBARA, M ISHIZAKI, Y UGAJIN, N SEKINE, N KAWASHIMA, T FUKUDA, A NOMOTO, T OHE, N KOBAYASHI, K NOMOTO, AND J KASAHARA. **10.5-in. VGA all-printed flexible organic TFT backplane for electrophoretic displays.** In *IDW '07: PROCEEDINGS OF THE 14TH INTERNATIONAL DISPLAY WORKSHOPS, VOLS 1-3*, pages 463–464, KIKAI-SHINKO-KAIKAN, 3-5-8 SHIBAKOEN, MINATO-KU, TOKYO 105-0011, JAPAN, 2007. INST IMAGE INFORMATION & TELEVISION ENGINEERS. 62
- [75] MONIQUE J. BEENHAKKERS, KRIS MYNY, GERWIN H. GELINCK, SOEREN STEUDEL, NICK A.J.M. VAN AERLE, PETER VICCA, PAUL HEREMANS, WIM DEHAENE, AND JAN GENOE. **Plastic circuits and tags for 13.56MHz radio-frequency communication**, 2009. 62
- [76] S JUNG, T JI, AND V K VARADAN. **Organic thin films based sensor applications.** In *Proceedings of SPIE - The International Society for Optical Engineering*, **6172**, 2006. 62
- [77] YONG-YOUNG NOH, DONG-YU KIM, AND KIYOSHI YASE. **Highly sensitive thin-film organic phototransistors: Effect of wavelength of light source on device performance.** *Journal of Applied Physics*, **98**(7):074505, 2005. 62
- [78] SHINUK CHO, JONATHAN YUEN, JIN YOUNG KIM, KWANGHEE LEE, AND ALAN J. HEEGER. **Photovoltaic effects on the organic ambipolar field-effect transistors.** *Applied Physics Letters*, **90**(6):063511, 2007. 62
- [79] N. MARJANOVIĆ, TH.B. SINGH, G. DENNLER, S. GÜNES, H. NEUGEBAUER, N.S. SARICIFTCI, R. SCHWÖDIAUER, AND S. BAUER. **Photoreponse of organic field-effect transistors based on conjugated polymer/fullerene blends.** *Organic Electronics*, **7**(4):188–194, August 2006. 62
- [80] W LUKOSZ AND R E KUNZ. **Light emission by magnetic and electric dipoles close to a plane interface I Total radiated power.** *Journal of the Optical Society of America*, **67**(12):1607, December 1977. 87
- [81] W LUKOSZ AND R E KUNZ. **Light emission by magnetic and electric dipoles close to a plane dielectric interface II Radiation patterns of perpendicular oriented dipoles.** *Journal of the Optical Society of America*, **67**(12):1615, December 1977. 87
- [82] W. LUKOSZ AND R.E. KUNZ. **Fluorescence lifetime of magnetic and electric dipoles near a dielectric interface.** *Optics Communications*, **20**(2):195–199, February 1977. 87
- [83] W LUKOSZ, D CLERC, P M NELLEN, C STAMM, AND P WEISS. **Output grating couplers on planar optical waveguides as direct immunosensors.** *Biosensors & bioelectronics*, **6**(3):227–32, January 1991. 87

Appendix A

Appendix

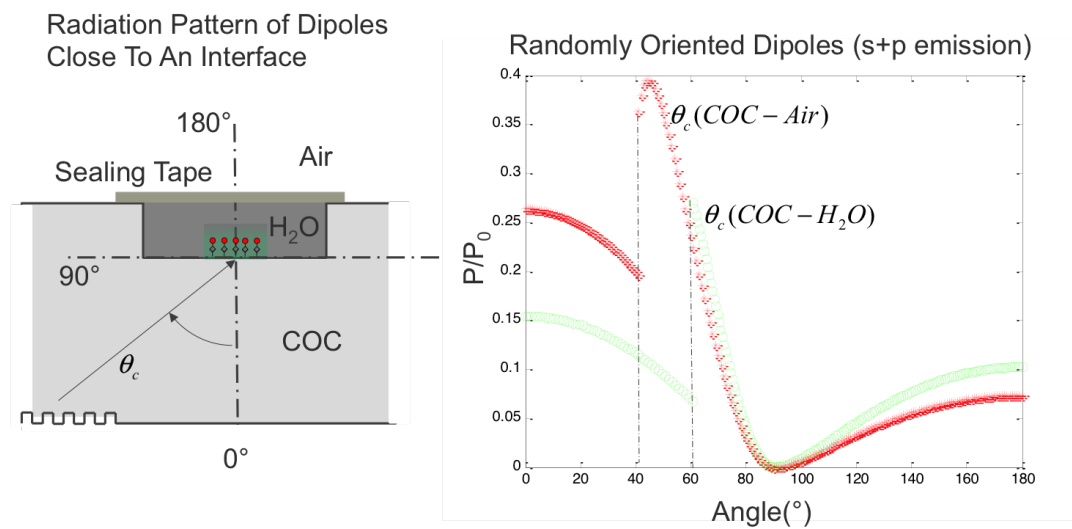


Course followed : EE5390 Computation Electromagnetics , Uni. Texas El Paso Course, Prof. R. C. Rumpf

Figure A.1: Simulation of optical field at the interface - Device is shown on the left, calculated steady state electric field is shown (middle) for $\theta_{in} < \theta_C$ (right) for $\theta_{in} > \theta_C$

FDFD method was implemented in Matlab and also in Python after following online course by Prof. R.C. Rumpf at University of Texas El Paso. Simulation of monochromatic light beam incident upon interface between COC ($n = 1.53$) and water ($n = 1.33$) is performed. Figure A.1 shows the device and the plot of calculated steady state electric field when incident angle is smaller/larger than the critical angle of the interface.

Fluorescence emission from a dipole very close the interface between two optical media is modified[31, 80, 81, 82][32][83][34]. When the dipole is in rarer medium major part of the emission occurs in so called forbidden region. This causes fluorescence to get trapped or in-coupled into the denser medium. The model proposed of Lukosz et al. is implemented in Python programming language. The figure A.2 shows the condition at the interface and corresponding radiation pattern calculated from the model. The Y-axis on radiation pattern is normalized with power emitted in absence of interface. Higher the contrast between the refractive index of the interface media, higher the emission into the forbidden region.



Lukosz, W. (1979), Journal of the Optical Society of America, 69(11), 1495

Figure A.2: Radiation pattern of dipole close to optical interface - (left) Schematic of the interface (right) Plots are for s+p polarization added together. Red plot is for COC-Air interface and Green plot is for COC-Water interface.

Acknowledgements

I want to sincerely thank CSEM SA (Swiss Center for Electronics and Microtechnology) for giving me the opportunity to work for my PhD and supporting me in all aspects. My colleagues at Muttentz/Basel center were very resourceful.

CSEM has been an incredible environment for my career. It is one of the very few companies well placed at the juncture of academics and industry. More information about CSEM SA can be found on the website www.csem.ch.

Sincere thanks to Prof. Dr. Christian Schönenberger and Dr. Alexander Stuck for supporting at critical junctions during my thesis.

I want to extend sincere gratitude towards Dr. David Leuenberger, Mr. Guillaume Basset and Dr. Adrian von Mühlénen for guiding me and for excellent discussions.

I thank management team at CSEM Muttentz Dr. Giovanni Nisato, Dr. Marc Schnieper and Dr. Christian Bosshard for their excellent support.

Many thanks to Ms. Angélique Luu-Dinh, Mr. Nicolas Glaser, Dr. Frédéric Zanella at CSEM Muttentz, Sarah Heub from CSEM Landquart, Janko Auswalder from CSEM Alpnach.

My wife's support was incredible during my work, especially in last 4 months! I could not thank her enough!

My parents always believed in me and encouraged me. My grandparents' zealous attitude and extreme curiosity always inspired me.

Thanks to my dearest friend Dr. Pradyumna Ayyalasomayajula for everything. We started our masters together and at the end finished our PhDs together. It has been a wonderful journey!

My sincere thanks to Mrs. Ranjana Sahasrabudhe for helping to give me perspective on my writing as a researcher from pharmacology domain.

Finally, discovering ketogenic diet provided me the physical and mental boost required during final six months of my work. Therefore thanks to all the researchers, bloggers who thought differently.

Curriculum Vitae - NEERAJ ADSUL

Email: neeraj.adsul@gmail.com Web: <http://www.neerajadsul.com>

EDUCATION

- 09/2010 - 12/2013 University of Basel, Switzerland.
Ph.D. in Nanoscience
- 10/2006 - 01/2008 University of Neuchâtel, Switzerland.
Master of Science (M.Sc.) in Micro-Nanotechnologies
- 09/2001 - 09/2005 PICT College, University of Pune, India.
B.Eng. in Electronics and Telecommunication

WORK EXPERIENCE

- 04/2005 - 08/2006 Co-founded Tantradnya Designs, Pune.
An Embedded Systems Company.
- 07/2008 - 09/2010 Ph.D. Student at CSEM SA.
High performance, solution processed OFETs
- 07/2007 - 09/2007 IEEE 802.15.4 wireless firmware intern.
ESPLAB, IMT Neuchatel

ADDITIONAL INFORMATION

- Microsoft Robotics Expo 2009, Bern Switzerland – 2nd Prize for Automatic Book Scanner
- First prize at Impetus & Concepts 2005, a National Level Engineering Project Competition
- First Prize in Mathematics 2001, at pre-university level.
- Theater: Lead /supporting actor role in 5 one-act plays,
- College Drama team organization won “Best Organized Team Award” for 2 consecutive years.
- Tabla player – a traditional Indian percussion instrument

PATENTS/PUBLICATIONS

- European patent pending titled “Integrated Optical Diagnostics Platform”, D. Leuenberger, N. Adsul, G. Nisato., Number 13177871.4 – 1554 filed on 24.07.2013.
- European patent pending titled “Point-of-Care Testing Device and Reader”, D. Leuenberger, N. Adsul, G. Nisato., Number 13155794.4 – 1554 filed on 12.04.2013
- “Integrated optical biosensor based on organic optoelectronic components”, Poster session presented at NanoBio conference 2010, August 24-27, Zurich, Switzerland